ACCELERATING INDUCTION MACHINE FINITE-ELEMENT SIMULATION WITH PARALLEL PROCESSING

BY

CHRISTINE ANNE HAINES ROSS

THESIS

Submitted in partial fulfillment of the requirements
for the degree of Master of Science in Electrical and Computer Engineering
in the Graduate College of the
University of Illinois at Urbana-Champaign, 2015

Urbana, Illinois

Adviser:

Professor Philip T. Krein

ABSTRACT

Finite element analysis used for detailed electromagnetic analysis and design of electric machines is computationally intensive. A means of accelerating two-dimensional transient finite element analysis, required for induction machine modeling, is explored using graphical processing units (GPUs) for parallel processing. The graphical processing units, widely used for image processing, can provide faster computation times than CPUs alone due to the thousands of small processors that comprise the GPUs. Computations that are suitable for parallel processing using GPUs are calculations that can be decomposed into subsections that are independent and can be computed in parallel and reassembled. The steps and components of the transient finite element simulation are analyzed to determine if using GPUs for calculations can speed up the simulation. The dominant steps of the finite element simulation are preconditioner formation, computation of the sparse iterative solution, and matrix-vector multiplication for magnetic flux density calculation. Due to the sparsity of the finite element problem, GPU-implementation of the sparse iterative solution did not result in faster computation times. The dominant speed-up achieved using the GPUs resulted from matrix-vector multiplication. Simulation results for a benchmark nonlinear magnetic material transient eddy current problem and linear magnetic material transient linear induction machine problem are presented. The finite element analysis program is implemented with MATLAB R2014a to compare sparse matrix format computations to readily available GPU matrix and vector formats and Compute Unified Device Architecture (CUDA) functions linked to MATLAB. Overall speed-up achieved for the simulations resulted in 1.2-3.5 times faster computation of the finite element solution using a hybrid CPU/GPU implementation over the

CPU-only implementation. The variation in speed-up is dependent on the sparsity and number of unknowns of the problem.

To My Supportive Family and Friends

ACKNOWLEDGMENTS

This project would not have been possible without the support of many people. Many thanks to my advisor, Philip T. Krein, for his patience and technical guidance. Thanks to the University of Illinois Graduate College for awarding me a SURGE Fellowship, and the Grainger Center for Electric Machinery and Electromechanics for granting me research assistantships, providing me with the financial means to complete this project.   And finally, thanks to my husband, parents, and numerous friends who endured this long process with me, always offering support and love.

TABLE OF CONTENTS

CHAPTER 1
INTRODUCTION

Electric machines constitute approximately two-thirds of all industrial electric power consumption [1]. An improvement in efficiency to a large number of electric machines thus conserves large amounts of electrical energy. This motivates improvements to electric machine design to reduce inefficiencies.

Specifically, induction machines and permanent-magnet synchronous machines are two types of machines that interest engineers and researchers. Induction machines are considered the "work horse" of electric machines [2]. Specific uses of induction machines include air conditioning units, pumps, hoists, servos, and bench tools. Most induction machines used today use the same design for induction machines developed in the 1960s. Those induction machines were intended to use electric line power from the power grid, i.e., at a fixed frequency. The technology available today in power electronics enables variable-frequency control of induction machines. Such a different control necessitates a change in design of induction machines in order to efficiently operate them with this different control.

Present commonly used tools for electric machine design include analytical circuit equivalents and finite-element models (FEM) [2], [3]. Analytical circuit equivalents of electric machines are a fast way to design a machine but do not model the machines as accurately as finite-element models because they cannot model the nonlinear magnetic behavior used in the construction of electric machines. This is important because induction machines may be operated near or at the magnetic saturation of the magnetically permeable material. However, finite-element models can model the nonlinear magnetic material used in electric machines, but they can be time-consuming to set up and simulate the machine. As a result, many electric machine designers use analytical models to create an initial design, and then use finite-element models to verify the design.

Decreasing the simulation time of a finite-element model of an electric machine makes the finite-element model a more desirable design tool for electric machine design.   Several approaches have been used to decrease the simulation time. Numerical approaches include the shooting-Newton method used to compute fewer iterations to obtain a steady-state solution [4]. Domain decomposition is another technique used to divide a finite-element domain into smaller domains for more efficient computation [5]. The approach examined in this thesis is to use parallel programming to reduce the simulation time.

CHAPTER 2
MAGNETIC VECTOR POTENTIAL FORMULATION AND FINITE ELEMENT IMPLEMENTATION

2.1 Magnetic Vector Potential Formulation

The electromagnetic fields for an electric machine involve magnetic flux density $(\mathbf{B})$ through materials with different conductivity (σ), permeability (μ), permittivity (ε), stationary and moving parts, and excitation by applying voltage or current. The magnetic flux density is solved for in a domain Ω with boundary Γ. The fields are described by Maxwell's equations and constitutive relations [6]:

$$\nabla\times\mathbf{E}=-\frac{\partial\mathbf{B}}{\partial t} \tag{2.1}$$

$$\nabla\times\mathbf{H}=\frac{\partial\mathbf{D}}{\partial t}+\mathbf{J} \tag{2.2}$$

$$\nabla\cdot\mathbf{D}=0 \tag{2.3}$$

$$\nabla\cdot\mathbf{B}=0 \tag{2.4}$$

$$\nabla\cdot(\sigma\mathbf{E})=0 \tag{2.5}$$

$$\mathbf{D}=\varepsilon\mathbf{E} \tag{2.6}$$

$$\mathbf{B}=\mu\mathbf{H} \tag{2.7}$$

where $\mathbf{E}$ is the electric field intensity, $\mathbf{D}$ is the electric flux density, $\mathbf{H}$ is the magnetic field intensity, ε is the permittivity, and $\mathbf{J}$ is current density. Current density can be decomposed into three parts: the impressed current $\mathbf{J}_s$, eddy current $\sigma\mathbf{E}$, and current induced by motion $\sigma \mathrm{v}\times\mathbf{B}$ where v is the velocity of the conductor with respect to $\mathbf{B}$ [3]. $\mathbf{J}$ is expressed as

$$\mathbf{J} = \mathbf{J}_s + \sigma\mathbf{E} + \sigma \mathrm{v}\times\mathbf{B} \tag{2.8}$$

The magnetic vector potential **A** is used to simulate the electromagnetic fields. It is related to the magnetic flux density by the equation

$$\mathbf{B} = \nabla\times\mathbf{A} \tag{2.9}$$

These equations can be combined to form one equation that describes the electromagnetic behavior of an electric machine. Substituting equation (2.1) into equation (2.9) and rearranging yields

$$\nabla\times\left(\mathbf{E} + \frac{\partial\mathbf{A}}{\partial \mathrm{t}}\right) = 0 \tag{2.10}$$

The electric scalar potential *V* is defined as

$$\mathbf{E} = -\nabla V - \frac{\partial\mathbf{A}}{\partial \mathrm{t}} \tag{2.11}$$

Using the constitutive relations described by equations (2.6) and (2.7), substituting equations (2.8), (2.9), and (2.11) into equation (2.2), and rearranging yields

$$\nabla\times\left(\frac{1}{\mu}\nabla\times\mathbf{A}\right) + \sigma\frac{\partial\mathbf{A}}{\partial \mathrm{t}} + \varepsilon\frac{\partial^2\mathbf{A}}{\partial \mathrm{t}^2} = -\nabla\left(\varepsilon\frac{\partial V}{\partial \mathrm{t}} + \sigma V\right) + \mathbf{J}_s + \sigma \mathrm{v}\times\left(\nabla\times\mathbf{A}\right) \tag{2.12}$$

The derivation considered here applies to isotropic media using scalars instead of dyads to represent material properties [6]. Within each finite element subdomain, each type of material is represented by scalar quantities of permittivity, permeability, and conductivity according to:

$$\begin{aligned}\overline{\varepsilon}(x,y,z,t) &= \varepsilon\\ \overline{\mu}(x,y,z,t) &= \mu\\ \overline{\sigma}(x.y,z,t) &= \sigma\end{aligned}$$

Using the vector identity $\nabla\times\left(\frac{1}{\mu}\nabla\times\mathbf{A}\right)=\frac{1}{\mu}\nabla\left(\nabla\cdot\mathbf{A}\right)-\frac{1}{\mu}\nabla^2\mathbf{A}+\nabla\frac{1}{\mu}\times\nabla\times\mathbf{A}$, equation (2.12) simplifies to

$$\begin{gathered}\frac{1}{\mu}\nabla^2\mathbf{A}-\nabla\frac{1}{\mu}\times\nabla\times\mathbf{A}-\sigma\frac{\partial\mathbf{A}}{\partial \mathrm{t}}-\varepsilon\frac{\partial^2\mathbf{A}}{\partial \mathrm{t}^2}= \\ \nabla\left(\varepsilon\frac{\partial V}{\partial \mathrm{t}}+\sigma V+\frac{1}{\mu}\nabla\cdot\mathbf{A}\right)-\mathbf{J}_s-\sigma\mathrm{v}\times\left(\nabla\times\mathbf{A}\right)\end{gathered}\tag{2.13}$$

Equation (2.13) includes the behavior of inhomogeneous material with the $\nabla\frac{1}{\mu}$ term. This formulation only includes homogeneous and uniform magnetic material properties, so the $\nabla\frac{1}{\mu}$ vanishes [7] resulting in the standard wave equation

$$\frac{1}{\mu}\nabla^2\mathbf{A}-\sigma\frac{\partial\mathbf{A}}{\partial \mathrm{t}}-\varepsilon\frac{\partial^2\mathbf{A}}{\partial \mathrm{t}^2}=\frac{1}{\mu}\nabla\left(\mu\varepsilon\frac{\partial V}{\partial \mathrm{t}}+\mu\sigma V+\nabla\cdot\mathbf{A}\right)-\mathbf{J}_s-\sigma\mathrm{v}\times\left(\nabla\times\mathbf{A}\right)\tag{2.14}$$

Next, the divergence of **A** should be specified since it is not fully determined by equation (2.9). For a unique solution to the wave equation, a *gauge condition*, i.e., the choice of $\nabla\cdot\mathbf{A}$, should be specified, although that may not be necessary since **B** is the value of interest in machine behavior [6]. In cases where the value of eddy current is desired, the gauge condition must be specified since the value of **A** is directly used to calculate eddy current. Not specifying the gauge condition can lead to numerical instability in iterative solutions and may reduce computational precision [7]. The selected gauge condition is the *diffusion gauge* defined by

$$\nabla\cdot\mathbf{A}=-\varepsilon\frac{\partial V}{\partial t}\tag{2.15}$$

Applying the gauge condition to equation (2.14) yields

$$\frac{1}{\mu}\nabla^2\mathbf{A}-\sigma\frac{\partial\mathbf{A}}{\partial \mathrm{t}}-\varepsilon\frac{\partial^2\mathbf{A}}{\partial \mathrm{t}^2}=\nabla\left(\sigma V\right)-\mathbf{J}_s-\sigma\mathrm{v}\times\left(\nabla\times\mathbf{A}\right)\tag{2.16}$$

This equation is simplified by neglecting the gradient of the electric scalar potential term, which is a function of the current density resulting from low-frequency voltage source excitation and resistance, and the magnetic vector potential second-derivative term, which is the displacement current and is small for low-frequency applications [7]. These assumptions reduce equation (2.16) to

$$\frac{1}{\mu}\nabla^2\mathbf{A}-\sigma\frac{\partial\mathbf{A}}{\partial \mathrm{t}}=-\mathbf{J}_s-\sigma \mathrm{v}\times\left(\nabla\times\mathbf{A}\right) \tag{2.17}$$

This equation is the main equation that describes the electromagnetic behavior of electric machines using magnetic vector potential. In a two-dimensional simulation, with impressed current density applied in the z-direction, the magnetic vector potential only has a single component, A_z. Reducing the problem to two dimensions means that the simulation assumes the electric machine has infinite axial length. When conducting simulation studies of electric machine designs, this assumption is appropriate for preliminary and semi-detailed machine analysis. This two-dimensional simplification of the electric machine analysis enables significantly faster analysis. However, for detailed machine design and analysis, a three-dimensional simulation that captures end turn effects should be conducted.

The velocity term of equation (2.17) can be eliminated by setting velocity to zero and neglecting motion or by employing a frame of reference that is fixed with respect to the moving component so that the relative velocity v becomes zero. This reference frame is created by fixing the mesh to the surface of the moving component and moving or remeshing only the elements in the air around the component [3]. To simplify the meshing and finite element implementation, motion is neglected in this formulation.

Using the fact that magnetic vector potential only has a single component in the z-direction for the two-dimensional analysis and neglecting motion, equation (2.17) reduces to

$$\frac{1}{\mu}\left(\frac{\partial^2 A}{\partial x^2}+\frac{\partial^2 A}{\partial y^2}\right)-\sigma\frac{\partial A}{\partial \mathrm{t}}=-J \qquad (2.18)$$

where *A* is understood to be z-directed and only varies in the x- and y-directions, and *J* is the impressed z-directed current density. Equation (2.18) is referred to as a magnetic diffusion equation.

2.2 Finite Element Discretization

The Galerkin approach is used to derive the finite element equations. It is a special case of the method of weighted residuals. The Galerkin method uses the weighting function of the same form as the finite element shape function [6], [3], [7]. The magnetic vector potential within an element is approximated by the sum of shape functions. With $\hat{A}$ denoting the approximation of *A*, the magnetic vector potential within an element *e* is approximated by

$$\hat{A}^e=\sum_{i=1}^{m} N_i^e(x,y)\hat{A}_i^e \qquad (2.19)$$

for *m* nodes in the element and N_i^e element shape functions.

The residual *r* of equation (2.18) with the approximation of *A* denoted as $\hat{A}$ is

$$r=\frac{1}{\mu}\left(\frac{\partial^2 \hat{A}}{\partial x^2}+\frac{\partial^2 \hat{A}}{\partial y^2}\right)-\sigma\frac{\partial \hat{A}}{\partial \mathrm{t}}+J \qquad (2.20)$$

The weighted residual for element *e* is

$$R_i^e=\iint_{\Omega^e} N_i^e\left[\frac{1}{\mu^e}\left(\frac{\partial^2 \hat{A}}{\partial x^2}+\frac{\partial^2 \hat{A}}{\partial y^2}\right)-\sigma^e\frac{\partial \hat{A}}{\partial \mathrm{t}}+J\right]dxdy \qquad i=1,2,\ldots,m \qquad (2.21)$$

where Ω^e denotes the element domain. Integrating by parts, equation (2.21) can be written as

$$
\begin{aligned}
R_i^e = \iint_{\Omega^e} \frac{1}{\mu^e}\left(\frac{\partial N_i^e}{\partial x}\frac{\partial \hat{A}}{\partial x} + \frac{\partial N_i^e}{\partial y}\frac{\partial \hat{A}}{\partial y}\right) dxdy - \oint_{\Gamma^e} \frac{1}{\mu^e}\, N_i^e \left(\frac{\partial \hat{A}}{\partial x}\hat{x} + \frac{\partial \hat{A}}{\partial y}\hat{y}\right)\cdot \hat{n}^e \; d\Gamma^e \\
- \iint_{\Omega^e} N_i^e \sigma^e \frac{\partial \hat{A}}{\partial \mathrm{t}} \; dxdy + \iint_{\Omega^e} N_i^e J \; dxdy
\end{aligned}
\tag{2.22}
$$

where Γ^e denotes the contour enclosing Ω^e and $\hat{n}^e$ is the outward unit vector normal to Γ^e.

To solve for the finite-element domain solution, the element weighted residuals, represented by equation (2.22), are assembled by summation with the same equation with shape functions for the other elements. The system residual should be zero so that the approximated $\hat{A}$ equates to the actual *A*. For *M* elements, this system residual is described by

$$
\begin{aligned}
\sum_{e=1}^{M}\left\{\iint_{\Omega^e} \frac{1}{\mu^e}\left(\frac{\partial N_i^e}{\partial x}\frac{\partial \hat{A}}{\partial x} + \frac{\partial N_i^e}{\partial y}\frac{\partial \hat{A}}{\partial y}\right) dxdy - \oint_{\Gamma^e} \frac{1}{\mu^e}\, N_i^e \left(\frac{\partial \hat{A}}{\partial x}\hat{x} + \frac{\partial \hat{A}}{\partial y}\hat{y}\right)\cdot \hat{n}^e \; d\Gamma^e\right\} + \\
\sum_{e=1}^{M}\left\{- \iint_{\Omega^e} N_i^e \sigma^e \frac{\partial \hat{A}}{\partial \mathrm{t}} \; dxdy + \iint_{\Omega^e} N_i^e J \; dxdy\right\} = 0
\end{aligned}
\tag{2.23}
$$

From the derivation in [6], the internal element sides do not contribute to the line integral. By imposing the homogeneous *Neumann* boundary condition, which is defined by $\frac{\partial \hat{A}}{\partial \hat{n}^e} = 0$, the line integral is zero. When the finite element method is used with other solution techniques, such as the boundary element method or an analytical expression to represent techniques the air-gap region solution [3], this may not be a suitable boundary condition. In that case, the line integral must be evaluated [3]. This formulation only uses the finite element method, so the homogeneous Neumann boundary condition is satisfactory and simplifies the solution calculation.

The reluctivity term is introduced, which is simply $\nu = \frac{1}{\mu}$. With the line integral term equal to zero, the following equation shows equation (2.23) written in matrix form:

$$\sum_{e=1}^{M} [S]^e \left\{\hat{A}\right\} + \sum_{e=1}^{M} [T]^e \left\{\frac{\partial \hat{A}}{\partial \mathrm{t}}\right\} - \sum_{e=1}^{M} \{Q\}^e = \{0\} \tag{2.24}$$

or even more compactly as

$$[S]\left\{\hat{A}\right\} + [T]\left\{\frac{\partial \hat{A}}{\partial \mathrm{t}}\right\} - \{Q\} = \{0\} \tag{2.25}$$

where it is understood that the *S*, *T*, and *Q* matrices are assembled by summing over the elements. Entries in these matrices are given by:

$$S_{ij}^e = \iint \nu^e \left(\frac{\partial N_i^e}{\partial x} \frac{\partial N_j^e}{\partial x} + \frac{\partial N_i^e}{\partial y} \frac{\partial N_j^e}{\partial y} \right) dxdy \tag{2.26}$$

$$T_{ij}^e = \iint \sigma^e N_i^e N_j^e \; dxdy \tag{2.27}$$

$$Q_i^e = \iint J^e N_i^e \; dxdy \tag{2.28}$$

for $i, j = 1, 2, ..., m$ nodes per element. $\left\{\hat{A}\right\}$ and $\left\{\frac{\partial \hat{A}}{\partial \mathrm{t}}\right\}$ correspond to the *j*th node. The integrals in these matrices can be evaluated analytically or numerically. The matrices depend on the element order and corresponding shape function.

2.2.1 First-order elements

First-order elements consist of three nodes connected by three edges to form a triangle. Figure 2.1 illustrates a first-order triangular element. For mesh consistency, they must be numbered counterclockwise. The unknown function $\hat{A}$ varies linearly within each element and is approximated as

$$\hat{A}^e(x,y) = a^e + b^e x + c^e y \tag{2.29}$$

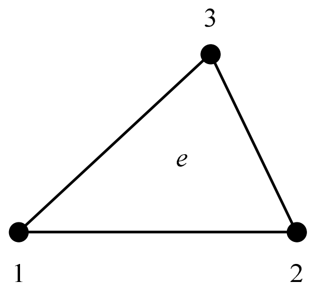

Figure 2.1 First-order triangular element

With m = 3, the shape functions which approximate $\hat{A}^e$ according to equation (2.29) satisfy equation (2.19). The derivation of the first-order shape functions can be found in [6] and [3]. For first-order elements, the shape functions are given by

$$N_j^e(x,y) = \frac{1}{2\Delta^e}(\alpha_j^e + \beta_j^e x + \gamma_j^e y) \qquad j = 1,2,3 \tag{2.30}$$

with

$$\begin{aligned} \alpha_1^e &= x_2^e y_3^e - y_2^e x_3^e; & \beta_1^e &= y_2^e - y_3^e; & \gamma_1^e &= \mathrm{x}_3^e - x_2^e \\ \alpha_2^e &= x_3^e y_1^e - y_3^e x_1^e; & \beta_2^e &= y_3^e - y_1^e; & \gamma_2^e &= \mathrm{x}_1^e - x_3^e \\ \alpha_3^e &= x_1^e y_2^e - y_1^e x_2^e; & \beta_3^e &= y_1^e - y_2^e; & \gamma_3^e &= \mathrm{x}_2^e - x_1^e \end{aligned} \tag{2.31}$$

and

$$\begin{aligned} \Delta^e &= \frac{1}{2}\left(\beta_1^e \gamma_2^e - \beta_2^e \gamma_1^e\right) \\ &= \text{ area of the element } e \end{aligned} \tag{2.32}$$

Using these shape functions, equations (2.26), (2.27), and (2.28) evaluate to

$$S_{ij}^e = \frac{\nu^e\left(\beta_i^e \beta_j^e + \gamma_i^e \gamma_j^e\right)}{4\Delta^e}, \quad \mathrm{T}_{ij}^e = \sigma^e \frac{\left(\delta_{ij}+1\right)\Delta^e}{12}, \quad \mathrm{Q}_i^e = J^e \frac{\Delta^e}{3} \tag{2.33}$$

where δ_{ij} = 1 when $i = j$, otherwise, δ_{ij} = 0. Note that for this implementation, reluctivity and conductivity are constant throughout the element.

2.2.2 Second-order elements

Second-order elements consist of six nodes connected by three edges to form a triangle. Figure 2.2 illustrates a second-order triangular element. For mesh consistency, they must be numbered in increasing order as shown in Figure 2.2. Higher-order elements are used to improve element accuracy. Another method of improving accuracy is to solve the system with a greater mesh density, i.e., smaller elements. Results and discussion about these options are presented for a benchmark problem in Section 4.3 Simulation Results. The unknown function $\hat{A}$ is a quadratic function within each element and is approximated as

$$\hat{A}^e(x, y) = a^e + b^e x + c^e y + d^e x^2 + e^e xy + f^e y^2 \tag{2.34}$$

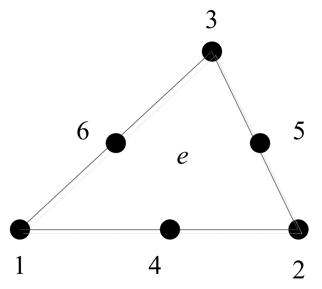

Figure 2.2 Second-order triangular element

With m = 6, the shape functions which approximate $\hat{A}^e$ according to equation (2.34) satisfy equation (2.19). The derivation of the second-order shape functions can be found in [6]. For second-order elements, the shape functions are given by

$$\begin{aligned} &N_j^e(x, y) = \left(2L_j^e - 1\right) L_j^e, \qquad j = 1, 2, 3 \\ &N_4^e(x, y) = 4L_1^e L_2^e, \quad N_5^e(x, y) = 4L_2^e L_3^e, \quad N_6^e(x, y) = 4L_3^e L_1^e \end{aligned} \tag{2.35}$$

with

$$L_j^e(x,y) = \frac{1}{2\Delta^e}(\alpha_j^e + \beta_j^e x + \gamma_j^e y) \qquad j = 1,2,3 \tag{2.36}$$

and the same α_j^e, β_j^e, γ_j^e, and Δ^e as defined for first-order elements.

Using these shape functions, equations (2.26), (2.27), and (2.28) evaluate to

$$\begin{aligned}
S_{ij}^e &= \nu^e \frac{4\delta_{ij}-1}{12\Delta^e}\left(\beta_i^e\beta_j^e + \gamma_i^e\gamma_j^e\right) \qquad i, j = 1,2,3 \\
S_{14}^e &= S_{24}^e = \frac{4}{3}S_{12}^e, \qquad S_{16}^e = S_{36}^e = \frac{4}{3}S_{13}^e \\
S_{25}^e &= S_{35}^e = \frac{4}{3}S_{23}^e, \qquad S_{15}^e = S_{26}^e = S_{34}^e = 0 \\
S_{44}^e &= \nu^e \frac{2}{3\Delta^e}\left[\left(\beta_1^e + \beta_2^e\right)^2 + \left(\gamma_1^e + \gamma_2^e\right)^2\right] \\
S_{55}^e &= \nu^e \frac{2}{3\Delta^e}\left[\left(\beta_2^e + \beta_3^e\right)^2 + \left(\gamma_2^e + \gamma_3^e\right)^2\right] \\
S_{66}^e &= \nu^e \frac{2}{3\Delta^e}\left[\left(\beta_3^e + \beta_1^e\right)^2 + \left(\gamma_3^e + \gamma_1^e\right)^2\right] \\
S_{45}^e &= \nu^e \frac{1}{3\Delta^e}\left[\left(\beta_2^e\beta_3^e + 2\beta_1^e\beta_3^e + \beta_1^e\beta_2^e + \beta_2^{e2}\right) + \left(\gamma_2^e\gamma_3^e + 2\gamma_1^e\gamma_3^e + \gamma_1^e\gamma_2^e + \gamma_2^{e2}\right)^2\right] \\
S_{46}^e &= \nu^e \frac{1}{3\Delta^e}\left[\left(\beta_1^e\beta_3^e + 2\beta_2^e\beta_3^e + \beta_1^e\beta_2^e + \beta_1^{e2}\right) + \left(\gamma_1^e\gamma_3^e + 2\gamma_2^e\gamma_3^e + \gamma_1^e\gamma_2^e + \gamma_1^{e2}\right)^2\right] \\
S_{56}^e &= \nu^e \frac{1}{3\Delta^e}\left[\left(\beta_3^e\beta_1^e + 2\beta_2^e\beta_1^e + \beta_2^e\beta_3^e + \beta_3^{e2}\right) + \left(\gamma_3^e\gamma_1^e + 2\gamma_2^e\gamma_1^e + \gamma_2^e\gamma_3^e + \gamma_3^{e2}\right)^2\right]
\end{aligned} \tag{2.37}$$

$$T_{ij}^e = \sigma^e \frac{\Delta^e}{180}\begin{bmatrix} 6 & -1 & -1 & 0 & -4 & 0 \\ -1 & 6 & -1 & 0 & 0 & -4 \\ -1 & -1 & 6 & -4 & 0 & 0 \\ 0 & 0 & -4 & 32 & 16 & 16 \\ -4 & 0 & 0 & 16 & 32 & 16 \\ 0 & -4 & 0 & 16 & 16 & 32 \end{bmatrix} \tag{2.38}$$

$$Q_i^e = \begin{cases} 0 & i = 1,2,3 \\ \dfrac{\Delta^e}{3} J^e & i = 4,5,6 \end{cases} \tag{2.39}$$

2.3 Time Discretization

The discretized system of equations for magnetodynamic finite-element analysis varies with time. To emphasize this, equation (2.25) can be written as

$$[S]\left\{\hat{A}(t)\right\} + [T]\left\{\frac{\partial \hat{A}(t)}{\partial \mathrm{t}}\right\} - \{Q(t)\} = \{0\} \tag{2.40}$$

In the case where motion is not modeled or a fixed reference frame is used, the *S*, *T*, and mesh-dependent sections of *Q* matrices are not time-dependent. Note that the *Q* matrix is shown to vary with time, but that is only because the applied current density *J* may vary with time. If motion were modeled with a reference frame, then elements in air are deformed with respect to time while all other elements remain the same. In air, the conductivity is zero, so this element deformation would not affect *T* and the mesh-dependent sections of *Q*. The *S* matrix would change with respect to time [3].

For induction machines, the magnetic field is time-varying within a conducting region which induces an electromotive force (emf) according to Faraday's law described by equation (2.1). This induced emf produces current, called eddy current, in conducting material normal to the magnetic flux. The eddy currents in the rotor create magnetic poles that interact with the stator poles created by the excitation current, causing the rotor to move. Modeling eddy current is essential to simulate an induction machine, so a magnetostatic formulation is not suitable. Either a time-harmonic or time-domain simulation can be used. Time-harmonic steady-state simulations, where the time-varying fields are sinusoidal and represented by a single frequency, are typically represented by the Fourier transform of equation (2.18) [3]:

$$\frac{1}{\mu}\left(\frac{\partial^2 A}{\partial x^2}+\frac{\partial^2 A}{\partial y^2}\right)-j\omega\sigma A=-J \tag{2.41}$$

The use of the time-domain simulation over the time-harmonic simulation is discussed in section 2.6 Nonlinear Formulation, where nonlinear magnetic material is addressed. For linear magnetic material simulations, time-harmonic analysis described by equation (2.41) can be used for steady-state simulations at a specified frequency. For linear or nonlinear magnetic material problems, simulations not at steady-state or involving non-sinusoidal excitation require the solution of the time-domain equation (2.40). For the simulations in this thesis, the time-domain formulation is used to model all possible frequencies of electromagnetic behavior.

The stator (ω_s) and rotor (ω_r) frequencies are related according to the rotor slip s according to

$$s=\frac{\omega_s-\omega_r}{\omega_s} \tag{2.42}$$

For a stationary time-domain formulation, the impressed current density is applied at slip frequency instead of the stator frequency in order to represent the mechanical power and torque produced on the rotor.

While the time-domain simulation enables eddy current simulation, the two-dimensional simulation limits the accurate simulation of total machine core losses. The eddy currents in the stator produce losses, called core losses, which the electric machine designer would like to minimize. Core losses are reduced by using laminated sheets which are electrically insulated from each other. The insulation is parallel to the direction of the magnetic flux density so that the eddy currents which flow normally to the magnetic flux density can only flow in each laminated sheet

[1]. A two-dimensional time-varying simulation thus only models the eddy current due to one lamination cross section.

The time-discretization of equation (2.40) follows the derivation in [3]. The time-discretization method used is based on:

$$\beta\left\{\frac{\partial A}{\partial t}\right\}^{t+\Delta t}+(1-\beta)\left\{\frac{\partial A}{\partial t}\right\}^{t}=\frac{\{A\}^{t+\Delta t}-\{A\}^{t}}{\Delta t} \tag{2.43}$$

The Δt symbol indicates the change in time. The constant β allows the difference method to be easily changed. Note that when $\beta = 0$, the algorithm is forward difference, when $\beta = 1$, the algorithm is backward difference, or when $0 < \beta < 1$, the algorithm is an intermediate type. When $\beta = \frac{1}{2}$, the algorithm is the Crank-Nicolson method [8].

Using equation (2.43) to discretize time in equation (2.40) yields

$$\left[[S]+\frac{1}{\beta\Delta t}[T]\right]\left\{\hat{A}\right\}^{t+\Delta t}=\left[\frac{1}{\beta\Delta t}[T]-\frac{1-\beta}{\beta}[S]\right]\left\{\hat{A}\right\}^{t}+\{Q\}^{t+\Delta t}+\frac{1-\beta}{\beta}\{Q\}^{t} \tag{2.44}$$

When reluctivity is linear, equation (2.44) is used to solve for $\left\{\hat{A}\right\}^{t+\Delta t}$ at each time step.

2.4 Sparse Iterative Linear Solvers

The system defined by equation (2.44) is essentially a sparse linear system equivalent to the typical

$$\mathbf{A}x = b$$

This sparse linear system also applies to the nonlinear formulation described in section 2.6 when solving for the change in magnetic vector potential used to update the next iteration. The matrix **A** is sparse, *b* is a vector, and the system is solved for the vector *x*. For the sparse matrices solved later in this thesis for time-domain formulations, the average density of nonzero elements in the matrix relative to the total number of elements is 0.0012. For example, given this density, for a 10,000 by 10,000 element matrix, approximately 117,430 elements of the matrix are nonzero out of the total 10^8 elements. An example of the matrix sparsity patterns is shown in Figure 2.3.

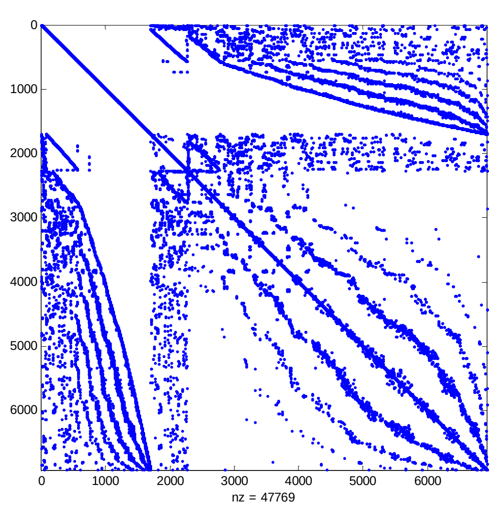

(a)

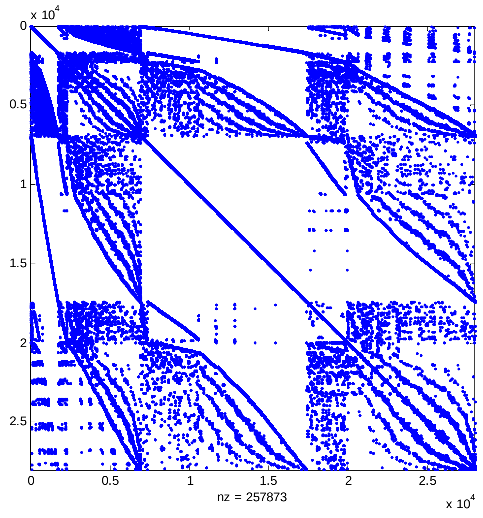

(b)

Figure 2.3 Matrix sparsity pattern for example time-domain meshes for (a) first-order elements and (b) second-order elements

The assignment of the element and node numbering upon mesh generation affect the sparsity structure of the matrix. For first-order elements, each element contributes nine nonzero entries (3x3 matrix according to node numbering). For first-order elements, each element contributes 36 nonzero entries (6x6 matrix according to node numbering).

There are several ways to solve the system. LU decomposition can be used. To solve the system using LU decomposition with forward and backward substitution for n unknowns, $O(n^3)$ multiplication operations are performed if $\mathbf{A}$ and b are full. The number of operations required when employing sparse LU decomposition techniques, such as those in [9]- [10], depends on the number and ordering of nonzero entries in the matrix.

Sparse iterative linear solvers are another option to solve the system. In particular, Krylov subspace methods can be used to solve the finite-element discretized system [11]. To solve the system using a sparse iterative linear solver for n unknowns, **A** is no longer treated as having $n \times n$ values, but rather only p nonzero values, and its inverse is found in terms of a linear combination of its powers. For well-conditioned matrices, this should reduce the number of operations that are performed to solve the system. Krylov subspace methods that use the Arnoldi [12] or Lanczos [13] process, such as generalized minimum residual method (GMRES) method [14], [15], conjugate gradient (CG) method [14], [16], bi-conjugate gradients (BiCG) method, and the bi-conjugate gradients stabilized (BiCGStab) method [14], [17], are $O(n^2)$ per iteration [18].

Finite element matrices can be ill-conditioned for the sparse iterative linear solvers. This means that the iterative solvers require many iterations to solve the system to a specified tolerance. Using a preconditioner can accelerate the convergence of the iterative solvers. While it takes a certain number of operations to create the preconditioner, the decrease in number of iterations required to solve the system using the preconditioner with the iterative solver may still require fewer operations than using iterative solver without the preconditioner. A preconditioner is used by solving the system

$$\mathbf{P}^{-1}\mathbf{A}x = \mathbf{P}^{-1}b \qquad (2.45)$$

Preconditioners used with iterative solvers are a computationally efficient way to find a matrix **P** such that $\mathbf{P}^{-1}\mathbf{A}$ is better conditioned than **A**. Two readily available preconditioners are the incomplete LU (ILU) preconditioner [11] and incomplete Cholesky factorization preconditioner [11], [19].

2.5 Post-Processing

After computing the solution for the nodal magnetic vector potential, other values may be computed from the solution in order to evaluate the physical behavior of the simulated problem. These other values are considered to be “post-processed” values since they are computed after the solution for *A* is found. The three post-processing values of interest in this thesis are the magnetic flux density **B**, eddy current, and force.

2.5.1 Magnetic flux density

The magnetic flux density is the first post-processed value of interest. Magnetic flux density has physical meaning and can be measured, unlike magnetic vector potential. For the linear ferromagnetic material model, magnetic flux density may be calculated outside of the magnetic vector potential finite-element solution. To minimize memory storage, it is beneficial to calculate the magnetic flux density at desired nodes or elements at each time step and store only those values rather than both of the entire magnetic vector potential and magnetic flux density solutions at each time step. For the nonlinear ferromagnetic material model, it is necessary to calculate the magnetic flux density magnitude at each node or element at every iteration in order to determine nonlinear reluctivity since reluctivity is a function of the square of magnetic vector potential.

Recalling from equation (2.9) that **B** is the curl of **A**, so **B** varies in each element with one degree of freedom less than **A**. For first-order elements, **B** is constant throughout the element. For second-order elements, **B** varies linearly throughout the element. Theoretically, the lower order elements decrease the accuracy of **B**. The element order accuracy and mesh density is examined in the benchmark problem simulation results in Chapter 4.

Since **B** is the curl of **A**, and **A** only has a single component A_z,

$$\mathbf{B} = \frac{\partial A_z}{\partial y}\hat{x} - \frac{\partial A_z}{\partial x}\hat{y} \tag{2.46}$$

The partial derivatives of A_z are computed from the shape functions that describe $\hat{A}_z$. **B** in terms of shape functions is

$$\mathbf{B}^e = \hat{x}\sum_{i=1}^{m}\frac{\partial N_i^e(x,y)}{\partial y}\hat{A}_i - \hat{y}\sum_{i=1}^{m}\frac{\partial N_i^e(x,y)}{\partial x}\hat{A}_i \tag{2.47}$$

For first-order elements, this equates to

$$\mathbf{B}^e = \hat{x}\frac{1}{2\Delta^e}\sum_{i=1}^{3}\gamma_i^e\hat{A}_i - \hat{y}\frac{1}{2\Delta^e}\sum_{i=1}^{3}\beta_i^e\hat{A}_i \tag{2.48}$$

Notice that the magnetic flux density is constant throughout the element. For second-order elements, the expressions becomes more complicated and equates to

$$\begin{aligned} B_x^e = \sum_{i=1}^{3}&\left(\frac{1}{\left(\Delta^e\right)^2}\left(\gamma_i^e\left(\alpha_i^e+\beta_i^e x+\gamma_i^e y\right)\right)-\frac{\gamma_i^e}{2\Delta^e}\right)\hat{A}_i + \\ &\left(\frac{1}{\left(\Delta^e\right)^2}\left(\gamma_2^e\left(\alpha_1^e+\beta_1^e x+\gamma_1^e y\right)+\gamma_1^e\left(\alpha_2^e+\beta_2^e x+\gamma_2^e y\right)\right)\right)\hat{A}_4 + \\ &\left(\frac{1}{\left(\Delta^e\right)^2}\left(\gamma_3^e\left(\alpha_2^e+\beta_2^e x+\gamma_2^e y\right)+\gamma_2^e\left(\alpha_3^e+\beta_3^e x+\gamma_3^e y\right)\right)\right)\hat{A}_5 + \\ &\left(\frac{1}{\left(\Delta^e\right)^2}\left(\gamma_3^e\left(\alpha_1^e+\beta_1^e x+\gamma_1^e y\right)+\gamma_1^e\left(\alpha_3^e+\beta_3^e x+\gamma_3^e y\right)\right)\right)\hat{A}_6 \end{aligned} \tag{2.49}$$

$$B_y^e = -\sum_{i=1}^{3}\left(\frac{1}{\left(\Delta^e\right)^2}\left(\beta_i^e\left(\alpha_i^e+\beta_i^e x+\gamma_i^e y\right)\right)-\frac{\gamma_i^e}{2\Delta^e}\right)\hat{A}_i -$$
$$\left(\frac{1}{\left(\Delta^e\right)^2}\left(\beta_2^e\left(\alpha_1^e+\beta_1^e x+\gamma_1^e y\right)+\beta_1^e\left(\alpha_2^e+\beta_2^e x+\gamma_2^e y\right)\right)\right)\hat{A}_4 -$$
$$\left(\frac{1}{\left(\Delta^e\right)^2}\left(\beta_3^e\left(\alpha_2^e+\beta_2^e x+\gamma_2^e y\right)+\beta_2^e\left(\alpha_3^e+\beta_3^e x+\gamma_3^e y\right)\right)\right)\hat{A}_5 - \quad (2.50)$$
$$\left(\frac{1}{\left(\Delta^e\right)^2}\left(\beta_3^e\left(\alpha_1^e+\beta_1^e x+\gamma_1^e y\right)+\beta_1^e\left(\alpha_3^e+\beta_3^e x+\gamma_3^e y\right)\right)\right)\hat{A}_6$$

$$\mathbf{B}^e = B_x^e\hat{x}+B_y^e\hat{y} \quad (2.51)$$

2.5.2 Eddy current density

The eddy current density is modeled by magnetic vector potential derived from Maxwell's equations. Using equation (2.11) that relates electric field to magnetic vector potential, neglecting the electric scalar potential, and knowing that

$$\mathbf{J}_{eddy} = \sigma\mathbf{E} \quad (2.52)$$

then eddy current in terms of magnetic vector potential is

$$\mathbf{J}_{eddy} = -\sigma\frac{\partial\mathbf{A}}{\partial \mathrm{t}} \quad (2.53)$$

In terms of time discretization using equation (2.43), eddy current density is calculated from the magnetic vector potential solution at each time step by

$$J_{eddy}^{t+\Delta t} = \frac{(\beta-1)}{\beta}J_{eddy}^{t} - \sigma\frac{\left(A^{t+\Delta t}-A^t\right)}{\beta\Delta t} \quad (2.54)$$

2.5.3 Force from Maxwell Stress Tensor

The purpose of an electric machine is to produce force or torque to do work. Measuring or computing these quantities is useful to evaluate the performance of the machine. There are several methods to compute the force from a finite element simulation. The Ampere's Force Law, Maxwell Stress Method, and Virtual Work Method are considered in [3]. In this thesis, the Maxwell Stress Method is used to compute force. It is used to find the total, not the local, force on an object. Additionally, the Maxwell Stress Tensor formulation in the air gap should result in accurate force calculation for linear and nonlinear magnetic material representation.

Following the derivation from [3], the volume force density can be written as the divergence of the Maxwell Stress Tensor (MST) **T**

$$p_v = \nabla \cdot \mathbf{T} \tag{2.55}$$

where **T** is derived as

$$\mathbf{T} = \frac{1}{\mu_0}\begin{pmatrix} B_x^2 - \frac{1}{2}|\mathbf{B}|^2 & B_x B_y & B_x B_z \\ B_y B_x & B_y^2 - \frac{1}{2}|\mathbf{B}|^2 & B_y B_z \\ B_z B_x & B_z B_y & B_z^2 - \frac{1}{2}|\mathbf{B}|^2 \end{pmatrix} \tag{2.56}$$

Integrating and using the vector divergence theorem, the total force can be expressed as

$$F = \oiint_S \mathbf{T} \cdot dS \tag{2.57}$$

Taking this surface integration to be a cylindrical surface through the machine airgap, this integration is reduced to a line for two-dimensional simulation to give force per unit depth. The tangential (F_t) and normal (F_n) force components in newtons per meter can be calculated according to

$$F_t = \oint_L dF_t = \oint_L \frac{B_n B_t}{\mu_0} dl$$
$$F_n = \oint_L dF_n = \oint_L \frac{B_n^2 - B_t^2}{2\mu_0} dl$$
$$B_n B_t = B_x B_y (s_x^2 - s_y^2) + s_x s_y (B_y^2 - B_x^2) \tag{2.58}$$
$$\begin{aligned} B_n^2 - B_t^2 &= B_x^2 s_y^2 - 2B_x B_y s_x s_y + B_y^2 s_x^2 - \left(B_x^2 s_x^2 + 2B_x B_y s_x s_y + B_y^2 s_y^2\right) \\ &= B_x^2 s_y^2 - 2B_x B_y s_x s_y + B_y^2 s_x^2 - \frac{1}{2}|B|^2 \end{aligned}$$

where the unit normal and tangential vectors to the integration path and tangential and normal components of flux density are defined as

$$\begin{aligned} \hat{a}_n &= s_x \hat{a}_x + s_y \hat{a}_y \\ \hat{a}_t &= -s_y \hat{a}_x + s_x \hat{a}_y \\ B_t &= B_x s_x + B_y s_y \\ B_n &= -B_x s_y + B_y s_x \end{aligned} \tag{2.59}$$

2.6 Nonlinear Formulation

Including the nonlinear permeability of the ferromagnetic material involved in an electric machine problem is necessary to obtain accurate simulations of magnetic flux saturation. Most induction machines operate near or in the saturation region, so only modeling linear permeability may yield inaccurate simulation results. To push the electric machines to their torque and power density limitations, the machines are likely to operate near saturation.

The permeability or equivalent reluctivity in the constitutive relation shown by equation (2.7) is nonlinear. It is a function of the local magnetic field. The most accurate physical representation of the **B-H** relationship includes nonlinearity and hysteresis. The family of hysteresis curves can be represented by a normal magnetization curve.

Figure 2.4 shows an example family of hysteresis curves. The dotted line represents a normal magnetization curve. For a specific steel, Figure 2.5 shows the initial magnetization nonlinear B-H curve. This steel curve is used for the nonlinear simulation of the benchmark problem described in Chapter 4. From this data, the reluctivity versus the square of magnetic flux density is computed and illustrated in Figure 2.6.

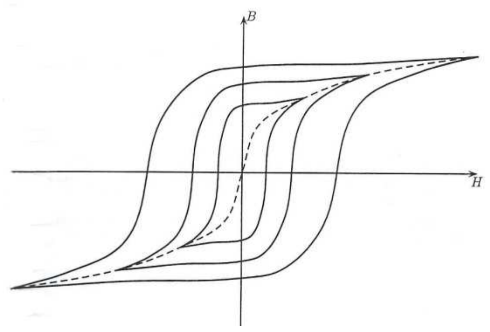

Figure 2.4 Hysteresis curves and normal magnetization curve

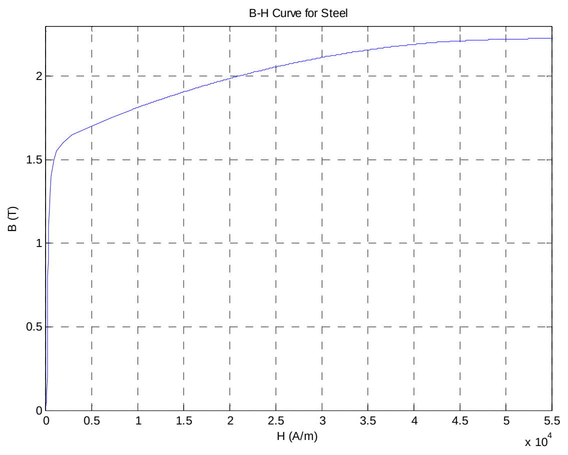

Figure 2.5 Nonlinear B-H curve for steel

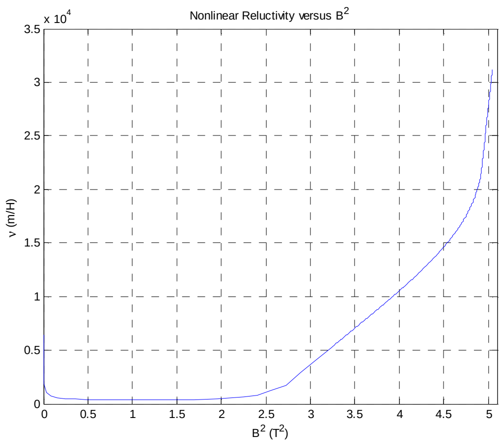

Figure 2.6 Nonlinear reluctivity versus square of magnetic flux density for steel

As previously referenced, a time-domain simulation is preferred to accurately simulate how nonlinear magnetic material affects the magnetic flux density. An effective permeability approximation method based on average energy [3] can be used with the time-harmonic approach. The time-domain method allows permeability to vary throughout the domain at each instant in time, providing a more intuitive model of the nonlinearity of the magnetic permeability. Additionally, time-domain simulation can include permeability hysteretic effects.

To model the nonlinearity of reluctivity, an iterative process is used to find the solution that is consistent with the field solution. The process is summarized by first assuming an initial value, solving the system, then correcting the reluctivity based on magnetic flux density solution. This process continues until the change in either the magnetic vector potential or reluctivity is less than a specified tolerance.

A common method of linearizing the system of nonlinear equations is the Newton-Raphson method. For the nonlinear iterative solution, the existence and uniqueness of a unique stable mathematical solution requires that the magnetization curve be monotonically increasing with their first derivatives monotonically decreasing [7]. If the nonlinear function is monotonically increasing, the solution from the Newton-Raphson method will converge quadratically. The curve in Figure 2.4 is not monotonically increasing. In order to guarantee convergence, the reluctivity in the low flux density region can be approximated as constant. Most electric machinery is not designed to operate in this region in steady-state, so this approximation is acceptable. For applications where the low flux density behavior is important, the Newton-Raphson method may use the change in permeability from one iteration to the next as the convergence criterion rather than the change in magnetic vector potential [3].

A review of the Newton-Raphson method for a system of nonlinear equations follows. Consider a system of nonlinear equations

$$\overline{f}(\overline{x}) = 0 \tag{2.60}$$

where $\overline{f}$ represents a system of *n* equations, and $\overline{x}$ represents *n* variables $x_1, x_2, ..., x_n$. An estimate of the solution is $\overline{x}^{(k)}$. An initial guess is used as the solution to $\overline{x}^{(0)}$. The iteration number is represented by the superscript (*k*). The error is $\Delta\overline{x}^{(k)} = \overline{x}^{(k+1)} - \overline{x}^{(k)}$. The system of equations can at iteration $k+1$ can be represented by

$$\overline{f}(\overline{x}^{(k)} + \Delta\overline{x}^{(k)}) = 0 \tag{2.61}$$

This equation expanded in a Taylor series is

$$f_i(\overline{x}^{(k)} + \Delta\overline{x}^{(k)}) = f_i(\overline{x}^{(k)}) + \sum_{j=1}^{n} \left.\frac{\partial f_i}{\partial x_j}\right|_{\left(\overline{x}^{(k)}\right)} \Delta x_j^{(k)} + \sum_{j=1}^{n} O\left(\left(\Delta x_j^{(k)}\right)^2\right) = 0, \quad i = 1, 2, ..., n \tag{2.62}$$

Omitting the higher order term, this equation can be written in matrix form as

$$[J]_{n\times n}\left\{\Delta\overline{x}^{(k)}\right\}_{n\times 1} = -\left\{\overline{f}(\overline{x}^{(k)})\right\}_{n\times 1} \tag{2.63}$$

where the Jacobian matrix *J* is given by

$$[J]=\begin{bmatrix} \left.\frac{\partial f_1}{\partial x_1}\right|_{\left(\overline{x}^{(k)}\right)} & \left.\frac{\partial f_1}{\partial x_2}\right|_{\left(\overline{x}^{(k)}\right)} & \cdots & \left.\frac{\partial f_1}{\partial x_n}\right|_{\left(\overline{x}^{(k)}\right)} \\ \left.\frac{\partial f_2}{\partial x_1}\right|_{\left(\overline{x}^{(k)}\right)} & \left.\frac{\partial f_2}{\partial x_2}\right|_{\left(\overline{x}^{(k)}\right)} & \cdots & \left.\frac{\partial f_2}{\partial x_n}\right|_{\left(\overline{x}^{(k)}\right)} \\ \vdots & \vdots & \ddots & \vdots \\ \left.\frac{\partial f_n}{\partial x_1}\right|_{\left(\overline{x}^{(k)}\right)} & \left.\frac{\partial f_n}{\partial x_2}\right|_{\left(\overline{x}^{(k)}\right)} & \cdots & \left.\frac{\partial f_n}{\partial x_n}\right|_{\left(\overline{x}^{(k)}\right)} \end{bmatrix} \tag{2.64}$$

Equation (2.63) is solved for $\Delta\overline{x}^{(k)}$. Then, $\overline{x}^{(k+1)}$ is found by $\overline{x}^{(k+1)}=\overline{x}^{(k)}+\Delta\overline{x}^{(k)}$. The method continues to iterate until

$$\Delta\overline{x}^{(k)}<\varepsilon \tag{2.65}$$

where ε is a specified tolerance.

The Newton-Raphson method is applied to the time-discretized finite-element equation (2.44) to linearize the reluctivity. This derivation follows aspects of the magnetostatic and time-domain modeling linearization using the Newton-Raphson method in [3] with some modifications for handling second-order elements. The implementation of the Newton-Raphson method is slightly different depending on the element order. For first-order elements, the reluctivity is constant throughout each element, so the calculation of the Jacobian only involves the terms $\frac{\partial\nu}{\partial A_j}=\frac{\partial\nu}{\partial\mathbf{B}^2}\frac{\partial\mathbf{B}^2}{\partial A_j}$ for j = 1,2,3. **B** is the magnitude of the magnetic flux density calculated from *A*. More information about how **B** is calculated from *A* is included in section 2.6 about post-processing. For second-order elements, the reluctivity now varies throughout the element. Since reluctivity is not an analytical function of **B**, it is represented numerically as the reluctivity derived from **B** at each element node. In that case, the Jacobian involves $\frac{\partial \nu_i}{\partial A_j} = \frac{\partial \nu_i}{\partial \mathbf{B}^2}\frac{\partial \mathbf{B}^2}{\partial A_j}$ for *i, j* = 1,2,3,4,5,6.

2.6.1 Nonlinear formulation for first-order elements

Consider the time-discretized equation (2.44) per element for first-order elements.

$$\left[\nu^e\begin{bmatrix} s_{11} & s_{12} & s_{13} \\ s_{21} & s_{22} & s_{23} \\ s_{31} & s_{32} & s_{33}\end{bmatrix} + \begin{bmatrix} t_{11} & t_{12} & t_{13} \\ t_{21} & t_{22} & t_{23} \\ t_{31} & t_{32} & t_{33}\end{bmatrix}\right]\begin{Bmatrix}\hat{A}_1 \\ \hat{A}_2 \\ \hat{A}_3\end{Bmatrix}^{t+\Delta t} = \left[\begin{bmatrix} t_{11} & t_{12} & t_{13} \\ t_{21} & t_{22} & t_{23} \\ t_{31} & t_{32} & t_{33}\end{bmatrix} - \frac{1-\beta}{\beta}\nu^e\begin{bmatrix} s_{11} & s_{12} & s_{13} \\ s_{21} & s_{22} & s_{23} \\ s_{31} & s_{32} & s_{33}\end{bmatrix}\right]\begin{Bmatrix}\hat{A}_1 \\ \hat{A}_2 \\ \hat{A}_3\end{Bmatrix}^{t} + \begin{Bmatrix}Q_1 \\ Q_2 \\ Q_3\end{Bmatrix}^{t+\Delta t} + \frac{1-\beta}{\beta}\begin{Bmatrix}Q_1 \\ Q_2 \\ Q_3\end{Bmatrix}^{t} \tag{2.66}$$

The subscripts denote local nodes 1, 2, and 3 for the element. Let $F_i,\ i=1,2,3$ denote the *i*th equation.

$$F_i = \left[\nu^e\left[s_{i1} \quad s_{i2} \quad s_{i3}\right] + \left[t_{i1} \quad t_{i2} \quad t_{i3}\right]\right]\begin{Bmatrix}\hat{A}_1 \\ \hat{A}_2 \\ \hat{A}_3\end{Bmatrix}^{t+\Delta t} - \left[\left[t_{i1} \quad t_{i2} \quad t_{i3}\right] - \frac{1-\beta}{\beta}\nu^e\left[s_{i1} \quad s_{i2} \quad s_{i3}\right]\right]\begin{Bmatrix}\hat{A}_1 \\ \hat{A}_2 \\ \hat{A}_3\end{Bmatrix}^{t} - Q_i^{t+\Delta t} - \frac{1-\beta}{\beta}Q_i^{t} \tag{2.67}$$

To find the derivatives necessary to form the Jacobian, equation (2.67) is differentiated with respect to the nodal magnetic vector potential. Using the product and chain rules, the result is

$$\frac{\partial F_i}{\partial A_j^{t+\Delta t}} = \nu^e s_{ij} + t_{ij} + \left(\sum_{q=1}^{3} s_{iq}A_q^{t+\Delta t}\right)\frac{\partial \nu^e}{\partial B^{e2}}\frac{\partial B^{e2}}{\partial A_j} \tag{2.68}$$

for $i, j = 1, 2, 3.$ The *i*th Newton-Raphson equation is

$$\begin{bmatrix} \dfrac{\partial F_i}{\partial A_1^{t+\Delta t}} & \dfrac{\partial F_i}{\partial A_2^{t+\Delta t}} & \dfrac{\partial F_i}{\partial A_3^{t+\Delta t}} \end{bmatrix} \begin{Bmatrix} \Delta A_1 \\ \Delta A_2 \\ \Delta A_3 \end{Bmatrix}^{t+\Delta t} = -F_i \tag{2.69}$$

This can be written in matrix notation per element as

$$\begin{aligned} &\left[\nu_k^{t+\Delta t}[S]+[T]+[G]_k^{t+\Delta t}\right]\{\Delta A\}_k^{t+\Delta t} = \\ &\quad -\left[\nu_k^{t+\Delta t}[S]+[T]\right]\{A\}_k^{t+\Delta t} + \left[[T]-\frac{1-\beta}{\beta}\nu^t[S]\right]\{A\}^t + \{Q\}^{t+\Delta t} + \frac{1-\beta}{\beta}\{Q\}^t \end{aligned} \tag{2.70}$$

where

$$[G]_k^{t+\Delta t} = \frac{\partial \nu_k^{e,t+\Delta t}}{\partial\left(B_k^{e,t+\Delta t}\right)^2} \begin{bmatrix} \sum_{q=1}^{3} s_{1q}A_q & \sum_{q=1}^{3} s_{1q}A_q & \sum_{q=1}^{3} s_{1q}A_q \\ \sum_{q=1}^{3} s_{2q}A_q & \sum_{q=1}^{3} s_{2q}A_q & \sum_{q=1}^{3} s_{2q}A_q \\ \sum_{q=1}^{3} s_{3q}A_q & \sum_{q=1}^{3} s_{3q}A_q & \sum_{q=1}^{3} s_{3q}A_q \end{bmatrix}_k^{t+\Delta t} \begin{bmatrix} \dfrac{\partial B^{e2}}{\partial A_1} & 0 & 0 \\ 0 & \dfrac{\partial B^{e2}}{\partial A_2} & 0 \\ 0 & 0 & \dfrac{\partial B^{e2}}{\partial A_3} \end{bmatrix}_k^{t+\Delta t} \tag{2.71}$$

Note the "hats" are dropped from the nodal magnetic vector potential, but it is understood that those values are estimated values. All values at time $t+\Delta t$ are the *k*th iteration values. The Newton-Raphson equations for each are assembled to obtain a global system of equations.

For each time step, the Newton-Raphson iteration process can be summarized as follows:

1. Start with an initial guess $A = A_0$. When solving for $A^{t+\Delta t}$, set $A_1^{t+\Delta t} = A^t$.

2. Calculate $B_k^{e,t+\Delta t}, \nu_k^{e,t+\Delta t},$ and the Jacobian values in equations (2.70) and (2.71) from $A_k^{t+\Delta t}$ values.

3. Assemble global matrices from element values according to equation (2.70) and (2.71).

4. Solve linear system of equations for $\{\Delta A\}_k^{t+\Delta t}$.

5. Update $A_{k+1}^{t+\Delta t} = A_k^{t+\Delta t} + \Delta A_k^{t+\Delta t}$. (2.72)

6. If $\left\|\Delta A_k^{t+\Delta t}\right\| < \varepsilon$, stop the iteration process and set $A^{t+\Delta t} = A_{k+1}^{t+\Delta t}$. Otherwise, repeat the iteration process from step 2 and continue.

Several calculations are required for step 2. The value of $\nu_k^{t+\Delta t}$ is calculated by first determining $B_k^{t+\Delta t}$ from equation (2.46), then determining the value of $\nu_k^{t+\Delta t}$ according to the non-linear $\nu - B^2$ curve at the point for $\left(B_k^{t+\Delta t}\right)^2$. Note that the Jacobian values in equation (2.71) are calculated differently for first- and second-order elements. The value of $\dfrac{\partial \nu_k^{e,t+\Delta t}}{\partial\left(B_k^{e,t+\Delta t}\right)^2}$ is determined by taking the derivative of the non-linear $\nu - B^2$ curve. The value of $\dfrac{\partial\left(B_k^{e,t+\Delta t}\right)^2}{\partial A_{i,k}^{t+\Delta t}}$, i = 1,2,3, for first-order elements is derived from equations (2.46) and (2.48) that describes **B** as a function of A_z. First, note that

$$B^{e2} = \left(\frac{\partial A_z}{\partial x}\right)^2 + \left(\frac{\partial A_z}{\partial y}\right)^2 \tag{2.73}$$

Squaring the *x*- and *y*-components of equation (2.48) and taking the derivative as a function of A_j for j = 1,2,3 yields

$$\frac{\partial\left(B_k^{e,t+\Delta t}\right)^2}{\partial A_{j,k}^{t+\Delta t}} = \frac{\gamma_j^e}{2\left(\Delta^e\right)^2}\sum_{i=1}^{3}\gamma_i^e A_{i,k}^{t+\Delta t} + \frac{\beta_j^e}{2\left(\Delta^e\right)^2}\sum_{i=1}^{3}\beta_i^e A_{i,k}^{t+\Delta t} \tag{2.74}$$

2.6.2 Nonlinear formulation for second-order elements

The author has not found specific implementation methods for modeling nonlinear second-order time-domain finite element methods. In [3], the nonlinear magnetostatic formulation is described for first-order elements, but not for second-order elements nor for the magnetodynamic (time-harmonic or time-domain) formulation. In [6], the linear two-dimensional time-harmonic formulation is described for first- and second-order elements, and the general time-domain discretization is discussed, but neither the nonlinear time-harmonic nor the nonlinear time-domain formulation for second-order elements is described. In [7], first- and second-order element implementations for the Helmholtz equation are described, first-order element solutions of the Newton-Raphson iterations are shown, and time- and frequency-domain problems are discussed including eddy-current analysis using magnetic vector potential, but the time-domain, nonlinear implementation for second-order or higher-order elements is not explicitly described. In [20] which is more mathematically based rather than application based for [3], [6], [7], higher-dimensional element formulation is presented, and iterative methods are discussed, but the application of second-order elements for a time-domain, nonlinear problem is not presented. The following formulation was derived for second-order elements as an extension of the nonlinear formulation for first-order elements.

For elements with nonlinear reluctivity which is a function of $\mathbf{B}^2$, and **B** depends on position within an element, reluctivity is also a function of position within an element and is no longer constant as it is for first-order elements. As a result, the finite element discretization, time discretization, and linearization should be repeated with elemental reluctivity replaced by $\nu(x,y)$. To numerically include the reluctivity variation within the element, the value of **B** is calculated at each local node per element. Then, using the local nodal **B** values, the reluctivity and corresponding $\dfrac{\partial \nu}{\partial B^2}$ at each local node belonging to elements in the nonlinear material region is calculated according to the nonlinear ν-$\mathbf{B}^2$ curve for the magnetic material. If an analytical expression is available for the *v*-**B**^{2} relationship, it may be analytically possible to determine the variation of *v* across the element. In this case, a value and gradient could be assigned at each local node per element. As seen in the example *v*-**B**^{2} in Figure 2.6, the derivative of this curve is constant for certain ranges of **B**^{2}. The reluctivity at each node belonging to elements in the linear material region is assigned according to the relative reluctivity to that region. For elements in the linear material region, the reluctivity is constant throughout the element.

With the reluctivity variation in mind, the matrix defined by equation (2.37) is redefined by replacing ν^e with ν_i^e. In this way, the finite element formulation is still the same as for first-order elements, but a variation in reluctivity within an element is included.

The nonlinear finite-element formulation is the same as first-order elements except the Jacobian values are different because reluctivity varies at each node. The Jacobian values become

$$\frac{\partial F_i}{\partial A_j^{t+\Delta t}} = \nu_i s_{ij} + t_{ij} + \left(\sum_{q=1}^{6} s_{iq} A_q^{\,t+\Delta t} \right) \frac{\partial \nu_i}{\partial B_i^2} \frac{\partial B_i^2}{\partial A_j} \tag{2.75}$$

for $i, j = 1, 2, ..., 6.$ The Newton-Raphson equation can be written in matrix notation per element as

$$\begin{aligned} &\left[diag[\nu]_k^{t+\Delta t} [S] + [T] + [G]_k^{t+\Delta t} \right] \{\Delta A\}_k^{t+\Delta t} = \\ &-\left[diag[\nu]_k^{t+\Delta t} [S] + [T] \right] \{A\}_k^{t+\Delta t} + \left[[T] - \frac{1-\beta}{\beta} diag[\nu]^t [S] \right] \{A\}^t + \{Q\}^{t+\Delta t} + \frac{1-\beta}{\beta} \{Q\}^t \end{aligned} \tag{2.76}$$

where

$$G_{ij,k}^{\,t+\Delta t} = \left[\frac{\partial \nu_i}{\partial B_i^2} \left(\sum_{q=1}^{6} s_{iq} A_q \right) \frac{\partial B_i^2}{\partial A_j} \right]_k^{t+\Delta t} \tag{2.77}$$

The value of $\nu_{i,k}^{t+\Delta t}$ is calculated in the same manner as for first-order elements by first determining $B_{i,k}^{t+\Delta t}$ from equation (2.46), then determining the value of $\nu_{i,k}^{t+\Delta t}$ according to the non-linear $\nu - B^2$

curve at the point for $\left(B_{i,k}^{t+\Delta t}\right)^2$. The value of $\dfrac{\partial \nu_{i,k}^{t+\Delta t}}{\partial \left(B_{i,k}^{t+\Delta t}\right)^2}$ is determined by taking the derivative of the non-linear $\nu - B^2$ curve. The value of $\dfrac{\partial \left(B_{i,k}^{t+\Delta t}\right)^2}{\partial A_{j,k}^{t+\Delta t}}$, *i*,*j* = 1,2,…,6 for second-order elements is derived from equations (2.46), (2.49), and (2.50) that describe **B** as a function of A_z. First, note that

$$B^2 = \left(\frac{\partial A_z}{\partial x}\right)^2 + \left(\frac{\partial A_z}{\partial y}\right)^2 \tag{2.78}$$

Rewriting equations (2.49) and (2.50) to simplify these expressions,

$$\begin{aligned} B_x^e = &\sum_{i=1}^{3}\left(\frac{1}{\left(\Delta^e\right)^2}\left(\gamma_i^e\left(\alpha_i^e+\beta_i^e x+\gamma_i^e y\right)\right)-\frac{\gamma_i^e}{2\Delta^e}\right)\hat{A}_i + \\ &\left(\frac{1}{\left(\Delta^e\right)^2}\left(\gamma_2^e\left(\alpha_1^e+\beta_1^e x+\gamma_1^e y\right)+\gamma_1^e\left(\alpha_2^e+\beta_2^e x+\gamma_2^e y\right)\right)\right)\hat{A}_4 + \\ &\left(\frac{1}{\left(\Delta^e\right)^2}\left(\gamma_3^e\left(\alpha_2^e+\beta_2^e x+\gamma_2^e y\right)+\gamma_2^e\left(\alpha_3^e+\beta_3^e x+\gamma_3^e y\right)\right)\right)\hat{A}_5 + \\ &\left(\frac{1}{\left(\Delta^e\right)^2}\left(\gamma_3^e\left(\alpha_1^e+\beta_1^e x+\gamma_1^e y\right)+\gamma_1^e\left(\alpha_3^e+\beta_3^e x+\gamma_3^e y\right)\right)\right)\hat{A}_6 \\ = &\sum_{m=1}^{6} f_m(x,y)\hat{A}_m \end{aligned} \tag{2.79}$$

$$
\begin{aligned}
B_y^e = &-\sum_{i=1}^{3}\left(\frac{1}{\left(\Delta^e\right)^2}\left(\beta_i^e\left(\alpha_i^e+\beta_i^e x+\gamma_i^e y\right)\right)-\frac{\gamma_i^e}{2\Delta^e}\right)\hat{A}_i - \\
&\left(\frac{1}{\left(\Delta^e\right)^2}\left(\beta_2^e\left(\alpha_1^e+\beta_1^e x+\gamma_1^e y\right)+\beta_1^e\left(\alpha_2^e+\beta_2^e x+\gamma_2^e y\right)\right)\right)\hat{A}_4 - \\
&\left(\frac{1}{\left(\Delta^e\right)^2}\left(\beta_3^e\left(\alpha_2^e+\beta_2^e x+\gamma_2^e y\right)+\beta_2^e\left(\alpha_3^e+\beta_3^e x+\gamma_3^e y\right)\right)\right)\hat{A}_5 - \\
&\left(\frac{1}{\left(\Delta^e\right)^2}\left(\beta_3^e\left(\alpha_1^e+\beta_1^e x+\gamma_1^e y\right)+\beta_1^e\left(\alpha_3^e+\beta_3^e x+\gamma_3^e y\right)\right)\right)\hat{A}_6 \\
= &\sum_{m=1}^{6} g_m(x,y)\hat{A}_m
\end{aligned}
\tag{2.80}
$$

Squaring the *x*- and *y*-components of **B** from equations (2.79) and (2.80) and taking the derivative as a function of A_j for j = 1,2,…,6 yields

$$
\frac{\partial\left(B_{i,k}^{t+\Delta t}\right)^2}{\partial A_{j,k}^{t+\Delta t}} = 2 f_j(x_i,y_i)\sum_{m=1}^{6} f_m(x_i,y_i)A_{m,k}^{t+\Delta t} + 2g_j(x_i,y_i)\sum_{m=1}^{6} g_m(x_i,y_i)A_{m,k}^{t+\Delta t} \tag{2.81}
$$

The Newton-Raphson equation for each element is assembled to obtain a global system of equations.

2.6.3 Relaxation factor

Rather than always updating the next iteration value of the nodal magnetic vector potential by , a relaxation factor α may be used according to

$$
A_{k+1}^{t+\Delta t} = A_k^{t+\Delta t} + \alpha\Delta A_k^{t+\Delta t} \tag{2.82}
$$

to either over-relax or under-relax the update. The updated value is over-relaxed if $\alpha > 1$, and this theoretically reduces the number of iterations to achieve convergence as long as the update does not overshoot the exact solution in which the method may not converge. The updated value is under-relaxed if $0 < \alpha < 1$. This may be necessary to achieve convergence with the Newton-Raphson method so that the next updated value does not overshoot the solution.

A method of determining the relaxation factor to find the value of α that minimizes the objective function in equation (2.83) which is a function of the Galerkin residual [21], [22]. The objective function is the sum of the values of the Galerkin residual each raised to the *n*th power. Objective functions to the second and fourth powers were explored. Equation (2.84) shows the Galerkin residual. Note that it is a function of the updated $A_{k+1}^{t+\Delta t}$ which is a function of α.

$$W_{k+1} = \sum_i \left\{ H_{i,k+1}^{t+\Delta t} \right\}^n \tag{2.83}$$

$$\mathrm{H}_{k+1}^{t+\Delta t} = \left[\nu_k^{t+\Delta t} [S] + [T] \right] \{A\}_{k+1}^{t+\Delta t} - \left[[T] - \frac{1-\beta}{\beta} \nu^t [S] \right] \{A\}^t - \{Q\}^{t+\Delta t} - \frac{1-\beta}{\beta} \{Q\}^t \tag{2.84}$$

The value of $\nu_k^{t+\Delta t}$ may be updated to the value of $\nu_{k+1}^{t+\Delta t}$ which is a function of $\{A\}_{k+1}^{t+\Delta t}$. This option was experimentally explored and did not seem to improve the convergence or reduce the number of iterations to achieve convergence. Additionally, updating the value of $\nu_{k+1}^{t+\Delta t}$ for each updated $\{A\}_{k+1}^{t+\Delta t}$ for the values of α examined $(\alpha = 0, 0.1, 0.2, \ldots, 2)$ increases the computation time of each iteration without necessarily any benefit. Instead, the relaxation factor α that allowed the solution value to achieve convergence was determined through numerical experiments for the specific problem. When an appropriate under-relaxation factor still does not yield a converged solution, the mesh may need to be refined.

2.7 Implementation

Each of the time-domain finite-element simulations was programmed for and run using MATLAB. While other programs, such as Maxwell Ansoft and JMAG, are available for finite element simulations of electric machines, a program needed to be created so that the lines of code could be manipulated in order to experiment with acceleration of the simulation. The time discretization used for each of these simulations is the Crank-Nicolson method with $\beta = 0.5$ according to equation (2.43).

In addition to the Neumann boundary condition applied in the derivation described in section 2.2 Finite Element Discretization, other boundary conditions must be applied to create a nonsingular global matrix and obtain a unique solution for the finite element problem [3]. At each point on the boundary of the mesh domain, the magnetic vector potential unknown or the normal derivative must be specified. Additionally, in order for the global matrix to be nonsingular, the magnetic vector potential must be defined for at least one specific node. For this application, the homogeneous Dirichlet boundary condition is applied, resulting that for all nodes on the boundary of the mesh domain, $A = 0$.

This section describes computer simulation implementation specifics for each type of problem – first or second order elements, and linear or nonlinear simulations. For all matrices and vectors stored and manipulated on the CPU, the MATLAB sparse matrix format is utilized to improve computational efficiency and reduce memory usage.

2.7.1 First-order, linear simulation

The first-order element mesh for the benchmark and induction machine simulation was generated using the MATLAB Partial Differential Equation (PDE) toolbox. This toolbox provides the ability to create a mesh using the Delaunay triangulation algorithm for a specified geometry. It generates a point matrix with the *x*- and *y*-coordinates of the points in the mesh, edge matrix, and triangle matrix describing the element triangle corner points in counterclockwise order and the corresponding element subdomain number.

For the simplest simulation using linear magnetic material and first-order elements, note that conductivity and reluctivity are constant throughout the element. From implementation of equation (2.44) using first-order matrices defined by equations (2.31)-(2.33), it is apparent that for a fixed geometry and linear reluctivity, the $[S]$ and $[T]$ matrices do not vary with time, but the magnetic vector potential and $\{Q\}$ vectors do vary with time. As a result, the $[S]$ and $[T]$ matrices only need to be computed once.

For a MATLAB script implementation, the $[S]$ and $[T]$ matrices are computed using the MATLAB sparse matrix format. For each element, the contributions from each node are calculated then summed over the elements to assemble the total $[S]$ and $[T]$ matrices. Because for first-order, linear simulations these matrices are only calculated once, they are computed on the CPU since the GPU will not yield a significant speed-up with this assembly, especially since the matrices are sparse.

For each time step, the solution for the next time-step value of the magnetic vector potential of equation (2.44) is solved for using the sparse iterative Krylov subspace solver biconjugate gradients stabilized method using a function that implements the biconjugate gradients stabilized method with preconditioner algorithm [11], [14], [17]. A similar MATLAB function “bicgstab” is also available for comparison. Several types of solvers for use with preconditioners are readily available functions in MATLAB. In addition to the biconjugate gradients stabilized method, the biconjugate gradients, conjugate gradients squared, generalized minimum residual, least squares, minimum residual, preconditioned conjugate gradients, quasi-minimal residual, and symmetric LQ methods are available MATLAB functions. For the first-order, linear simulation, each of these preconditioned solvers, except the quasi-minimal residual which was much slower, calculated the solution in similar times. The biconjugate gradients stabilized method is chosen as the solver for each type of simulation for consistency and calculation time comparison for different problem sizes. For the biconjugate gradients stabilitized method used, the solver tolerance was 10^{-5}. The MATLAB built-in function “ichol” to form the sparse incomplete Cholesky factorization was used to form the preconditioner. For this problem, the matrix is symmetric, positive definite, so the incomplete Cholesky factorization is a suitable preconditioner. The modified incomplete Cholesky, lower triangle preconditioner was formed using threshold dropping of tolerance 10^{-3}. Once the value for the magnetic vector potential was solved, the corresponding magnetic flux density per element was computed by equation (2.48), and the eddy current density was computed by equation (2.54)

2.7.2 Second-order, linear simulation

The second-order element mesh, specifically for the three additional nodes per element and edges between elements used to determine boundary nodes, was generated with the MATLAB PDE toolbox and the LehrFEM 2D finite element toolbox [23].

The second-order linear simulation follows the same simulation process as the first-order linear simulation except with second-order defined matrices. These matrices are the [S] and [T] per equations (2.37) and (2.38). Additionally, the magnetic flux density is calculated for each local node per element according to equations (2.49) and (2.50). The same preconditioner was not used for the second-order linear simulation as for the first-order linear simulation since it did not result in a converging sparse iterative solution to the specified 10^{-5} tolerance. Instead, the lower triangular, unmodified incomplete Cholesky factorization with zero fill was used for the preconditioner.

2.7.3 First-order, nonlinear simulation

The nonlinear problem mesh is formed the same way as the linear problem mesh. The nonlinear reluctivity vs. B^2 and nonlinear $\frac{\partial \nu}{\partial B^2}$ vs. B^2 are each represented by a piecewise linear interpolation function according to the nonlinear magnetic material properties.

The nonlinear simulation is set up to solve equation (2.70) with equation (2.71) using the Newton-Raphson method to solve the nonlinear system of equations. The matrices $[T]$ and $[S]$ without the associated ν are computed once at the beginning of the simulation. The nonlinear iterative process outlined in section 2.6, Nonlinear Formulation, is implemented. For first-order elements, the magnetic flux density and reluctivity are constant throughout the element and are thus assigned per element. The Newton-Raphson residual ε used was 10^{-6}. The incomplete Cholesky factorization preconditioner resulted in pivoting errors when it was called to compute and did not enable the biconjugate gradient stabilized solver to converge. Instead, the sparse incomplete LU factorization preconditioner was used according to the MATLAB function "ilu." The row-sum modified incomplete LU Crout version factorization with drop tolerance 10^{-5} was used and resulted in converged solutions for the biconjugate gradient stabilized solver. The sparse iterative linear solver tolerance was 10^{-5}.

An under-relaxation factor according to equation (2.82) was used for each Newton-Raphson iteration and time step. The value of the relaxation factor was determined experimentally using the value closest to 1 but still allowing the Newton-Raphson iteration to converge and not overstep the solution. This approach minimizes the number of Newton-Raphson iterations while still resulting in a converging solution.

In addition to the relaxation factor, the element size and time step difference Δt affect the Newton-Raphson convergence. For the first-order, nonlinear simulation, both coarse and fine meshes for the benchmark problem and Δt = 1 ms result in a converged solution.

2.7.4 Second-order, nonlinear simulation

The second-order, nonlinear simulation follows the same process as for the first-order, nonlinear simulation. The second-order matrices were computed according to equations (2.37), (2.38), (2.39), (2.76), (2.77), and (2.81). As described previously, the nonlinear reluctivity and resulting $\frac{\partial \nu}{\partial B^2}$ and $\frac{\partial B^2}{\partial A}$ are computed for each local node per element. The magnetic flux density is calculated for second-order elements by equations (2.49)-(2.51). The same incomplete LU factorization type of preconditioner and iterative solver used for the first-order, nonlinear simulation was used for this simulation.

The second-order, nonlinear simulation had Newton-Raphson convergence issues that did not arise for the other simulation types. For the benchmark problem, the coarse mesh problem could only converge for Δt = 1 ms for simulation times 1-4 ms. Beyond that, smaller Δt values had to be used in order for the Newton-Rapshon iterations to converge to the 10^{-6} residual. Solutions were calculated up to 27.487 ms with a Δt = 0.001 ms. For subsequent times, it was determined that for a reasonable computation time, the fine mesh needed to be used in order to achieve convergence for a larger Δt .

For the benchmark problem fine mesh, the solution converged for Δt =1 ms for times 1-18 ms. For subsequent times, Δt =0.5 ms resulted in converged solutions for times 18-20 ms, and Δt =0.1 ms resulted in converged solutions for times 20-21.7 ms. The remaining part of the simulation was not conducted due to the nonlinear convergence problems. Results are presented for times 1-18 ms to show scalability of the GPU solution.

For the linear induction machine problem, the large air gap and excitation resulted in the operation of the magnetic material in the linear region. Nonlinear problem solutions did achieve convergence for the M19 steel representation using continuous analytical functions to represent ν-$\mathbf{B}^2$ and $\frac{\partial \nu}{\partial B^2}$. However, the results were similar to the linear magnetic material results, so they are not presented.

A complete nonlinear solution of the benchmark problem is available for the first-order elements, but not for the second-order elements due to the nonlinear convergence problem. This convergence issue could potentially be resolved by using an even smaller Δt, finer mesh, or a continuous analytical expression of the nonlinear magnetic material properties instead of the piecewise linear representation. For electric machine design and analysis problems, the higher-order element simulations with nonlinear magnetic material should result in higher fidelity solutions than for first-order elements. As part of the tradeoff of simulation detail and computation time, the higher-order element simulations require a smaller time step or finer mesh than the first-order element simulations to achieve convergence, resulting in a longer computation time. This trade-off may be reasonable when detailed simulation results are desired, such as for magnetic material saturation near tooth tips.

CHAPTER 3
ACCELERATING THE FINITE ELEMENT SIMULATION

3.1 Methods of Accelerating Finite Element Simulations

The finite element simulation of a low-frequency nonlinear electromagnetic problem can be accelerated using a numerical or parallel computing method or both. The Shooting-Newton [4] numerical method was investigated. Multi-core and GPU parallel computation methods were also studied.

3.1.1 Numerical methods

When the steady-state analysis of an electromagnetic problem is desired, there are numerical approaches, such as the shooting-Newton method [4], that can be utilized. Additionally, domain decomposition techniques can be utilized to subdivide the problem for different processing techniques [5].

Methods for steady-state analysis reduce the need for a transient solution to achieve the steady-state solution. For an induction machine, eddy current is represented through transient analysis. For different machine topologies such as permanent magnet synchronous machines, steady-state analysis can be utilized for machine nominal performance design.

One approach of the shooting-Newton method, which requires Gaussian elimination, assessed for simulation acceleration involves a matrix-free Krylov-subspace approach [4]. The shooting method approach is to find the periodic steady-state solution of the problem by comparing the computed solution at the end of the period and determining if it matches the initial condition at the start of the period. The method outlined in [4] was experimented for the benchmark problem later presented. For this specific type of finite element analysis, this method did not appear to reduce the computation time because the numerical integration required a small change in time, resulting in a longer computation time than the transient finite element analysis formulation.

3.1.2 Parallel processing methods

3.1.2.1 Multiple core

Multiple-core processors provide a means to accelerate certain simulations such as ordinary differential equations. For an implementation in which each equation is independent, not related to the solution of a separate set of equations or other variables, and can be implemented in any order, the solution of these equations is easily solved in parallel. For the time-domain finite element simulation, each time step of the solution must be computed sequentially, but it may be possible to decompose the domain for each time step and compute the solution of each subsection in parallel [5].

For example, MathWorks has developed a parallel for-loop that enables parallel for-loop implementation across each core of a processor [24], [25]. The parallel ordinary differential equation example describes the use of the parallel for-loop to solve a parameter sweep study of a second-order ODE system [26]. First, the example solves 3500 ODEs in serial using the ode45 solver. Then, the example solves the same number of ODEs using the parallel for-loop. For a processor with four cores, the speed-up of this example is tested to be approximately 3.63, which is nearly linearly proportional to the number of cores. This is due to the fact that this loop has minimal overhead in terms of data transfer.

Another means of multi-core processing and parallel loops is using single program multiple data (SPMD) [27]. This type of processing is suitable for simulations that can be implemented in any order and be solved in parallel. SPMD is a shared-memory approach using message passing. One task per processor is executed, and each processor executes the same code. In this way, a parallel loop can be implemented. An API readily available for shared memory multiprocessing is Open Multi-Processing (OpenMP). It provides a means of multithread processing whereby a block of code is executed in parallel [27].

Message Passing Interface (MPI) is a message-passing communication protocol developed for parallel programming such as scalable cluster computing [27]. The computing nodes do not share memory and interact through message passing. Programs that use MPI use a set of routines callable from several types of programming languages, making MPI portable.

There are several examples from the literature about parallel processing applied to finite element simulations using MPI and domain decomposition (DD) [5], [28], [29], [30], [31]. Applications of such simulations include structural dynamics and electromagnetic simulation of electric machines. The application described in this thesis is the time-domain, nonlinear simulation of an induction machine in two dimensions for a fixed position. The time domain simulation of this problem is essential in order to simulate the eddy currents of the induction machine. Examples from the literature include aspects of this type of simulation but not all in a single simulation using one or more parallel processing methods.

A simulation by engineers in Tokyo [30] describes a method to parallelize the 2D, steady-state analysis of nonlinear induction machine magnetic fields. The approach, called the parallel time-periodic finite-element method (PTPFEM), parallelizes the simulation in the time-axis direction rather than in each time step. The simulation approach taken in this thesis and typical with domain decomposition is by each time step. By solving the equations for all nonlinear unknowns at every time step for a period simultaneously, the problem is posed for a larger number of equations which lends itself to greater speed up from parallelization in this approach. This is useful for the steady-state analysis of the induction machine and not the transient. This thesis does not necessarily focus on the steady-state simulation of the induction machine. In the early stages of a machine design, it may be beneficial to understand the steady-state behavior of the machine. In this case, an approach such as this may be useful. The authors use MPI communications for the parallel processing. The BiCGstab2 method and localized ILU preconditioning are used. To stabilize the convergence of the Newton-Raphson method, the authors apply the line search based on the minimization of energy function. The authors claim, but do not quantify, that the communication overhead associated with domain decomposition for parallel performance causes the performance to suffer for small scale analysis. The example simulation described for an induction machine includes 13,198 elements, 256 time steps to form a period, and 3,252,480 unknowns. A supercomputer is used for the simulation where each node consists of four AMD Opteron 8356 processors, and the backward Euler method is used for time integration. The PTPFEM simulation results were compared for 1, 8, 16, 32, 64, and 128 processes, as well as for the transient approach called the time-periodic explicit error correction method, which is a time-domain approach to find the steady-state solution faster than traditional time-domain approaches. For a slip of 1, the PTPFEM approach achieved a speed-up of 7.06, and for a slip of 0.0588, the PTPFEM approach sped up the solution by a factor of 8.4. The authors did not describe a means to parallelize the time-domain approach and compare those results to the PTPFEM approach. As the number of processes increases, the speed-up increases, showing the effectiveness of the PTPFEM approach for highly parallel computation.

Another example of the use of MPI was done by researchers at the University of Alberta [29]. A two-dimensional, transient, nonlinear simulation of an induction machine was implemented using the Newton-Raphson method for linearization and domain decomposition. The induction machine was simulated with an interbar rotor circuit model. The parallelization was done with three PCs using 3.2 GHz Pentium D processors and MPICH2. The problem was of similar size in this thesis for the first-order element simulation of the benchmark problem. In [29], the finite element simulation consisted of 1941 nodes and 3534 first-order elements per time step. For the simulation of 1000 time steps, three simulations were completed using different methods: the traditional Newton-Raphson (NR) method, NR method with domain decomposition, and parallelized NR with domain decomposition. The simulation times for these methods were 2270 s, 1581 s, and 395 s respectively. Comparing the serial and parallel NR with domain decomposition techniques, the parallelized simulation resulted in a speed-up of 4. Note also that domain decomposition resulted in a speed-up of 1.43, and comparing traditional NR with parallelized NR with DD resulted in a speed-up of 5.75. This may show that depending on the implementation of domain decomposition, further simulation speed-up may be obtained by using domain decomposition with parallel processing such as with MPI.

A variation of parallel processing using MPI for a domain decomposition technique for nonlinear dynamic finite element analysis was simulated for a structural dynamics problem [31]. The simulated problem requires the solution of second derivative differential equations, and the unconditionally stable Newmark-β method is used for the time integration of the problem. The parallel algorithm uses a method with overlapped domains with a predictor-corrector scheme. The parallel algorithm is implemented on a cluster workstation using MPI. The number of partitioned subdomains matches the number of processors. The algorithm was implemented for a mesh size with 4710 unknowns and for a finer mesh with 17,322 unknowns. The larger mesh size provides a slightly better speed-up than for a smaller mesh size, indicating the typical trend that the performance of the parallel algorithm improves with increase in problem size. For 8 processors, the smaller mesh speed-up was 4.7, and for the larger mesh the speed-up was approximately 5.

Researchers at the University of Tokyo and Kyushi University have also researched domain-decomposition techniques applied to electromagnetic finite-element simulation [28]. They applied the Heirarchical Domain Decomposition Method (HDDM) to a 3D nonlinear magnetostatic problem. The domain decomposition technique allowed them to use parallel computing with a supercomputer consisting of 64 nodes and 1024 cores. They investigated different magnitudes of convergence criterion of two iterative solvers and how that affects the computation time and convergence of the subdomain interface problem. The two iterative solvers compared are the incomplete Cholesky-conjugate gradient method with shifted incomplete Cholesky factorization preconditioner and the LU decomposition with pivoting. The specific speed-up of the domain decomposition problem solved by the Supercomputer is not specified, but they indicate that the problem had 1.2 billion degrees of freedom and solved in 4.8 hours with approximately 80% of the time dedicated to computing and 16% of the time to communication. A sequential solution for a smaller problem with 100 million degrees of freedom was solved in 4.5 hours. Assuming the supercomputer can solve the smaller 100 million degrees of freedom problem in a proportional amount of time (which is not the case – the communication overhead will likely increase), then the supercomputer may be able to solve this problem in 0.32 hours, resulting in a potential speed-up of 14 due to the application of domain decomposition to multiple cores and processors.

3.1.2.2 Graphical processing units

Graphical Processing Units (GPUs) can be utilized not only for graphics processing but also for parallel computing [32], [33]. A GPU may consist of hundreds of cores that can be utilized for multithreaded, single-instruction computation. Depending on the application, the numerous cores could yield a large speed-up compared to CPUs. The fundamental design differences between CPUs and GPUs can be utilized to achieve a faster simulation. Figure 3.1 from [33] illustrates the CPU and GPU design differences. The CPU is optimized for sequential execution with a larger amount of memory, while the GPU has higher bandwidth, approximately 10 times on average [32].

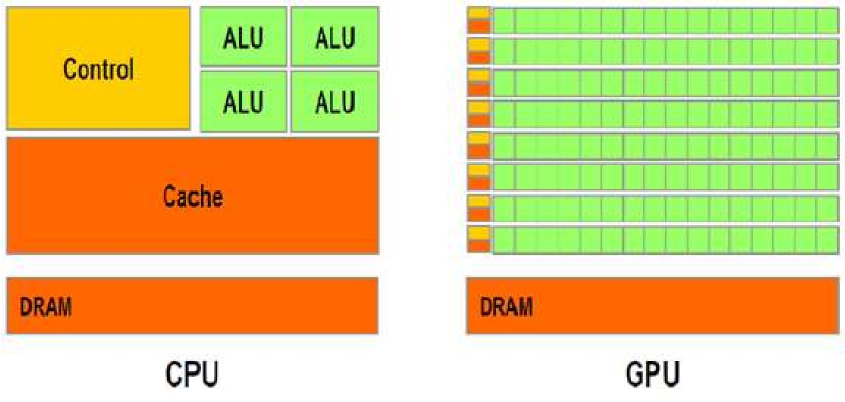

Figure 3.1 CPU and GPU design illustration [33]

The general architecture of a GPU is illustrated in Figure 3.2. Each block shows an array of highly threaded streaming multiprocessors. In each block, there are two streaming multiprocessors. Each of these has several streaming processors, represented by the green square.

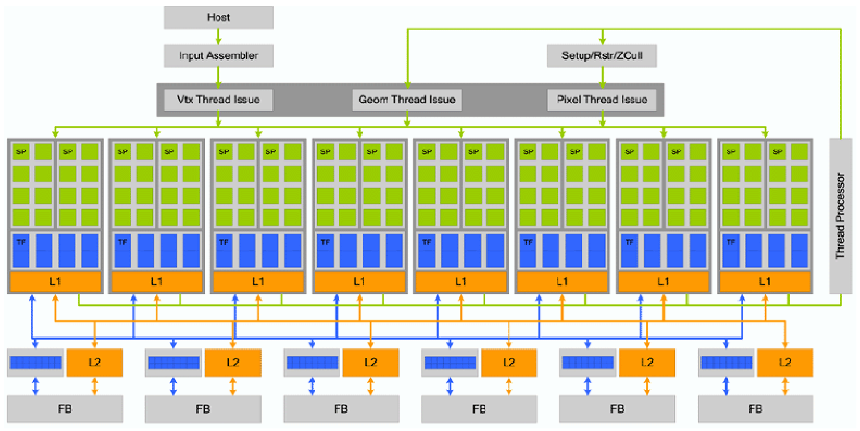

Figure 3.2 Example GPU architecture [34]

Figure 3.3 illustrates how the GPU memory, data transfer, and threads are structured. Each device is composed of multiple grids which contain multiple blocks. Each block contains multiple threads that can each be used to execute a single process. Each thread has access to local, global, and shared memory. The shared memory is shared among the threads in each block. The kernel function specifies the code that all threads should execute in parallel. This process is the SPMD process. When the kernel is launched, it executes the parallel threads in the grid [32]. To utilize the full capability of the GPU hardware, the threads should be adequately allocated to maximize the parallelism.

The amount of speed-up that can be expected from GPU parallel processing depends on the portion of the application that can be computed in parallel [32]. In most applications, only a portion of the problem can be computed in parallel. Additionally, a practical speed-up ceiling exists, such as a possible maximum of 100 times speed-up, which limits the expected simulation speed-up.

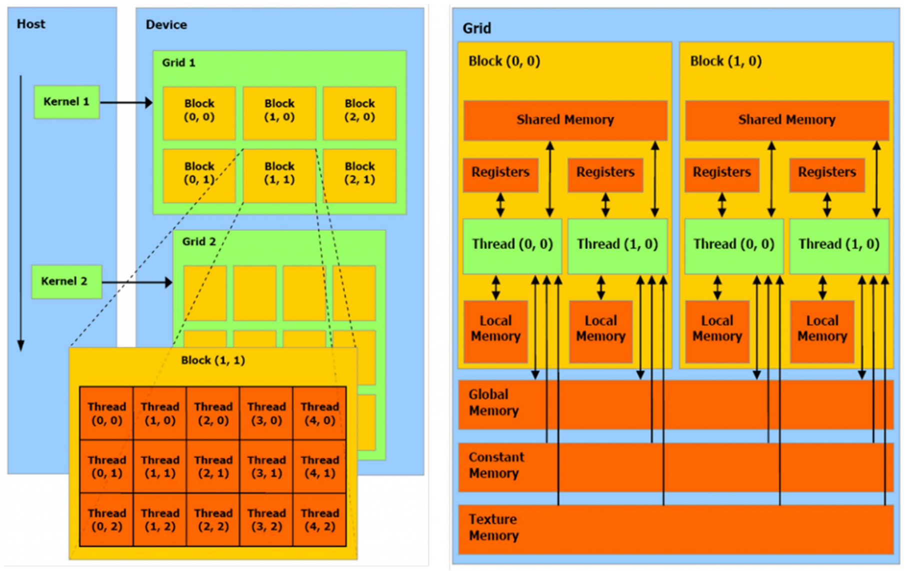

Figure 3.3 Abstract representation of GPU structure [33], [32]

Interaction between the CPU and GPU within a program is similar to message passing since there is limited shared memory between the processors. The data transfer between the CPU and GPU thus contributes to the overhead of a hybrid CPU/GPU simulation and should be minimized [32].

3.2 GPU Parallel Processing for the Finite Element Simulation

3.2.1 Components of FEA suitable for GPU parallel processing

There are several components in the finite element simulation, some of which may be suitable for parallel processing and some which may not be. The components that are suitable are parts where the computation can be distributed to multiple processors for parallel processing, then reassembled for the domain solution to that component. The time-domain finite element simulation for eddy-current problems requires the solution for each time step to be computed, and the previous time step solution is required for the next time step computation. Thus, multiple time steps cannot be distributed for parallel processing; one time step at a time must be considered unless a different numerical method is used. Within each time step, there are several components to the finite element simulation, as discussed in section 2.3 Time Discretization, section 2.6 Nonlinear Formulation, and section 2.7 Implementation.

1. Matrix assembly
2. Matrix multiplication: Magnetic flux density calculation (post processing for linear formulation, used to determine nonlinear reluctivity for nonlinear formulation)
3. Matrix multiplication: $[G]_k^{t+\Delta t}$ for nonlinear formulation only based on nonlinear reluctivity

4. Solution of the next time step $\{A\}^{t+\Delta t}$ for the linear formulation, or iteration $\{\Delta A\}_k^{t+\Delta t}$ for the nonlinear formulation. Solution is computed using a sparse iterative solver with preconditioner.
5. Nonlinear reluctivity and $\frac{\partial \nu}{\partial B^2}$ determination based on $\nu - B^2$ for nonlinear magnetic material only
6. Post processing: eddy current density, force calculation using multiplication

The finite-element mesh creation and assembly prior to computations for the magnetic vector potential are not considered.

In addition to identifying the components where GPU parallel processing can speed up the simulation, the CPU computation time percentage of each component should be understood. To gain the most speed-up, ideally the components that require the longest computation time should lend themselves to GPU parallel processing. In Chapter 4, Simulation of the Benchmark Problem, the component computation time will be discussed for the linear and nonlinear formulation for different mesh densities. The component with the longest computation time is formulation of the preconditioner and sparse iterative solver solution, followed by matrix multiplication for the magnetic flux density and $[G]_k^{t+\Delta t}$, with the remaining components of matrix assembly, nonlinear reluctivity determination, and eddy current density calculations requiring the shortest computation times.

With the sparse iterative solver and matrix multiplications requiring longer computation time than the other components, these components were chosen to study how GPUs can be used for parallel processing with the goal to provide speed-up relative to the CPU simulation. The remaining components are left on the CPU to form a hybrid CPU/GPU MATLAB-based simulation. In particular, the MATLAB sparse matrix assembly and storage yields fast computation times not readily achievable with the gpuArray format. There are numerous research efforts that have studied how GPUs can be used for sparse matrix-vector multiplication and sparse iterative solvers [35], [36], [37], [38], [39], [40], [41], [42], as is discussed in section 3.2.2.1 NVIDIA CUDA. This research studies how GPUs can be used to speed up these components to form a hybrid CPU/GPU desktop-based MATLAB simulation for the time-domain finite element analysis required for detailed electromagnetic induction machine analysis.

3.2.2 Implementation methods for GPU parallel processing for FEA

Several programming languages are available to use GPUs for parallel computing, including OpenGL, OpenCL, Compute Unified Device Architecture (CUDA), and higher-level language tools such as the parallel computing toolbox with MATLAB script programming language. OpenGL is utilized for graphics programming and requires in-depth knowledge of the programming language. CUDA, developed by NVIDIA, is an extension of C. This makes it more accessible to programmers without the need to know graphics programming. This section focuses on the use of CUDA, MATLAB extensions, and the MATLAB parallel computing toolbox.

3.2.2.1 NVIDIA CUDA

CUDA is a C-based programming language that extends C-programming for use with GPUs for scientific parallel computing. In addition to the CUDA language, libraries have been built to allow functions to be accessible to the average programmer and expand the use of CUDA. In particular, for CUDA used for numerical solutions of partial differential equations, such as for electromagnetic finite element simulation, the sparse linear algebra library CUSP [43] and cuSPARSE library [44] provide useful functions. CUSP expands the Basic Linear Algebra Library

(BLAS) to apply linear algebra to sparse matrices. It supports several sparse matrix formats: coordinate (COO) storage of sparse matrices (similar to sparse matrix storage in MATLAB), compressed sparse row (CSR), diagonal (DIA), ell (ELL), and hybrid (HYB). According to NVIDIA, the diagonal and ell formats are the most efficient for computing sparse matrix-vector products, and therefore are the fastest formats for solving sparse linear systems with iterative methods, such as the conjugate gradient method. The coordinate and CSR formats are more flexible than DIA and ELL and easier to manipulate. Additional useful functions within the CUSP library are preconditioners and iterative solvers. Iterative solvers include the conjugate-gradient, biconjugate gradient, biconjugate gradient stabilized, generalized minimum residual, multi-mass conjugate gradient, and multi-mass biconjugate gradient stabilized. CUSP provides the preconditioners algebraic multigrid based on smoothed aggregation, approximate inverse, and diagonal.

A comparison of ILU and Cholesky preconditioned iterative methods using CUSPARSE and CUBLAS was made by researchers with NVIDIA [35]. Numerical experiments with the incomplete factorization performed on the CPU and iterative method on the GPU were conducted. The experiment shows that the ILU and Cholesky preconditioned iterative methods achieved an average of two times speed-up using the CUSPARSE and CUBLAS libraries on the GPU over the MKL implementation on the CPU. The test matrices ranged from square matrix sizes with 147,900 to 1,585,478 rows and columns, and the number of nonzero elements of the test matrices ranged from approximately 1 to 17 million. The speed-up for different problems ranged from less than 1 to 5.5 and is highly dependent on the sparsity pattern of the coefficient matrix. For each iteration of the incomplete-Cholesky preconditioned CG method, one sparse matrix-vector multiplication and two triangular solves are performed. For each iteration of the incomplete-LU preconditioned BiCGStab iterative method, two sparse matrix-vector multiplications and four triangular solves are performed. The total speed-up that can be achieved for a complete solution will depend on the preconditioning time and number of iterations, not just the computation required to perform one iteration. The majority of the computation time for both of these iterative methods is spent for the triangular solve. Generally, the speed-up was greater for solutions requiring a larger number of iterations and for less dense factorization. Denser factorization inhibits the parallelism of these algorithms due to the dependence between rows in the sparse triangular solver.

In [36], the authors also explore the use of GPUs for sparse matrix-vector products and several preconditioning and iterative solver methods. Comparing CPU and GPU implementations of the sparse triangular solve, the use of *level scheduling* can result in an improved matrix structure more suitable for parallel computing. This type of sorting groups several unknowns into levels such that the unknowns for one level can be computed at the same time, or in parallel [11]. The ability of the GPU to speed up the computation of the parallel triangular solve depends on the number of levels. Minimization of the number of levels improves the GPU computation time speed-up. An example technique to reduce the number of levels is the Multiple Minimal Degree ordering [45]. The greatest speed-up achieved using the GPU level scheduling sparse triangular solve technique for the matrices tested was approximately 2.6 for a square matrix with 2.1 million nonzero elements for a matrix size 525,000 x 525,000. The preconditioned iterative methods considered were for the incomplete LU factorization, incomplete Cholesky factorization, block Jacobi preconditioner, multi-color SSOR, and least-squares polynomial preconditioner. Certain preconditioners were paired with the CG or GMRES iterative solver. For each of these experiments, in many cases the triangular solves in the preconditioner were computed on the CPU because the CPU computation time was faster than the GPU computation time. The greatest GPU speed-up achieved for the cases considered was 4.3 for the GPU-accelerated ILUT-GMRES method for the matrix with 8.8 million nonzeros for a matrix 1.27 million x 1.27 million. For the sparse matrices used for the numerical experiments, the GPUs can be used to speed up the computations, but their performance is limited for the sparse matrices compared to dense matrices.

3.2.2.2 MATLAB and extensions

There are several approaches to using GPUs with MATLAB script programs. With the parallel computing toolbox, there is a gpuArray type that readily allows the user to convert an array into this type and store the array on GPU as a full, single-precision array. This allows for direct manipulation of the gpuArray with the MATLAB script. Another option is the use of mex files to link a C, C++, or Fortran source file with the MATLAB program. This provides a means to pass MATLAB variables to and from this function. With CUDA being an extension of C, this readily allows the MATLAB program to call the CUDA program via the mex file. Additionally, a sparse gpuArray format was developed by MATLAB users as an extension of the gpuArray type to readily allow sparse matrix computation using gpuArray.

3.2.2.2.1 MATLAB gpuArray

A MATLAB gpuArray is stored on the GPU. Data can be created on the CPU and then transferred to the GPU, resulting in communication time overhead, or created on the GPU. This is accomplished using the gpuArray type. There are limitations to this type: the matrix must be non-sparse (full) and of the data type single, double, int8, int16, int32, int64, uint8, uint16, uint64, or logical. Thus, for problems well-suited to sparse matrix solvers, the use of GPUs and MATLAB built-in functions will not inherently provide a faster computational speed. MathWorks has adapted built-in functions to support the gpuArray type. For this list of functions, see Appendix D Built-In MATLAB Functions that Support GPUArray for MATLAB 2012A, and Appendix E Built-In MATLAB Functions that Support GPUArray for MATLAB 2014A. When one of these functions is called with at least one gpuArray input argument, the function is executed on the GPU and returns a gpuArray result.

An example of the use of gpuArrays with MATLAB functions to accelerate the matrix fast-Fourier transform (FFT) is the solution of the second-order wave equation using spectral methods [26]. The solution to the equation

$$\frac{\partial u}{\partial t} = \frac{\partial^2 u}{\partial x^2} + \frac{\partial^2 u}{\partial y^2}$$

with boundary conditions $u = 0$ is implemented using a second-order central finite difference in time, and a Chebyshev spectral method in space using the FFT. The implementations with CPUs and GPUs are identical with the exception of gpuArrays used for vectors and matrices for the GPU implementation. The *real*, *fft*, *ifft* and matrix multiplication functions are used with gpuArrays to accelerate the computation. The iteration is also calculated using element-wise multiplication, addition, and subtraction. Each time iteration solution depends on calculations for the previous and current iteration.   The previous iteration solution is merely saved in a gpuArray and stored in a separate matrix used to calculate the current solution. This previous time iteration solution does not need to be transferred between the CPU and GPU. Testing of this implementation with a CPU running Windows 7 SP1 with Intel core i5-2400 CPU @ 3.10 GHz, 4.00 GB RAM, 64-bit OS and with a GPU GeForce GTX 570 with 1024 threads per block and 15 multiprocessors, results in the computation speeds shown in Figure 3.4 and speed-up shown in Figure 3.5. As is expected, the speed-up improves as the grid size increases due to the reduced data storage overhead relative to computation time for larger problem sizes.

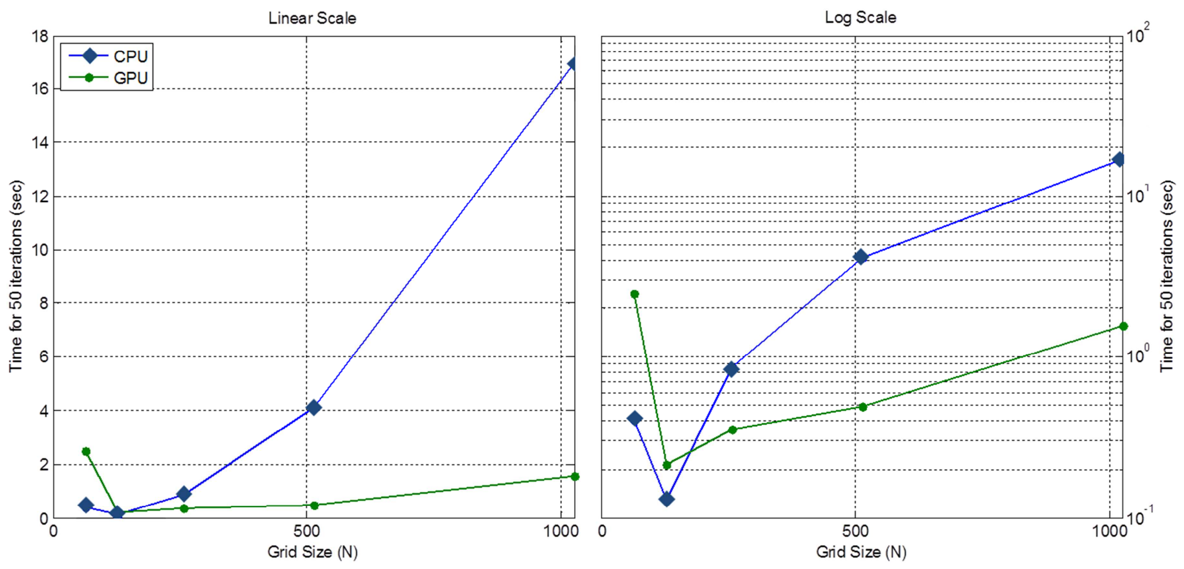

Figure 3.4 Computation speed for CPU and GPU simulations using MATLAB ifft function with gpuArrays

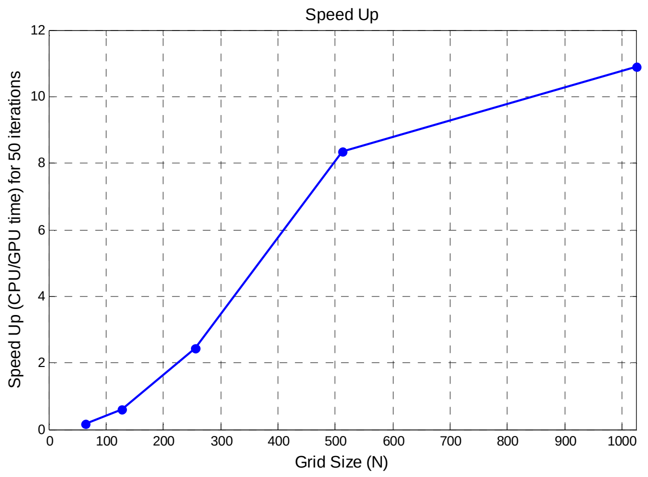

Figure 3.5 Speed-up for MATLAB ifft function with gpuArrays

Another benchmark example of GPUs to CPUs developed by MathWorks is the mldivide or backslash operator (\) used to calculate x from the system of equations $x = A\backslash b$ [24]. The time measured is only the computation time to calculate x; it does not include the cost of transferring data between the CPU and GPU or the time it takes to create a matrix. Note that since gpuArray matrices are only defined for full matrices, the A matrix used with mldivide is a full matrix.

Compared to CPU sparse matrix solutions with mldivide or CPU sparse iterative solvers, the full matrix gpuArray mldivide computation time is much longer. Figure 3.6 shows the calculated speed-ups for the mldivide function for several matrix sizes and single or double precision matrices. The computation time for these calculations was done with the same CPU and GPU as described for the previous example. Especially for single precision, the larger the matrix size, the greater the speed-up. These matrix sizes are multiples of 1024 which facilitates greater speed-up than for other multiples based on the single and double precision byte size. Although there are 15 processors available with the GeForce GTX 570, the speed-up for the largest matrix size with single precision is approximately 4. The speed-up achieved depends on the algorithm implementation.

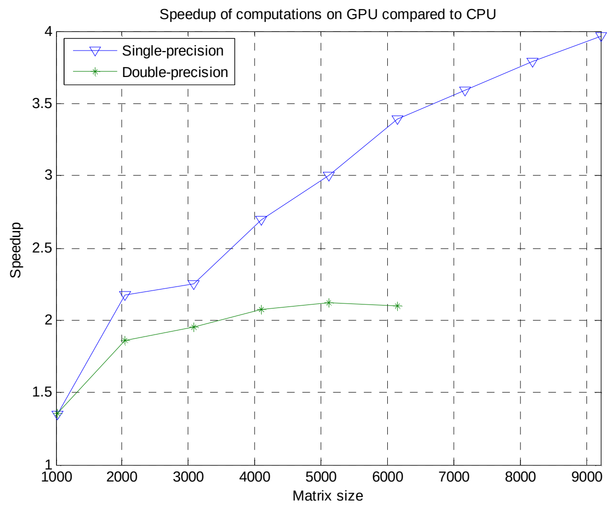

Figure 3.6 Speed-up results for single and double precision calculations for MATLAB mldivide

3.2.2.2.2 MATLAB and MEX files

MEX files can be used to link MATLAB arrays with C files. They provide a means to link CUDA code and libraries to gpuArray data on 64-bit platforms. Support for MEX files containing

CUDA code was developed for MATLAB version 2013a and later. Programs using C, C++, or CUDA with functions developed for external libraries can be linked to MATLAB data types and formats with the MEX files. Since the gpuArray type does not yet support a sparse matrix format, it is advantageous to make use of MEX files as a means to perform GPU computation in a sparse matrix format linking to already developed CUDA libraries enabling sparse computation of GPU data. As discussed in Section 3.2.2.1 NVIDIA CUDA, such sparse data and matrix CUDA libraries are CUBLAS, CUSP, and cuSPARSE. CUDA version 4.0 with CUSP version 0.4.0 and Thrust v1.2 is used in experimental simulations.

The entry point to the MEX-file is the mexFunction. The mexFunction contains the CUDA or C code that interacts with the MATLAB objects (on CPU or gpuArray) and runs the CUDA code. MEX files can allocate memory within the mexFunction. MATLAB links the mexFunction C or CUDA source file to MATLAB by compiling the source file into a binary MEX-file. The MEX-file only needs to be created once to compile the source file. For example, executing the command for the CUDA source file "cusp_solve.cu" containing the mexFunction,

```
mex –largeArrayDims cusp_solve.cu
```

will compile this CUDA source file into a binary MEX-file. From there, this source code can be executed with other MATLAB code similarly to a MATLAB function. MATLAB function or workspace variables can be passed into and out of this source code. The "largeArrayDims" option uses the MATLAB large-array-handling APLI and must be used when calling Linear Algebra Package (LAPACK) or Basic Linear Algebra Subprograms (BLAS) functions in the source file.

Alternatively, a MATLAB kernel object can be used to execute a CUDA thread. Files developed using the CUDA programming language (CU files or kernels) and PTX files can be executed on the GPU using MATLAB. PTX files are parallel thread execution files. The CU file must be compiled to create the PTX file using the nvcc compiler in the NVIDIA CUDA Toolkit. For example,

```
nvcc -ptx myfun.cu
```

generates the file named myfun.ptx. Using the .cu and .ptx files, a MATLAB kernel object can be created and used to evaluate the kernel

```
k = parallel.gpu.CUDAKernel('myfun.ptx', 'myfun.cu');
```

The feval function is then used to evaluate the kernel on the GPU. Inputs can be from the MATLAB workspace data on the CPU or gpuArray type. It may be more efficient to use gpuArray objects as inputs to the kernel. The outputs of the kernel evaluation are gpuArray. The CUDAKernel object is already compiled CUDA. Access to GPU memory must be pre-allocated before execution of the kernel. The evaluation of the kernel returns a gpuArray, so transfer is not required between the GPU and CPU.

3.2.2.2.3 Sparse gpuArray format

While the gpuArray format allows the user to readily convert CPU matrices and vectors to GPU matrices and vectors, the gpuArray format is limited. As stated previously, a limited number of MATLAB built-in functions are overloaded and useable with the gpuArray format. Additionally, as of the time of this research, the gpuArray format is only available for full vector and matrix formats. Only since MATLAB version R2015a has the gpuArray sparse format been available, and the only function available with this format that could increase GPU performance for the FEA problem is the matrix multiplication function. Finite element simulations involve sparse matrices by nature, and they are typically large, involving at least thousands of unknowns. The sparse matrix format allows this type of problem to be solved faster and with less memory than an equivalent full matrix format. This motivated the need for a sparse gpuArray format.

Several research institutions have developed gpuArray sparse formats for MATLAB. In late 2013, researchers from the Lawrence Berkeley National Laboratory released a set of code for MATLAB users for the gpuArray sparse class, called gcsparse, using the CUSP library [46]. This code defines the class gcsparse. The sparse gpuArray formats available are COO and CSR. Overloaded functions for this class are defined for transposition, sparse matrix multiplication (mtimes), real, complex, find, size, type, ptr2row, and row2ptr. The sparse matrix multiplication function uses a MEX file created for the mexFunction containing CUDA code.   This CUDA code uses the input arguments consisting of the sparse gpuArray matrix and vector (which can be sparse or full gpuArray). Based on the specified sparse matrix storage format (COO or CSR), CUDA pointers to the matrix and vector are created. The CUSP "multiply" function is used to implement the sparse GPU matrix-vector multiplication. The mexFunction output is the result of the multiplication on the GPU. The MATLAB output of the MEX file is the gpuArray result.

CHAPTER 4
SIMULATION OF THE BENCHMARK PROBLEM

4.1 Problem Description

The benchmark problem used to develop and test the finite element simulation programs is the TEAM 10 benchmark problem [47]. It consists of steel plates around a coil as an example nonlinear transient eddy current problem. The nonlinear initial magnetization B-H curve describing the steel magnetic properties is shown in Figure 4.1. The dimensions of the problem are shown in Figure 4.2. It is a three-dimensional problem. For the purpose of this set of simulations, the problem is reduced to two dimensions by simulating the cross section shown in Figure 4.2a with current excitation in the coils simplified by assuming infinite length into and out of the page. The conductivity of the steel is given as $7.505 \cdot 10^6$ S/m. The excitation current is

$$I_0 = 5.64\left(1 - e^{-t/0.05}\right) \text{ A} \tag{4.1}$$

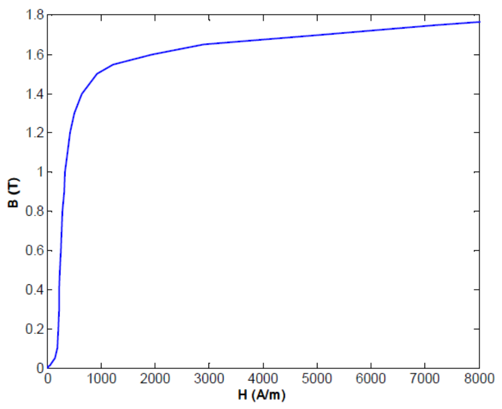

Figure 4.1 Normal magnetization curve of steel

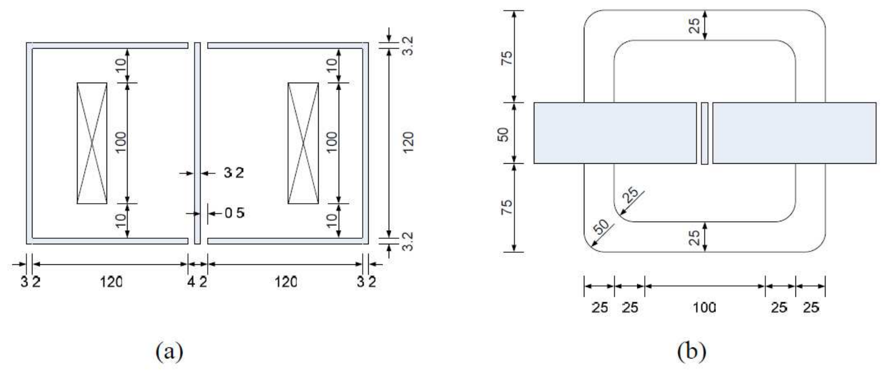

Figure 4.2 Geometry of TEAM problem 10 (dimensions in millimeters):
(a) side view, (b) top view

For use to evaluate the accuracy of finite element simulations, three search coils were positioned on the steel plates to measure the average flux densities and eddy current densities on the surface of the steel plates. Reduced to two dimensions, the search coils are positioned at the points shown in Table 4.1. Figure 4.3 shows the measured magnetic flux densities at these search coil positions and eddy current densities on the steel plate surface at these positions.

Table 4.1 Benchmark Problem Measured Positions

Search Coil Number	*x (mm)*	*y (mm)*
1	0-1.6	0
2	41.8	60-63.2
3	122.1-125.3	0

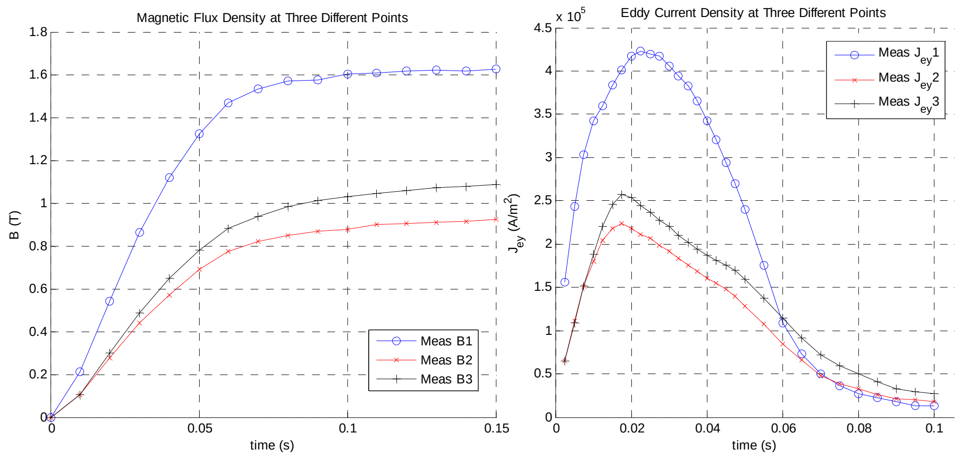

Figure 4.3 TEAM 10 benchmark problem magnetic flux density and eddy current density measured at three search coils

4.2 GPU Parallel Processing Methods

The hybrid GPU/CPU time-domain finite element program was developed to incorporate GPU computation for the suitable FEA program components based on the CPU MATLAB linear and nonlinear program implementation discussed in section 2.7 Implementation. For each type of program – first-order linear, second-order linear, first-order nonlinear, and second-order nonlinear – a hybrid GPU/CPU program was developed. The GPU parallel processing methods were the same for each type of program.

For each program, the matrix assembly was computed on the CPU using MATLAB's sparse matrix storage and sparse matrix functions. Once the matrices are assembled, they are converted to the sparse gpuArray format using the gcsparse class. This requires a conversion from the CPU double format to the GPU single format. The CSR sparse matrix storage format is utilized. The vectors used for computation including the magnetic vector potential solution are stored as gpuArray vectors.

The gcsparse class is used in order to explore the GPU speed-up of the sparse matrix-vector multiplication CUSP function "multiply." Sparse matrix-vector multiplication using the CSR sparse matrix storage format yielded accurate results, but when the COO storage format was used, the results were inaccurate or nonsensical. As discussed in section 3.2.2.2.3 Sparse gpuArray format, the gcsparse class overloaded multiplication function is defined using a MEX file that links the MATLAB gpuArray inputs with the compiled CUDA source file mexFunction. The MEX function uses the mxGPUArray type from the MATLAB mxGPU API to create pointers to the MEX function inputs, perform calculations, and return outputs to MATLAB. The sparse matrix multiplication source file for the CSR storage format creates pointers to the appropriate CSR-format input matrix, allocates memory for the vector output, and calls the CUSP function multiply.

This MEX file is created once using the mex function to compile the CUDA source file. This compilation time is not included in the GPU program computation time and only takes a few seconds.

Using the sparse gpuArray matrix and gpuArray vector formats, the GPU sparse matrix-vector multiplication is used to calculate the magnetic flux density for the linear and nonlinear program, and $\frac{\partial B^2}{\partial A}$ and SA terms for $[G]_k^{t+\Delta t}$ for the nonlinear program. The same syntax using the "*" operator for matrix-vector multiplication is used. With the operator overloaded for the gcsparse and gpuArray formats, MATLAB will use the gcsparse class multiplication function. This allows the hybrid GPU/CPU program to be readily converted from the CPU program once the sparse gpuArray and overloaded functions with MEX files are created.

The preconditioner is computed using the MATLAB function on the CPU given the CPU sparse matrix inputs. As described in section 2.7 Implementation, the incomplete Cholesky factorization is used for the linear simulation using the MATLAB "ichol" function, and the incomplete LU factorization is used for the nonlinear simulation using the MATLAB "ilu" function. These preconditioners are not defined in the CUSP library. The available preconditioners in the CUSP library are variations on the Bridson outer product formulation (approximate inverse), diagonal, and smoothed aggregation. In [35], the author investigates the CPU and GPU computation time for the incomplete-LU factorization preconditioner formation using different fill-ins from the preconditioner functions available in the cuSPARSE library from the NVIDIA CUDA toolkit. The speed-up was highly dependent on the sparsity of the matrix, and the matrix sizes were much larger, 3-17 million nonzero elements, than the matrix size for this application, several thousand elements. In this application, only the CUSP library functions were investigated. Using the preconditioner algorithm, a MATLAB script could be written using the gpuArray matrix format. However, directly using the algorithm with the gpuArray matrix will not yield speed-up since the direct algorithm steps through each element in the matrix sequentially. A specialized CUDA program utilizing multithreading is needed in order to utilize the GPUs for parallel processing. With the desire for direct CPU and GPU computation time comparisons for the same functions and implementation, since the CUSP library did not have the same preconditioners defined as used for the MATLAB CPU implementation, the preconditioner formation was left on the CPU.

The biconjugate gradients stabilized sparse iterative solver computation time was explored using the CPU and GPU. Using the CPU, the MATLAB "bicgstab" sparse iterative solver was used. Additionally, two equivalent biconjugate gradient functions following the known algorithm, with or without a preconditioner, were written [11]. These function can receive inputs that are either CPU double sparse matrices/vectors or sparse or full gpuArray matrices/vectors. Note that the bicgstab algorithm without a preconditioner requires two sparse matrix-vector multiplications per iteration, and the bicgstab algorithm with a preconditioner requires two sparse matrix-vector multiplications and two sparse matrix-vector solutions per iteration. For the CPU preconditioned biconjugate gradient algorithm function, the matrix-vector solution is calculated using the MATLAB "mldivide" function for sparse matrices.

For GPU biconjugate gradients iterative solver computation, several methods were explored. The gpuArray matrix and vectors were used with the implemented algorithms with and without preconditioners. The implementation of the bicgstab function without the preconditioner is the same for the gpuArray format as for the CPU double sparse format. However, for the implementation of the bicgstab function with the preconditioner, the same implementation for the

GPU cannot be used as for the CPU since the MATLAB “mldivide” function is only available for full gpuArray formats. Instead, to implement this algorithm, the inverse of the preconditioner is computed on the CPU using the MATLAB “inv” function. Then, in the bicgstab implemented function with preconditioner for gpuArray and gcsparse, the preconditioner inverse is used to require four sparse matrix-vector multiplications per iteration instead of two sparse matrix-vector multiplications and two sparse matrix-vector solutions. The overhead required to compute the preconditioner inverse is acceptable for small problems but not for larger problems such as the fine mesh used for this benchmark problem. As a result, the bicgstab implemented function with preconditioner for the gpuArray is not usable.

Another method for the sparse iterative solver explored is the CUSP “bicgstab” function without a preconditioner through the MEX file. A CUDA mexFunction given MATLAB CPU sparse input matrix and vectors to solve, allocates memory and transfers the matrix and vector to the GPU in COO format, allocates space on the GPU for the solution, calls the Krylov “bicgstab” function, and outputs the solution. This mexFunction was compiled as previously described to create the mexFunction. This function with the CUSP bicgstab solver computed accurate results for small problems, but for larger matrices applied to the benchmark problem, the solver did not converge and output a diverging solution for the same problem that did converge using the CPU MATLAB bicgstab function. As a result, this mexFunction was not usable for the finite element simulations.

For several problem sizes, Table 4.2 shows a comparison of multiple CPU and GPU-implemented un-preconditioned solver computation times. Speed-up is computed for the fastest CPU solution over the fastest GPU solution. From this sample of problems analyzed, the density of the matrix affects the speed-up achieved by the hybrid CPU/GPU program over the CPU program. Assessing the mldivide function using CPU sparse format and full gpuArray format, the gpuArray format achieves speed-up over the CPU for random sparse matrices. However, for matrices with similar sparsity as for the finite element simulations, speed-up is not achieved. Comparing the CPU and GPU biconjugate gradient iterative solver implementations, speed-up is only achieved for the dense random matrix, not for the finite element sparse matrix. Additional CPU and GPU iterative solver computation times for the specific problems are discussed in section 4.3 Simulation Results.

Table 4.2 CPU and GPU Comparison Times for Multiple Problem Sizes for Different Solvers Without the Preconditioner

	CPU or GPU	*CPU*	*GPU*	*GPU*	*Speed-up*	*CPU*	*CPU*	*GPU*	*GPU*	*Speed-up*
	Sparse or Full Matrix	Sparse	Full	Full		Sparse	Sparse	Sparse	Sparse	
	Data Structure	MATLAB CPU sparse	gpuArray	gpuArray		MATLAB CPU sparse	MATLAB CPU sparse	CUSP COO (original MATLAB CPU sparse) - includes transfer to COO format	gcsparse	
	Solver	\	\	\		MATLAB bicgstab	m file bicgstab	CUSP bicgstab	m file bicgstab	
	Single or Double	Double	Single	Double		Double	Double	Single	Single	
Solution Time for Problem (s)	**Wilk 21x21 matrix**	0.00002	0.10132	0.00051	0.04630	0.00153	0.00130	0.02783	0.05980	0.04676
	Random 100x100 matrix, symmetric, diagonal	0.1485	0.2868	0.0312	4.7661	0.0082	0.0050	6.8788	0.3328	0.0151
	Random 1000x1000 matrix, symmetric, diagonal	0.1092	0.1150	0.0209	5.2202	0.0125	0.0261	12.5315	0.1141	0.1094
	Random 5000x5000 matrix, symmetric, diagonal	5.2423	0.4186	0.7420	12.5241	0.0694	0.1589	28.3397	0.0539	1.2876
	Random 5000x5000 matrix, symmetric, diagonal, sparse with density 9.95533e-4	0.0029	0.2837	0.6708	0.0101	0.0052	0.0099	11.9676	0.0482	0.1085
	Random 6927x6927 matrix, symmetric, diagonal, sparse with density 9.95533e-4	0.0053	0.6371	1.5931	0.0083	0.0078	0.0139	0.0000	0.0483	0.1618
	Linear problem at t = 50 ms, 6927x6927 matrix, 7219 nnz	0.0134	0.9051	1.5910	0.0148	0.3697	0.3559	0.0000	1.8540	0.1920
	Nonlinear problem at t = 5 ms, first order elements fine mesh	0.0413	3.6364	0.0000	0.0113	0.2439	0.6854	0.0000	4.0792	0.0598

4.3 Simulation Results

Following the finite element derivations for first-order and second-order linear and nonlinear simulations, each of these simulations was developed for the TEAM 10 benchmark problem geometry and material properties. The simulations were developed using MATLAB scripts. On the CPU, the MATLAB sparse vector and matrix storage and operations were used. On the GPU, the gpuArray, sparse gpuArray, and MEX files linked to CUDA file were used. Computation time for the CPU and hybrid CPU/GPU simulations is determined using the “tic” and “toc” MATLAB functions. All of the simulations for this thesis were conducted on the CPU using an Intel Core i5-2400 CPU with 4 gigabytes of random-access memory. The Windows 7 64-bit operating system was used. The GPU for personal computing used for these simulations is the NVIDIA GeForce GTX 780 (Kepler architecture) GPU with 3 gigabytes of memory and compute capability 3.5. The GTX 780 has 2304 CUDA cores. Final MATLAB simulation implementations were developed for MATLAB R2014a.

For each type of simulation, a coarse and fine mesh of the geometry was used to assess scalability of the GPU simulation. Table 4.3 describes the number of elements and nodes for each type of simulation. Figure 4.4 illustrates the coarse mesh, and Figure 4.5 illustrates the fine mesh. The blue elements represent the coils with impressed current density, magenta elements represent the magnetic steel, and white elements represent air. The elements and nodes that are colored differently show the tracked nodes and elements in the simulations. The magnetic vector potential and magnetic flux density solution is calculated for the entire domain for each iteration or time step, but only specified nodes and element solutions are saved for the entire transient simulation.

Table 4.3 Benchmark Problem Mesh Descriptions

Magnetic Material Model	Element Order	Mesh	*Total Domain* Number of Nonzero Elements in Matrix	*Total Domain* Number of Elements	*Total Domain* Number of Nodes	*Nonlinear Region* Number of Elements	*Nonlinear Region* Number of Nodes
Linear	First	Fine	47769	14144	7219	0	0
	Second	Coarse	62973	3536	7219	0	0
	Second	Fine	257873	14144	28581	0	0
Non-Linear	First	Coarse	11444	3536	1842	932	725
	First	Fine	47769	14144	7219	3728	2379
	Second	Fine	257873	14144	28581	3728	8483

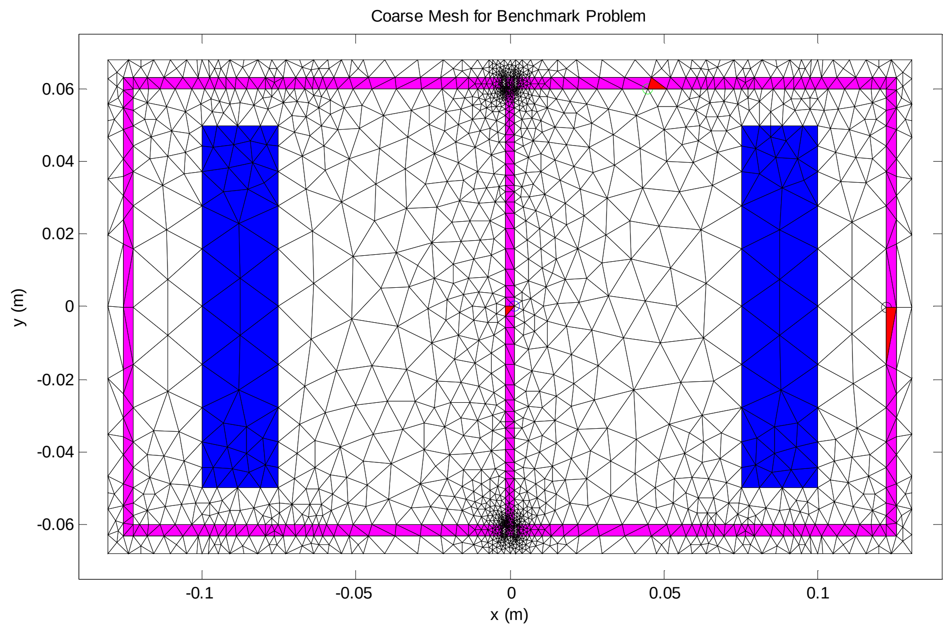

Figure 4.4 Coarse mesh for benchmark problem

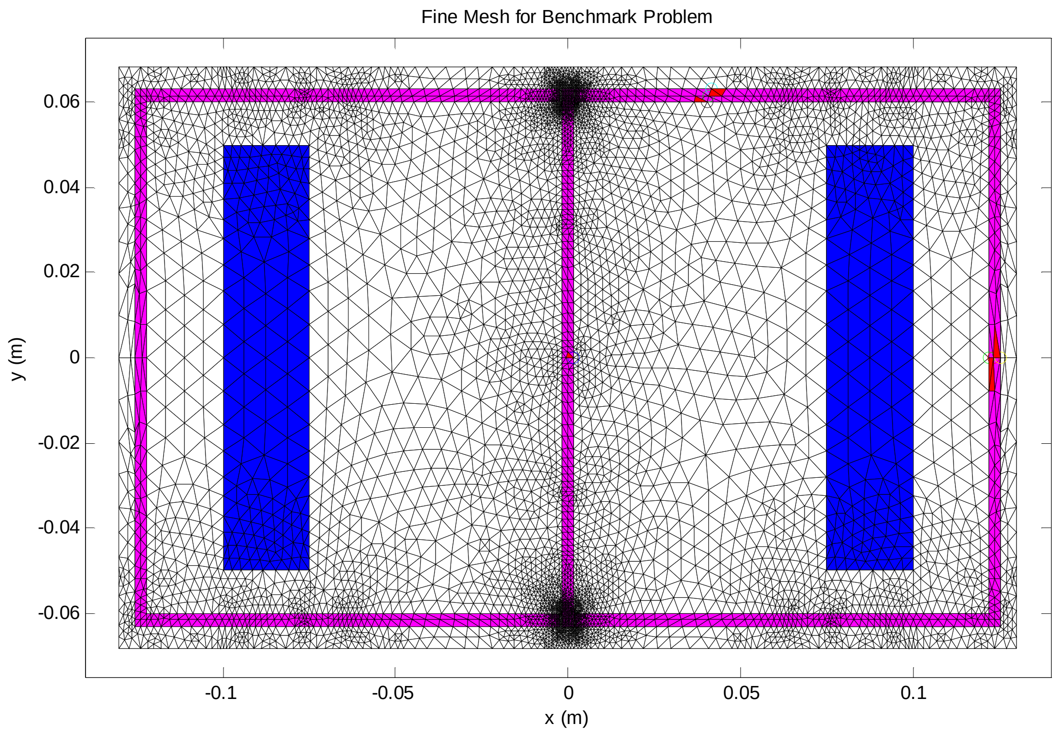

Figure 4.5 Fine mesh for benchmark problem

4.3.1 Linear magnetic material simulation results

4.3.1.1 First-order elements with linear magnetic material

The first-order element, linear magnetic material solutions for the benchmark problem are shown in Figure 4.6 for magnetic flux density and Figure 4.7 for eddy current density for the fine mesh. The computed solutions at the nodes nearest to the search coils are used to compare to the measured solutions, and those coordinates are shown in Table 4.4 The steel permeability is represented linearly with relative permeability $\mu_r = 1000$. The CPU simulation uses the biconjugate gradient algorithm implemented function with preconditioner using the MATLAB double sparse format. The GPU simulation uses the same iterative solver function with the sparse gpuArray single format.

Table 4.4 Tracked Solution Points for First-Order, Linear Program for Benchmark Problem

	Measured Points		*Simulated Points*	
Search Coil Number	x (mm)	y (mm)	x (mm)	y (mm)
1	0-1.6	0	1.6	0
2	41.8	60-63.2	41	61.6
3	122.1-125.3	0	123.2	0

To show CPU and GPU program simulation time, Figure 4.8 shows the computation time for the major components of the linear program for each time step. The major components measured for each time step are the right-hand side vector calculation from equation (2.44), time to solve for the magnetic vector potential using the sparse iterative solver, post-processing for magnetic flux density, and post-processing for eddy current density. For the magnetic flux density and iterative solver component computation times per time step, Figure 4.9 shows the CPU and GPU computation times and speed-up. Note that the GPU computation times presented throughout this thesis include the overhead to transfer data to the GPU from the CPU, and from the GPU back to the CPU. The GPU computation time for the magnetic flux density results in approximately 4 times speed-up, but no speed-up – approximately 0.3 – for the sparse iterative solver with preconditioner.

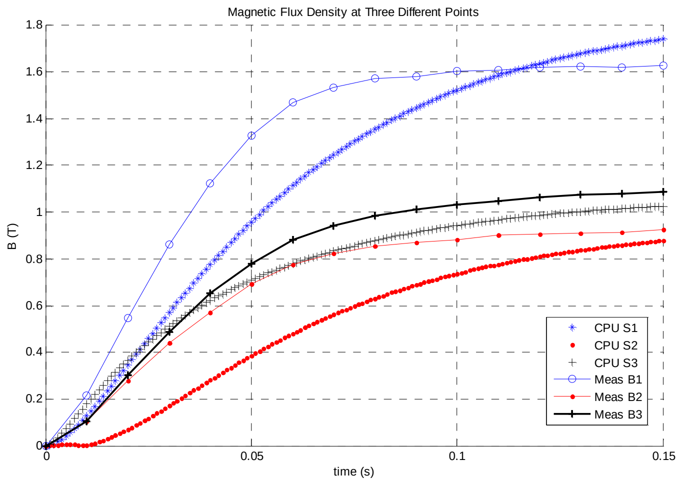

Figure 4.6 First-order element, linear material, magnetic flux density solution for fine mesh, compared to TEAM problem measured results at three points

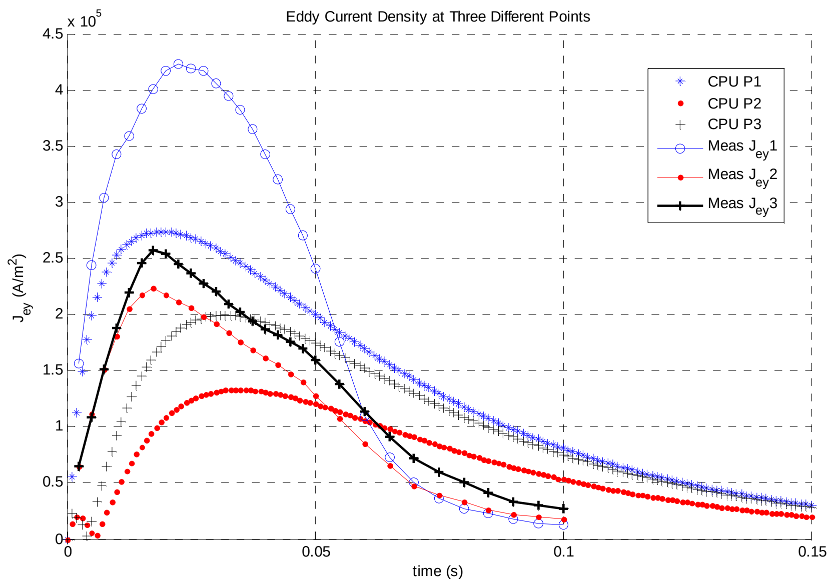

Figure 4.7 First-order element, linear material, eddy current density solution for fine mesh, compared to TEAM problem measured results at three points

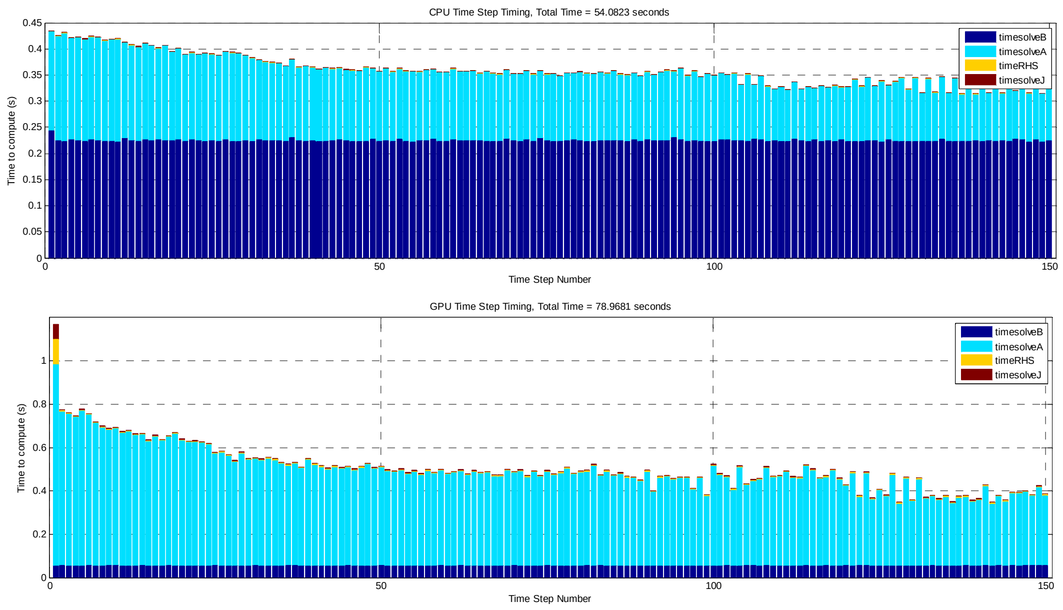

Figure 4.8 First-order element, linear material, CPU and GPU computation time for each time step

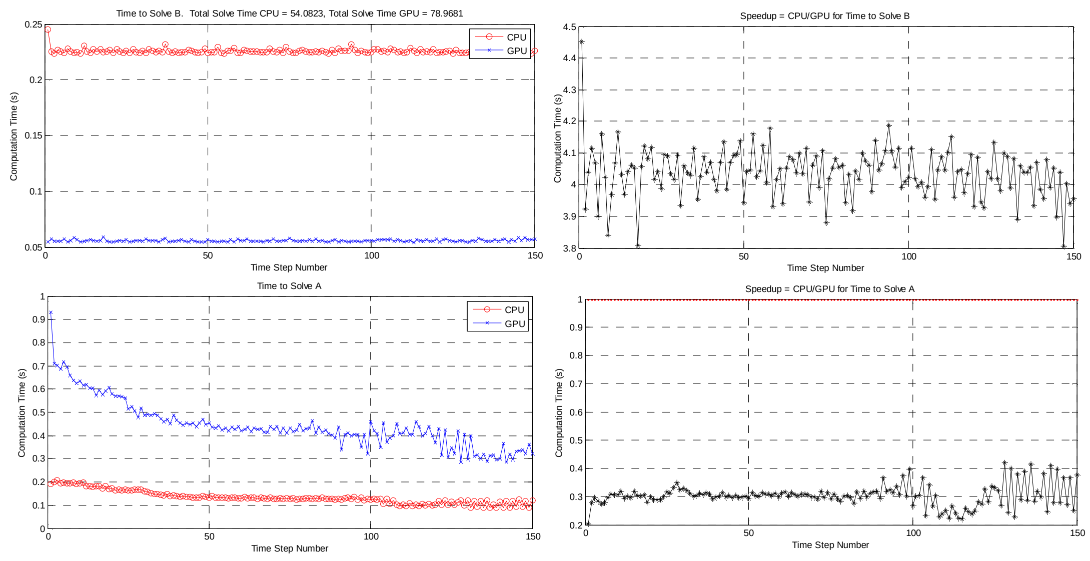

Figure 4.9 First-order element, linear material, CPU and GPU computation time comparison for magnetic flux density and magnetic vector potential

Table 4.5. CPU and GPU Simulation Computation Time Comparison for First-Order Elements, Linear Magnetic Material, Fine Mesh. Iterative solver is preconditioned.

		Total for Simulation		
Simulation Time(s)/Speed-up	**Preconditioner Formation on CPU**	**Iterative Solver**	**Magnetic Flux Density**	**Total**
CPU Time (s)	0.004	20.075	33.858	54.082
GPU Time (s)	0.746	66.733	8.388	78.968
Speed-up	**N/A**	**0.301**	**4.036**	**0.685**
Hybrid CPU/GPU Time (s)	0.004	18.417	8.454	29.414
Speed-up	**N/A**	**N/A**	**4.005**	**1.839**

Table 4.5 summarizes the CPU and GPU computation time for the first-order, linear element simulation for the fine mesh using the preconditioned iterative solver. For the CPU simulation, the total magnetic flux density computation time was 33.86 seconds. Comparatively, the total magnetic flux density computation for the GPU simulation was only 8.39 seconds due to sparse gpuArray matrix-vector multiplication. This yields a total speed-up for the magnetic flux

density calculation of 4.04. However, the sparse gpuArray format did not yield a speed-up for the sparse iterative solver. The total CPU sparse iterative solver calculation time was 20.075 seconds, while the total GPU sparse iterative solver calculation time was 66.73 seconds. As a result, the total computation time for the GPU simulation did not speed up the simulation compared to the CPU simulation. For a hybrid CPU/GPU simulation that uses the sparse gpuArray format for magnetic flux density calculation and the CPU sparse format for the CPU iterative solver calculation, the simulation time is reduced by the GPU speed-up for the magnetic flux density calculation. This saves approximately 25.4 seconds of computation time. With minimal GPU to CPU transfer overhead, the resulting overall CPU/(hybrid CPU-GPU) speed-up is 1.84.

4.3.1.2 Second-order elements with linear magnetic material

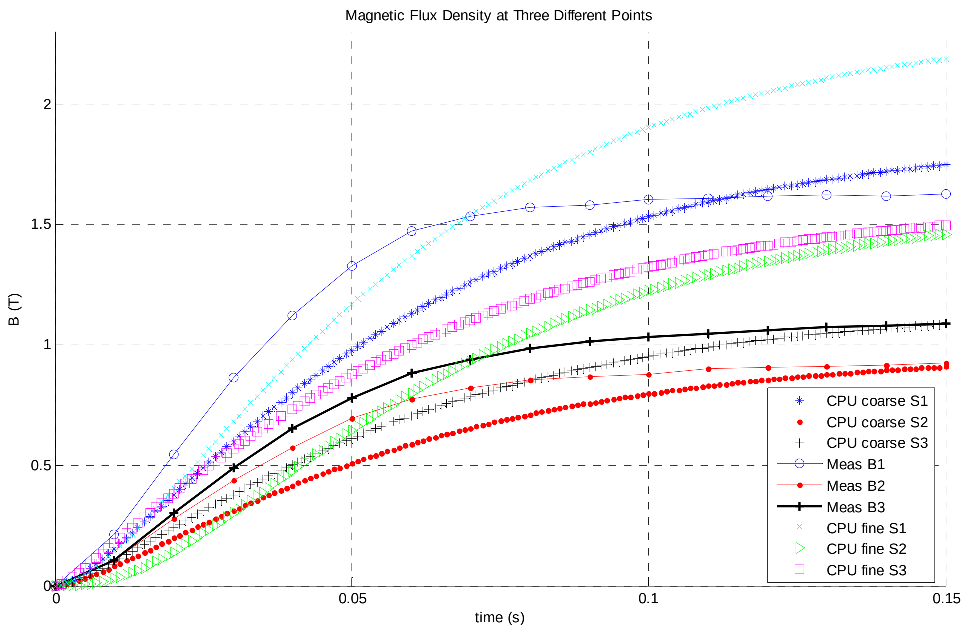

Figure 4.10 Second-order element, linear material, magnetic flux density solution for coarse and fine meshes, compared to TEAM problem measured results at three points

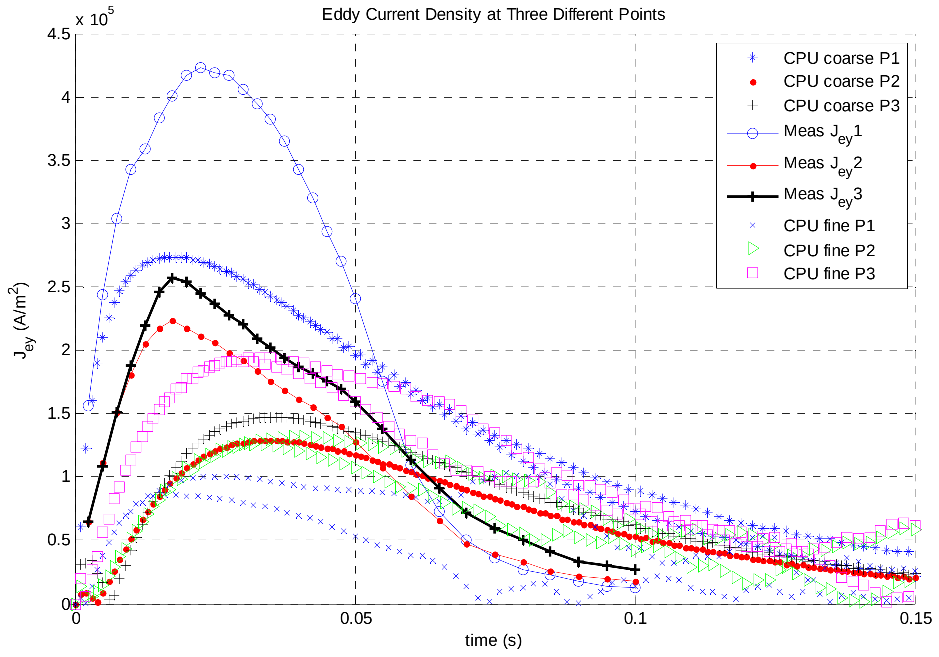

Figure 4.11 Second-order element, linear material, eddy current density solution for coarse and fine meshes, compared to TEAM problem measured results at three points

The coarse and fine mesh computed solutions near the measured points for the second-order, linear element simulation are shown in Figure 4.10 for magnetic flux density and Figure 4.11 for eddy current density. The solutions shown for the coarse and fine meshes are for the tracked points shown in Table 4.6.

Table 4.6 Tracked Solution Points for Second-Order, Linear Program for Benchmark Problem

	Measured Points		*Coarse Mesh Simulated Points*		*Fine Mesh Simulated Points*	
Search Coil Number	x (mm)	y (mm)	x (mm)	y (mm)	x (mm)	y (mm)
1	0-1.6	0	1.6	0	0.55	0
2	41.8	60-63.2	41	61.6	41	61.6
3	122.1-125.3	0	123.7	0	123.2	0

Table 4.7 CPU and GPU Simulation Computation Time Comparison for Second-Order Elements, Linear Magnetic Material

				Total for Simulation			
Mesh	**Solver With or Without Preconditioner**	**Simulation Time(s)/Speed-up**	**Preconditioner Formation on CPU**	**Iterative Solver**	**Magnetic Flux Density**	**Total**	**Total for Hybrid CPU/GPU**
Coarse Mesh	Without preconditioner	CPU Time (s)	0	50.041	41.271	91.567	91.567
		GPU Time (s)	0	266.572	27.597	295.940	77.893
		Speed-up	N/A	**0.188**	**1.495**	**0.309**	**1.176**
	With preconditioner	CPU Time (s)	0.008018164	24.213	40.944	65.371	65.371
		GPU Time (s)	1.115737855	73.364	29.688	117.886	54.114
		Speed-up	N/A	**0.330**	**1.379**	**0.555**	**1.208**
Fine Mesh	Without preconditioner	CPU Time (s)	0	173.999	296.619	471.564	471.564
		GPU Time (s)	0	274.234	25.267	301.561	200.212
		Speed-up	N/A	**0.634**	**11.739**	**1.564**	**2.355**
	With preconditioner	CPU Time (s)	0.005682121	261.100	298.550	560.593	560.593
		GPU Time (s)	0.120006674	291.103	44.060	338.000	306.102
		Speed-up	N/A	**0.897**	**6.776**	**1.659**	**1.831**

The computation time for each major component and total simulation are shown in Table 4.7. It is important to note that in the linear simulation case, the preconditioner is only formed once. As a result, the total simulation time is not as sensitive to the time to form the preconditioner, but rather to the iterative solver computation time. For the coarse and fine mesh, the gpuArray sparse format used with the iterative solver with and without the preconditioner did not achieve speed-up. However, for the coarse mesh, approximately 1.4 times speed-up was achieved for the magnetic flux density calculation. For the fine mesh, approximately 6-11 times speed-up was achieved for the magnetic flux density calculation. Comparing the CPU iterative solver computation time with and without the preconditioner, the coarse mesh solution using the preconditioner was computed approximately twice as fast as compared to the solution without the preconditioner. However, for the preconditioner used, the fine mesh solution with the preconditioner was computed approximately 1.5 times slower than without the preconditioner. In this case, using a different preconditioner may result in faster computation of the next magnetic vector potential time step solution. Comparing the total CPU and GPU simulation times for the GPU solution using the sparse gpuArray for the iterative solver, speed-up was only achieved for the fine mesh. For the hybrid CPU/GPU simulation where the sparse iterative solver is computed on the CPU and the magnetic flux density is computed on the GPU, a total speed-up of approximately 1.2 is achieved for the coarse mesh, and approximately 1.8-2.3 for the fine mesh. The speed-up is limited in this case to the percentage of the simulation where GPUs can be utilized to compute the solution faster than the CPU. In this case, this is for the magnetic flux density, which accounts for approximately 45-63% of the CPU total simulation time.

4.3.2 Nonlinear magnetic material simulation results

Given the magnetic steel material properties for the benchmark problem shown in Figure 4.1, the magnetic reluctivity vs. magnetic flux density squared and $\frac{\partial \nu}{\partial B^2}$ vs. magnetic flux density squared were computed. These curves are represented using piecewise-linear representation in MATLAB. The curves used to simulate the nonlinear magnetic steel properties are shown in Figure 4.12. The discontinuities in the representation of the magnetic reluctivity vs. magnetic flux density squared result in discontinuities in the derivative representation.

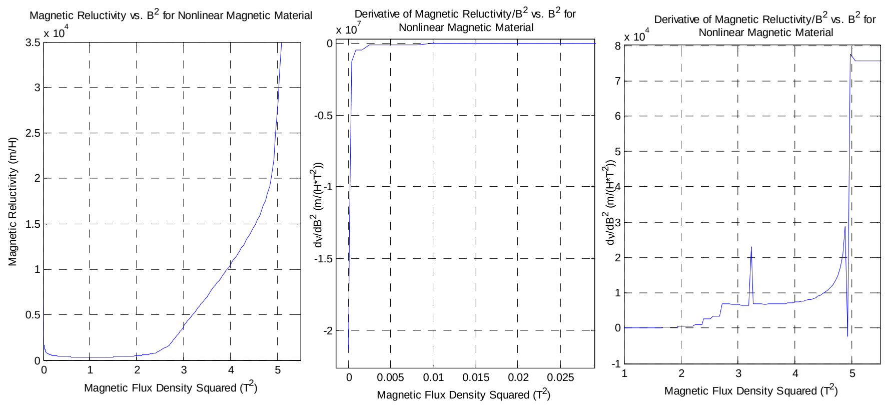

Figure 4.12 Nonlinear magnetic material representation for benchmark problem simulation

4.3.2.1 First-order elements with nonlinear magnetic material

Solutions for the computed magnetic vector potential, magnetic flux density, and eddy current density were tracked at several elements and nodes. The first measured solution is tracked at an outer node between the steel and air with an element in the middle of the steel. The second and third measured solutions are each tracked at inner, middle, and outer nodes and elements. The computed solutions at the middle nodes and elements match the measured solutions more closely than those on the inner or outer elements or nodes. The inner computed solutions were calculated at higher magnetic flux densities and eddy currents than measured, and the outer computed solutions were at lower values than measured. The following solutions shown are for the middle elements and nodes close to the measured solutions described by the coordinates in Table 4.8

Table 4.8 Tracked Solution Points for First-Order, Non-linear Program for Benchmark Problem

	Measured Points		*Coarse Mesh Simulated Points*		*Fine Mesh Simulated Points*	
Search Coil Number	x (mm)	y (mm)	x (mm)	y (mm)	x (mm)	y (mm)
1	0-1.6	0	1.6	0	1.6	0
2	41.8	60-63.2	44.6	60	41	61.6
3	122.1-125.3	0	122.1	0	123.2	0

The computed transient solutions at the designated points for the coarse and fine mesh are shown in Figure 4.13 for the magnetic flux density, Figure 4.14 for the eddy current density, and Figure 4.15 for CPU and GPU calculations of eddy current density. The points tracked for the coarse mesh more closely track the measured magnetic flux density solution than the fine mesh points. Both mesh solutions show the nonlinear magnetic material impact on the solution compared to the linear simulations. The fine mesh solution for the first eddy current density point near the origin closely tracks the measured solution, but the other calculated solutions do not match well. Again, the nonlinear representation of the magnetic material is evident. Figure 4.16 shows the comparison of the CPU and GPU calculated magnetic vector potential, magnetic flux density, and eddy current density. The magnetic vector potential and magnetic flux density calculations match closely, but there are some differences in the first point eddy current density later in the transient solution.

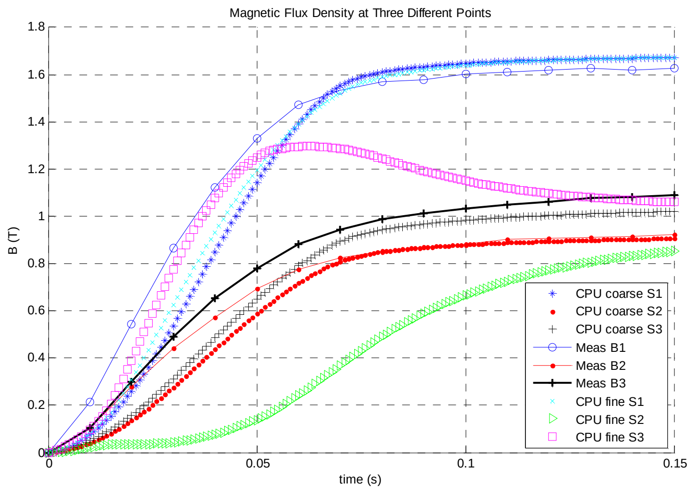

Figure 4.13 First-order element, nonlinear material, magnetic flux density solution for coarse and fine mesh, compared to TEAM problem measured results at three points

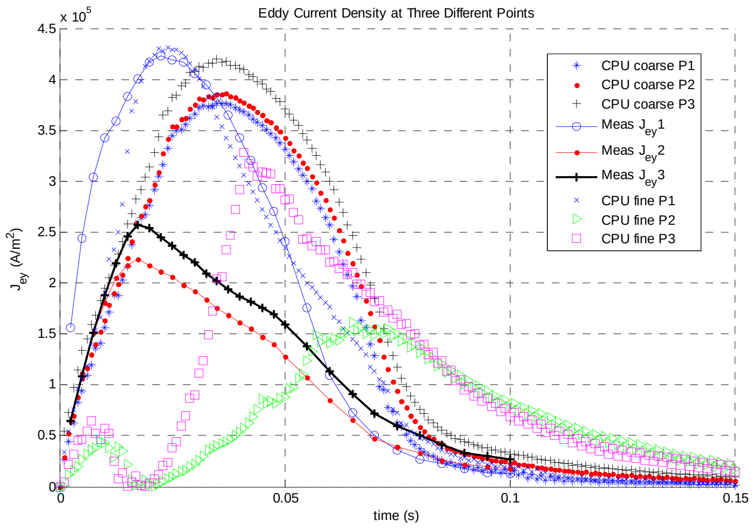

Figure 4.14 First-order element, nonlinear material, eddy current density solution magnitude for coarse and fine mesh, compared to TEAM problem measured results at three points

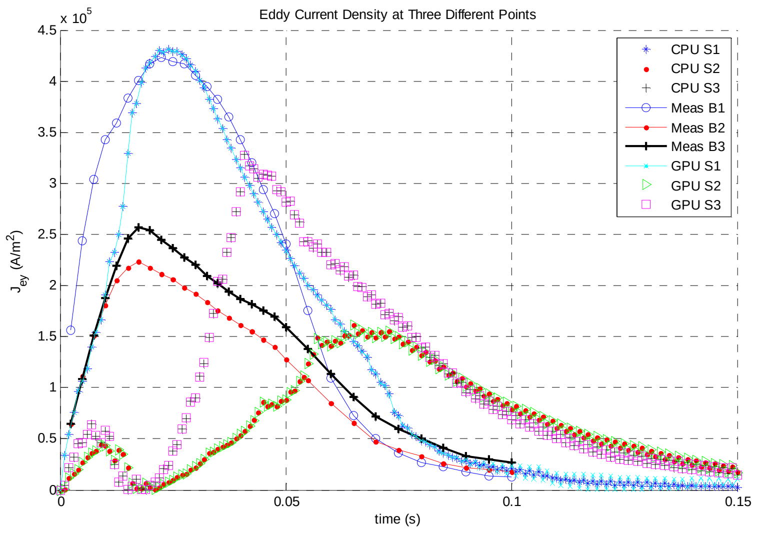

Figure 4.15 First-order element, nonlinear material, eddy current density solution magnitude for fine mesh, GPU and CPU solutions, compared to TEAM problem measured results at three points

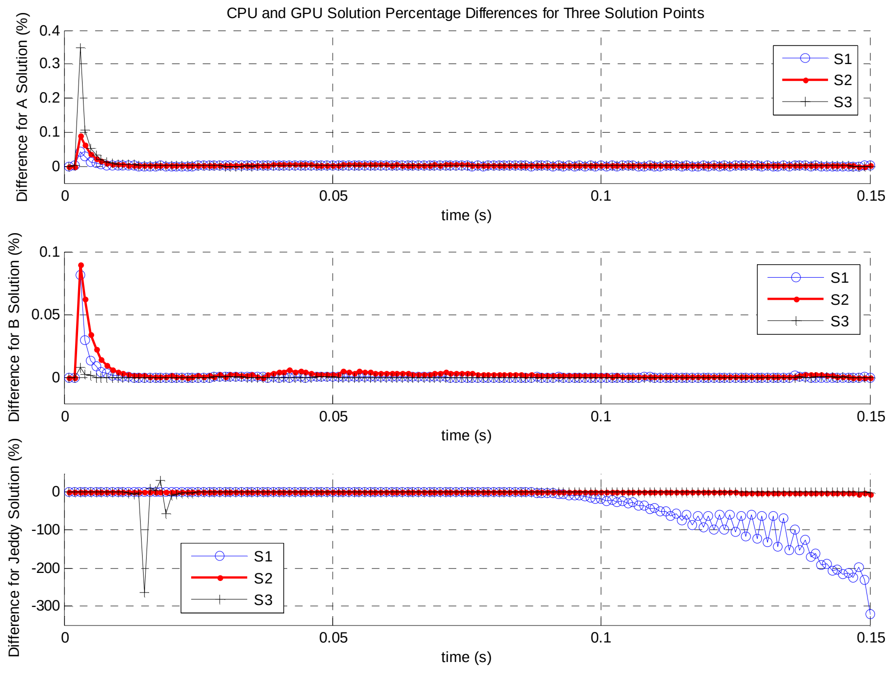

Figure 4.16 First-order element eddy current solution for fine mesh, GPU and CPU solutions, percentage difference for magnetic vector potential, magnetic flux density, and eddy current density computed solutions

In the following subsections, results are shown for CPU and GPU simulation times for the coarse and fine mesh complete solutions for each time step broken down by section of the time step solution. These results use the MATLAB (CPU, sparse matrix) ILU preconditioner function with the Crout version of ILU, drop tolerance of 1e-5, and row-sum modified incomplete LU factorization. Due to results also shown for the CPU and GPU iterative solver, these results use the fastest implementation with the CPU and MATLAB's bicgstab solver with the ILU preconditioner.

4.3.2.1.1 Iterative solver numerical experiments

The following numerical experiments were conducted for the first-order elements, nonlinear magnetic material simulation with the fine mesh. Experiments were conducted to determine the shortest computation time achievable for the iterative solver. Methods using the bicgstab algorithm on the CPU and GPU and with or without a preconditioner were explored. Figure 4.17 shows the difference in the number of iterations when the preconditioner is not used and when it is used. Accordingly, Figure 4.18 shows that the higher number of iterations results in longer total solver computation time, shown as "timesolveA." Figure 4.19 shows that even with the preconditioner formation time, shown as "timePrec," the overall solver time including the preconditioner formation time is shorter than the iterative solver time without the preconditioner.

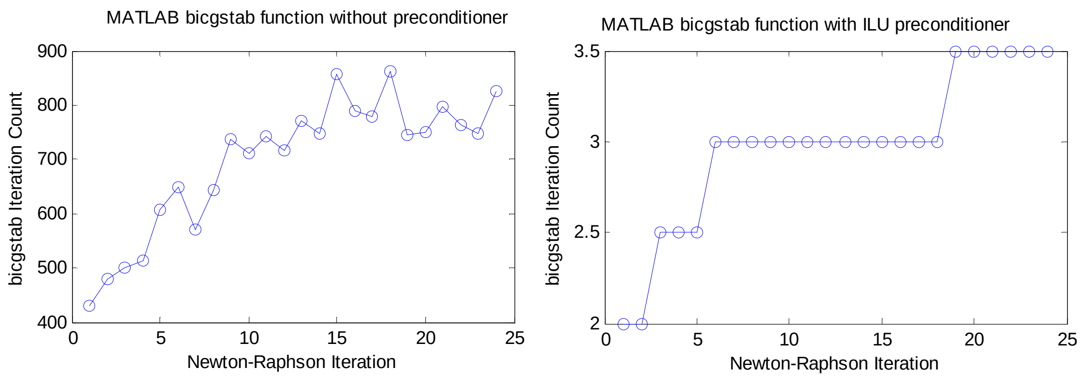

Figure 4.17 Number of bicgstab iterations without and with preconditioner to solve each Newton-Raphson iteration. Example solution for time setup = 14 ms.

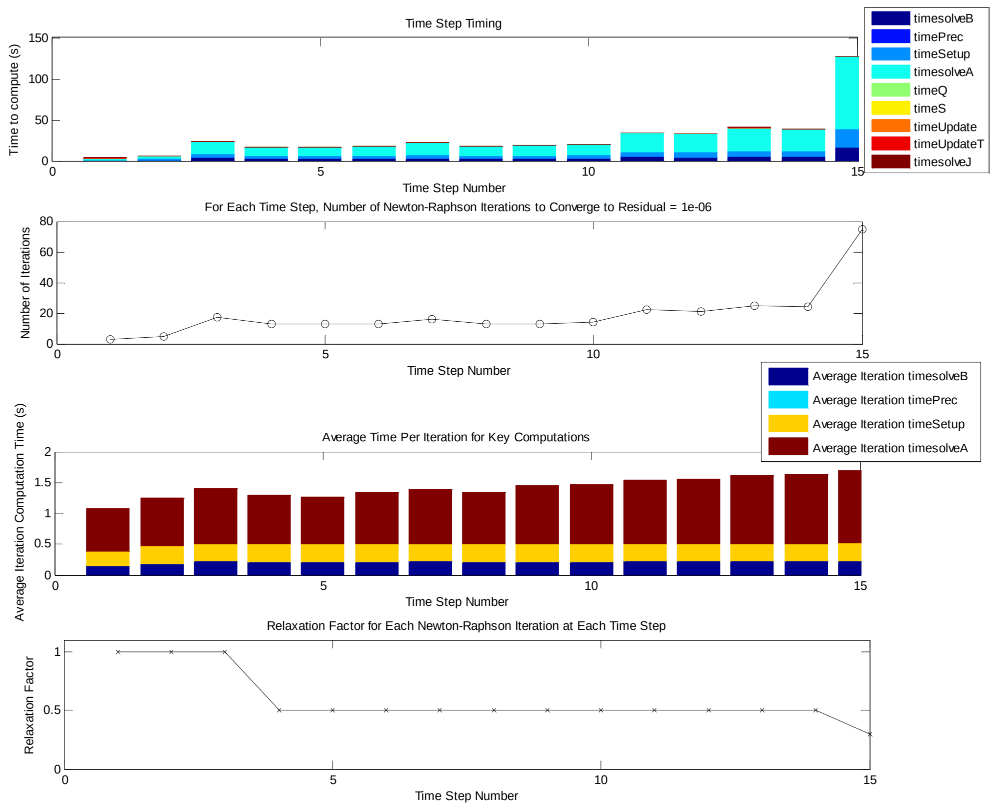

Figure 4.18 Iterative solver time for MATLAB bicgstab function without preconditioner

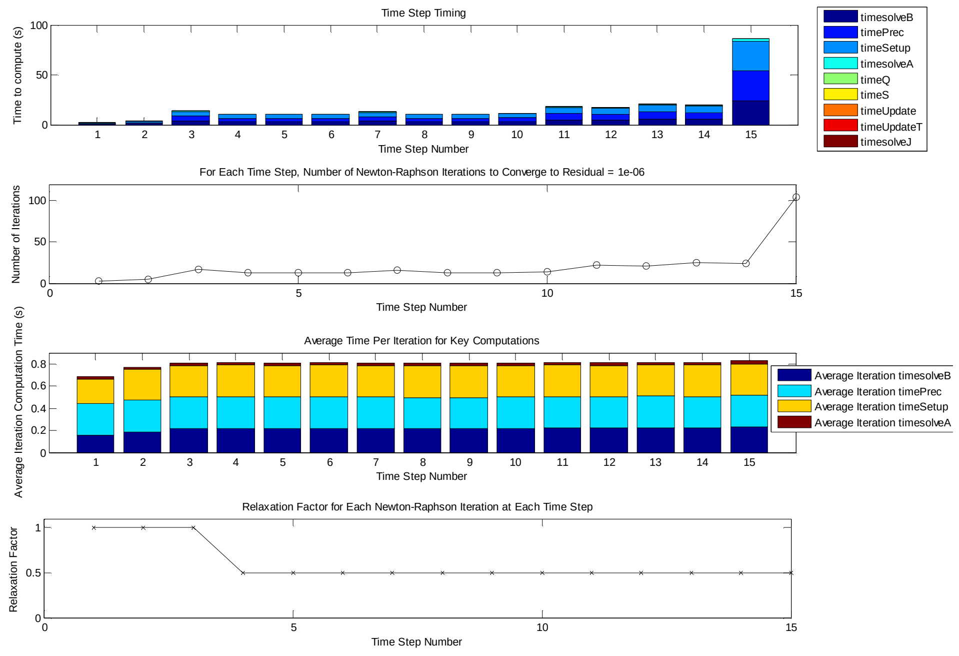

Figure 4.19 Iterative solver time for MATLAB bicgstab function with preconditioner

Table 4.9 CPU and GPU Bicgstab Iterative Solver Algorithm Comparison with and without Preconditioner

CPU or GPU	Solver	Preconditioner Used	*Average Newton-Raphson Iteration Computation Time (s)*					Iterative Solver Percentage (%)
			Magnetic Flux Density	Setup	Magnetic Vector Potential Iterative Solution	Precon-ditioner	Approximate Total	
CPU	MATLAB bicgstab	No	0.21274	0.27914	0.92945	0.00000	1.42133	65.39
CPU	bicgstab algorithm	No	0.21571	0.27969	0.83654	0.00000	1.33194	62.81
GPU	bicgstab algorithm	No	0.05041	0.13759	4.94796	0.00000	5.13596	96.34
CPU	MATLAB bicgstab	Yes	0.21184	0.27810	0.02297	0.28577	0.79868	38.66
CPU	bicgstab algorithm	Yes	0.21765	0.27738	1.56864	0.34742	2.41109	79.47

Table 4.9 summarizes timing results for the CPU and GPU bicgstab iterative solver algorithms with and without the preconditioner. The results are for time step solutions from 1 to 15 ms. Note that for the CPU bicgstab algorithm with preconditioner implemented, the two linear solutions of $\mathbf{Ax} = \mathbf{b}$ use the MATLAB mldivide function. This dominates the solution time and is much slower than the MATLAB bicgstab with preconditioner function. Also, the GPU bicgstab algorithm with preconditioner implemented requires the inverse of the preconditioner to be computed since the mldivide function is not available for sparse GPUArray types. As a result, this GPU bicgstab algorithm is extremely slow and is not included in this comparison. As previously stated, further research using developed preconditioner formation and bicgstab with preconditioner algorithms implemented using CUDA, such as in the cuSPARSE library, could be used and integrated with MATLAB to determine if GPU speed-up can be achieved for this specific problem. For the fastest implementation compared, the iterative solver for the magnetic vector potential is approximately 39% of the average Newton-Raphson iteration computation time. With further research, this component may be further reduced with GPU computing, but based on other research, this is not conclusive based on the problem size and sparsity [35], [36], [37], [38]. Based

on these results, the iterative solver method used for the hybrid CPU/GPU solutions is the CPU-based MATLAB bicgstab function with the ILU preconditioner.

4.3.2.1.2 Iteration setup time breakdown

The results in Figure 4.20 and Figure 4.21 show the CPU and hybrid CPU/GPU simulation setup computation time for the fine mesh solution.

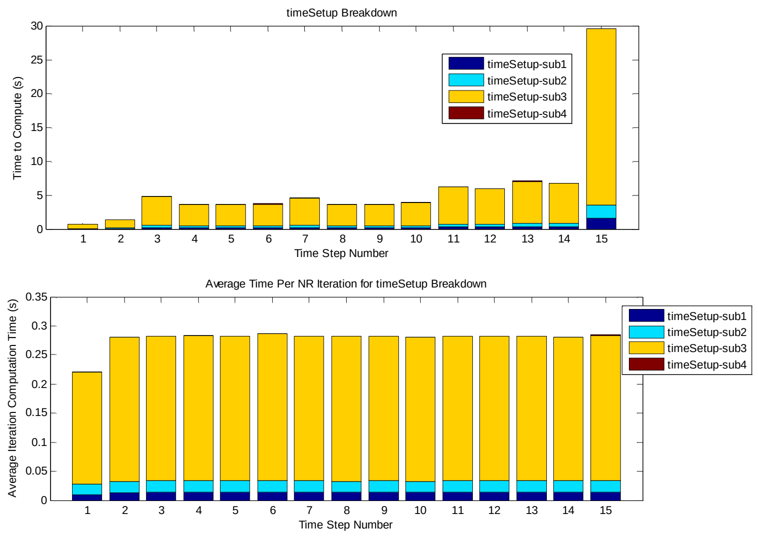

Figure 4.20 Setup time breakdown for CPU

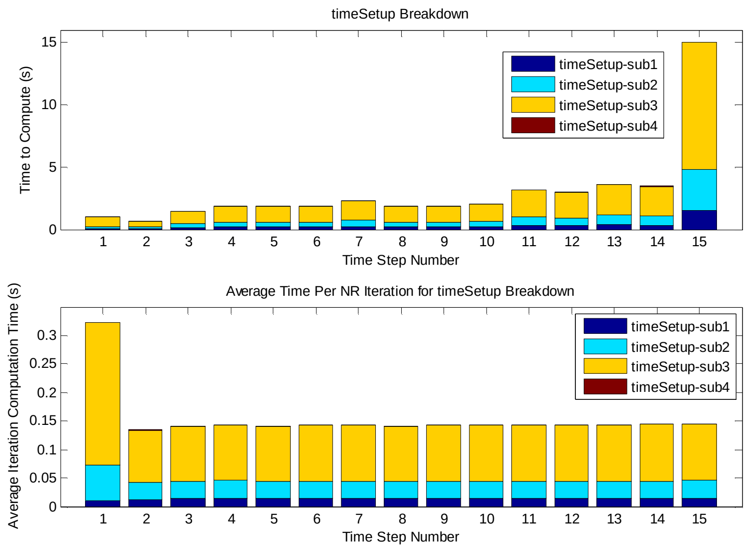

Figure 4.21 Setup time breakdown for GPU sparse

The setup computation required for each Newton-Raphson iteration is broken down into four subsections. The subsections along with the hybrid CPU/GPU simulation implementation are:

- timeSetup-sub1 = look up ν and $\frac{\partial \nu_k^{e,t+\Delta t}}{\partial \left(B_k^{e,t+\Delta t}\right)^2}$ based on **B** from fitted ν-**B**^{2} and $\frac{\partial \nu}{\partial B^2}$ equations (CPU)
- timeSetup-sub2 = compute **S** with elemental ν (CPU), and compute right-hand side vector (matrix multiplication and subtraction) (GPU sparse)
- timeSetup-sub3 = compute ***G*** from equation . $\frac{\partial B^{e2}}{\partial A_i}$ and SA are computed on the GPU, and the sparse matrix assembly of ***G*** is done on the CPU.
- timeSetup-sub4 = compute the left-hand side matrix final addition (CPU).

The setup computation time results averaged over the Newton-Raphson iterations are summarized by Table 4.10. The largest part of the CPU setup calculation time, subsection 3 to compute ***G***, can be parallel processed using the sparse gpuArray matrix-vector multiplication. This subsection results in a speed-up of approximately 2.3, allowing for an overall setup time speed-up of approximately 1.8.

Table 4.10 CPU and GPU Setup Time Comparison

	Average Newton-Raphson Iteration Computation Time (s)				
CPU or GPU	Setup - sub 1	Setup - sub 2	Setup - sub 3	Setup - sub 4	Total
CPU	0.013749	0.018930	0.245237	0.000185	0.278102
GPU	0.013549	0.033317	0.107026	0.000175	0.154068
Speed-up CPU/GPU	1.014726	0.568162	2.291392	1.057076	1.805060

4.3.2.1.3 Transient CPU and hybrid CPU/GPU simulation results

The figures and tables in this section describe the transient simulation computation time for the CPU and hybrid CPU/GPU implementations. In Figure 4.22, for a few sample time steps, the

CPU and hybrid CPU/GPU simulation computation times are broken down by major component to illustrate the computation time percentage for each component and the GPU speed-up for each component. The components are:

- timesolveB – time to compute the magnetic vector potential
- timePrec – time to form the preconditioner
- timeSetup – time to set up the Newton-Raphson iteration as described in Section 4.3.2.1.2 Iteration setup time breakdown
- timesolveA – time to solve for the next Newton-Raphson iteration magnetic vector potential
- timeQ – time to calculate the next impressed current density
- timeS – time to assemble the *S* matrix
- timeUpdate – time to update the next magnetic vector potential iteration given the solution for ΔA
- timeUpdateT – when the ΔA is less than the specified tolerance, this is the time to save the iteration solution as the time step solution and update the magnetic flux density and reluctivity
- timesolveJ – time to compute the eddy current density

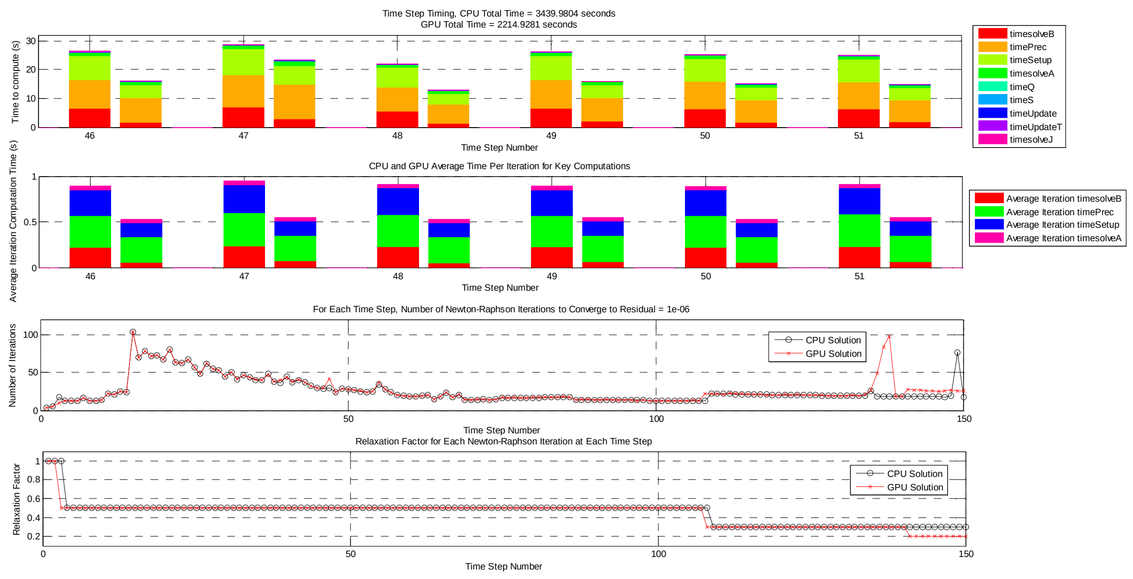

Figure 4.22 CPU and GPU computation time comparison for first-order elements, nonlinear magnetic material, fine mesh. Subset of CPU and GPU computation time for several time steps including breakdown of computation time for key computations.

Table 4.11 CPU and GPU Computation Time Comparison for Average Newton-Raphson Iteration, First-Order Elements, Nonlinear Magnetic Material Problem

Mesh	CPU or GPU	*Average Newton-Raphson Iteration Computation Time Over Total Transient Solution (s)*				
		Magnetic Flux Density	Setup	Magnetic Vector Potential Iterative Solution	Precon-ditioner	Approx. Total
Coarse	CPU	0.027664	0.053201	0.005250	0.019420	0.105535
	GPU	0.022935	0.066776	0.005671	0.019508	0.114890
	Speed-up	**1.206207**	**0.796699**	**N/A**	**N/A**	**0.918568**
Fine	CPU	0.218303	0.280088	0.036713	0.341196	0.876300
	GPU	0.060477	0.151496	0.035943	0.283171	0.531087
	Speed-up	**3.609685**	**1.848813**	**N/A**	**N/A**	**1.650013**

Table 4.12 CPU and GPU Computation Time Comparison for Total Transient Solution, First-Order Elements, Nonlinear Magnetic Material Problem

Mesh	CPU or GPU	*Total Transient Solution Computation Time (s)*				
		Magnetic Flux Density	Setup	Magnetic Vector Potential Iterative Solution	Precon-ditioner	Total
Coarse	CPU	67.597	128.695	12.771	46.817	263.609
	GPU	57.563	162.282	14.021	48.600	299.995
	Speed-up	**1.174**	**0.793**	**N/A**	**N/A**	**0.879**
Fine	CPU	856.000	1084.896	138.784	1319.007	3439.980
	GPU	253.529	622.615	149.140	1164.800	2214.928
	Speed-up	**3.376**	**1.742**	**N/A**	**N/A**	**1.553**

Note that the preconditioner formation and magnetic vector potential solver are computed on the CPU for the total GPU solution. From previous discussions, this method was used to improve the total computation time since it was not previously shown that speed-up was achieved with the sparse GPU format using the same bicgstab algorithm. From these results averaging over all the time step solutions and the average Newton-Raphson iteration computation times, Table 4.11 shows that the magnetic flux density GPU computation achieved an average speed-up of 1.2 for the coarse mesh and 3.6 for the fine mesh, and the setup achieved an average speed-up of 1.8 for the fine mesh. This is primarily due to the parallel processing of GPU sparse matrix-vector multiplication. From the total transient computation time shown in Table 4.12, the GPU implementation does not achieve speed-up for the coarse mesh, but for the fine mesh it achieves approximately 1.55 speed-up.

4.3.2.2 Second-order elements with nonlinear magnetic material

The simulation of the second-order elements, nonlinear program required more manipulation of the relaxation factor and time step difference in order to achieve convergence. For the coarse mesh, the solution only converged for times 1 to 4 ms with a time step of 1 ms. For solutions beyond that, time steps of 0.25 ms and incrementally smaller were required in order to achieve convergence. A reason for the convergence issue is due to too large of a time step given the mesh density, resulting in a larger change in magnetic vector potential for each iteration. As a result, solutions are shown for the fine mesh only. The higher mesh density reduced the convergence issues. For the fine mesh, solutions for times 1-18 ms converged for a time step of 1 ms. For solutions beyond 18 ms, a smaller time step is required to achieve convergence. Full transient solutions are not presented. For the partial simulations up to 18 ms for the fine mesh, the CPU and hybrid CPU/GPU simulation results are presented in Figure 4.23 and Figure 4.24 for the points described in Table 4.13. As previously discussed, the iterative solver used for both the CPU and hybrid CPU/GPU simulation is on the CPU using the MATLAB “bicgstab” function with row-sum modified incomplete LU Crout version factorization with drop tolerance 10^{-5} for the preconditioner. This was the fastest iterative solver implementation tested for this problem.

Table 4.13 Tracked Solution Points for Second-Order, Non-linear Program for Benchmark Problem

	Measured Points		*Fine Mesh Simulated Points*	
Search Coil Number	x (mm)	y (mm)	x (mm)	y (mm)
1	0-1.6	0	0.5	0
2	41.8	60-63.2	41	61.6
3	122.1-125.3	0	123.2	0

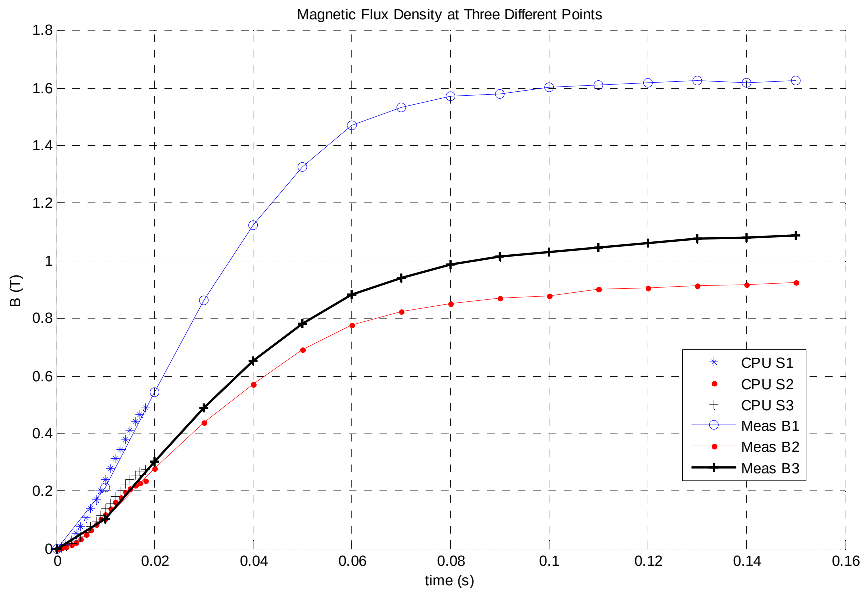

Figure 4.23 Second-order element, nonlinear material, magnetic flux density solution for fine mesh, compared to TEAM problem measured results at three points

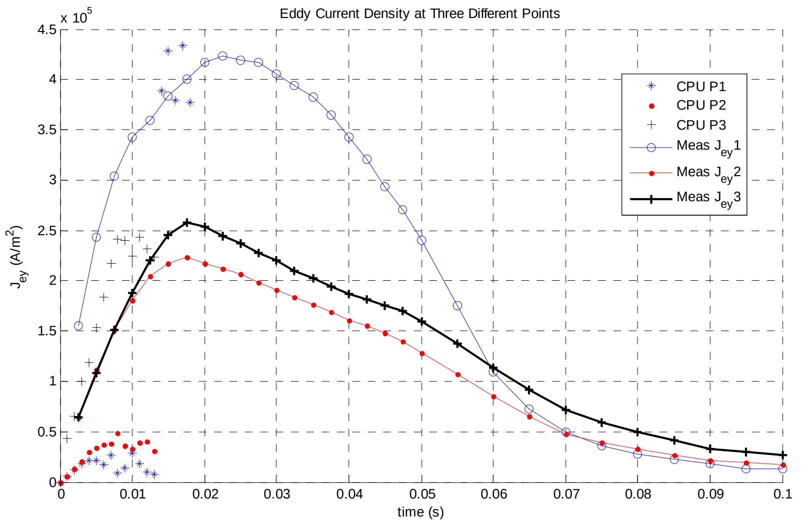

Figure 4.24 Second-order element, nonlinear material, eddy current density solution magnitude for fine mesh, compared to TEAM problem measured results at three points

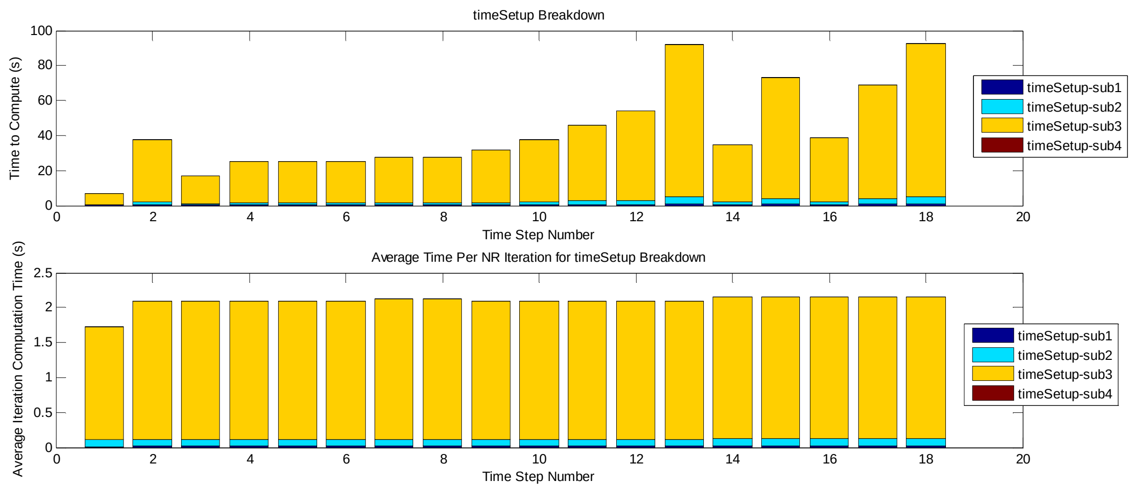

Figure 4.25 Setup time breakdown for CPU, second-order elements

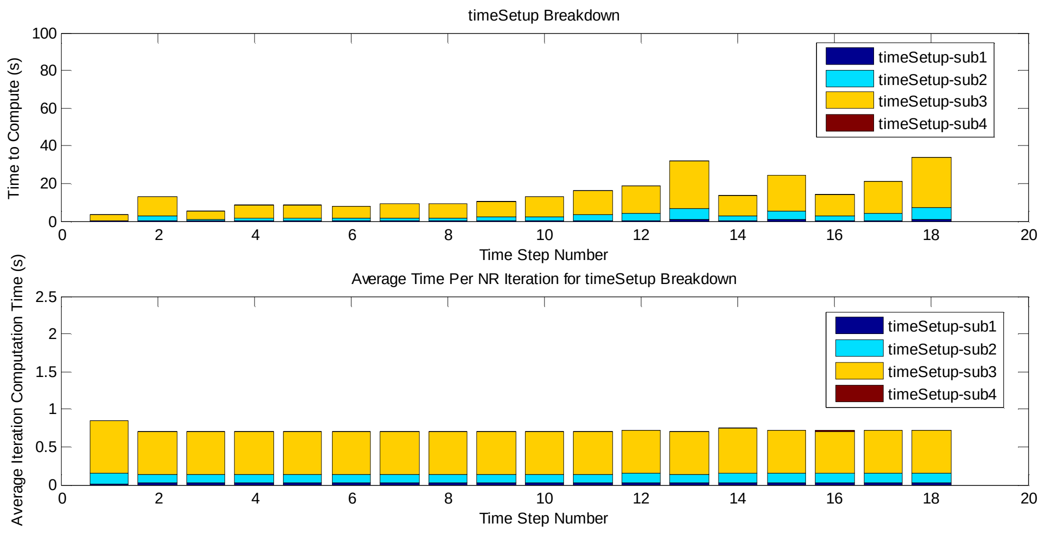

Figure 4.26 Setup time breakdown for GPU, second-order elements

To show the setup calculation time scalability, the setup calculation time by subsection is shown in Figure 4.25 for the CPU and in Figure 4.26 for the GPU. Table 4.14 summarizes the setup calculation time for the average Newton-Raphson iteration. Like for the first-order elements, the subsection 3 dominates the setup calculation time and can be parallel processed using GPUs for sparse matrix-vector multiplication. The larger problem size for the second-order elements results in a subsection 3 speed-up of approximately 3.4, and an overall setup time speed-up of 2.9.

Table 4.14 CPU and GPU Average Setup Computation Time per Iteration for Second-Order Elements, Fine Mesh

	Average Newton-Raphson Iteration Computation Time (s)				
CPU or GPU	Setup - sub 1	Setup - sub 2	Setup - sub 3	Setup - sub 4	Total
CPU	0.017544	0.096670	1.976303	0.002136	2.092652
GPU	0.018379	0.124870	0.574369	0.002113	0.719731
Speed-up CPU/GPU	**0.954584**	**0.774167**	**3.440821**	**1.010553**	**2.907546**

Figure 4.27 shows the transient solution CPU and GPU computation time by component. It is clear that the preconditioner formation time constitutes a large portion of the calculation time, followed by the setup time and magnetic flux density time. Due to the preconditioner, the sparse iterative solver time is relatively short. Table 4.15 summarizes these results showing the average component calculation time for a Newton-Raphson iteration. The magnetic flux density calculation speed-up is approximately 6.9, and the setup calculation speed-up is approximately 2.9. However, because the preconditioner formation is approximately 56% of the total iteration computation time, the overall iteration speed-up is approximately 1.4. Compared to the first-order nonlinear element problem, the overall speed-up is not as high but is comparable. The first-order nonlinear problem achieved a speed-up of 1.55 with the preconditioner formation accounting for 38% of the simulation time. For the second-order nonlinear problem, while the component speed-ups are greater due to the larger number of unknowns, the preconditioner formation accounting for 54% of the computation time limits the overall speed-up to 1.4.

Table 4.15 CPU and GPU Computation Time Comparison for Average Newton-Raphson Iteration, Second-Order Elements, Nonlinear Magnetic Material Problem. For simulation 1-18 ms.

		Average Newton-Raphson Iteration Computation Time Over Total Transient Solution (s)				
Mesh	CPU or GPU	Magnetic Flux Density	Setup	Magnetic Vector Potential Iterative Solution	Precon-ditioner	Approx. Total
Fine	CPU	1.888694	2.092652	0.177723	5.241148	9.400217
	GPU	0.271298	0.719731	0.080714	5.429043	6.500786
	Speed-up	**6.961708**	**2.907546**	**N/A**	**N/A**	**1.446012**

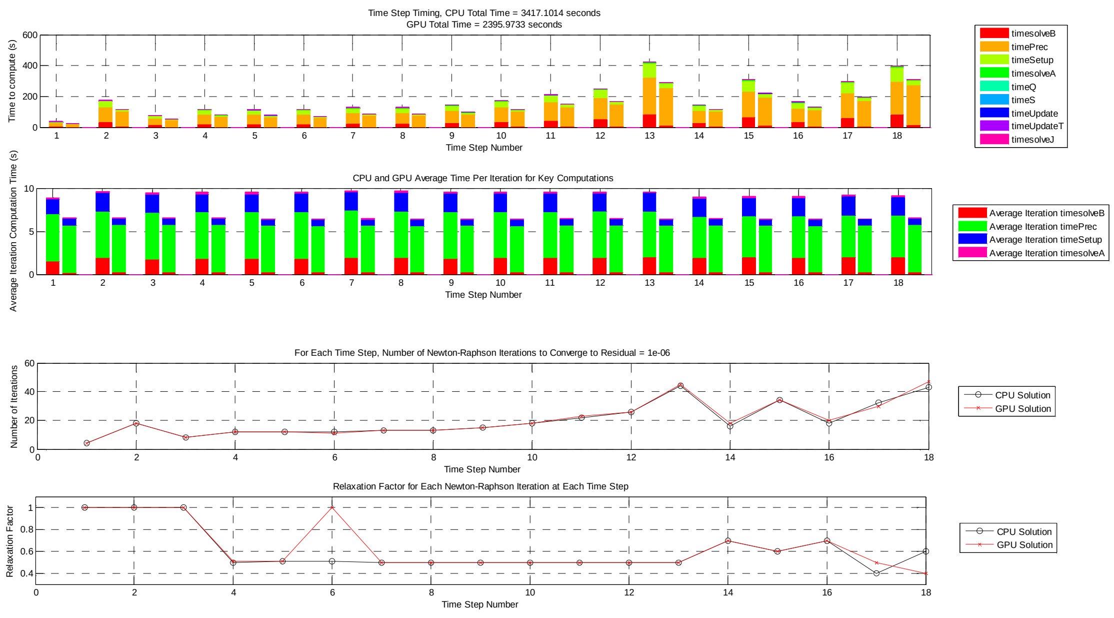

Figure 4.27 CPU and GPU computation time comparison for second-order elements, nonlinear magnetic material, fine mesh.

4.3.3 Benchmark problem simulation results summary

Table 4.16 Simulation Results Summary for Benchmark Problem

Magnetic Material Model	Element Order	Mesh	Preconditioned	Number of Nodes	*Computation Time (s)* CPU	*Computation Time (s)* Hybrid CPU/GPU	Speed-up
Linear	First	Fine	Yes	7219	54.082	29.414	1.839
	Second	Coarse	Yes	7219	65.371	54.114	1.208
	Second	Fine	No	28581	471.564	200.212	2.355
Non-Linear	First	Coarse	Yes	1842	263.609	299.995	0.879
	First	Fine	Yes	7219	3439.980	2214.928	1.553
	Second	Fine	Yes	28581	3417.101	2395.973	1.426

For the discussed simulations, Table 4.16 summarizes the CPU and GPU simulation computation times. It shows that as the problem scale increases for both the linear and nonlinear simulations, the speed-up achieved also increases. For the nonlinear simulation, due to the significance of the preconditioner formation time which is only computed on the CPU for these simulations, the overall speed-up is limited as the problem size increases.

CHAPTER 5
LINEAR INDUCTION MACHINE EXPERIMENT AND SIMULATION

5.1 Experiment Description

The induction machine experiment chosen to estimate the validity of the finite element CPU and GPU models is the double-sided stator linear induction machine (LIM). The machine is described in [48]. Measurable experiments for the LIM with a solid aluminum rotor were conducted. For the applied stator current and frequency from a constant volts-per-Hertz drive, the force on the rotor for a steady-state locked position was measured by a spring scale. The linear induction machine and experiment are depicted in Figure 5.1 from [49].

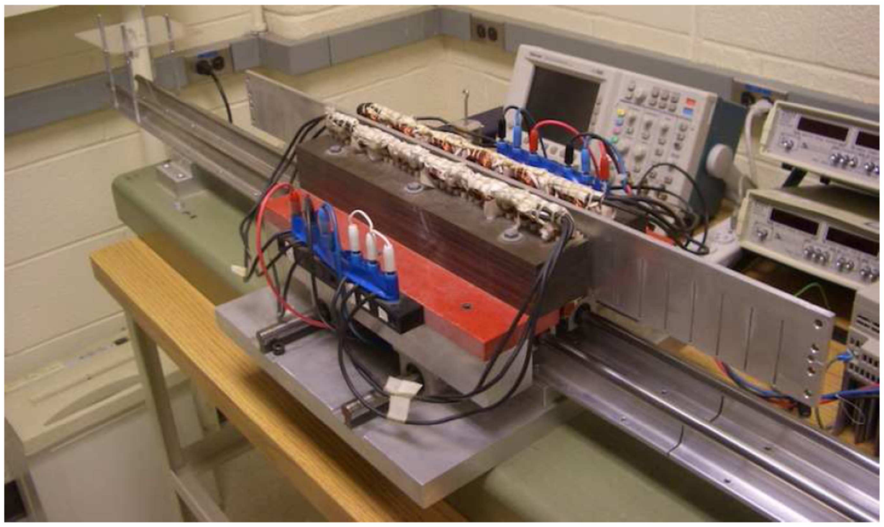

(a)

Figure 5.1(a) Laboratory LIM setup

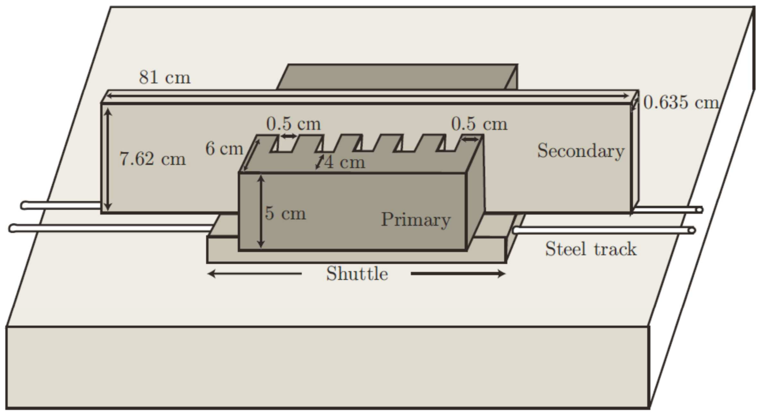

(b)

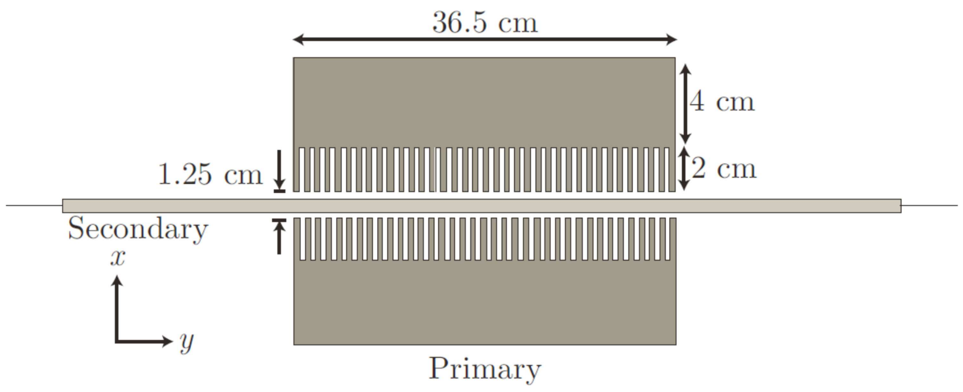

(c)

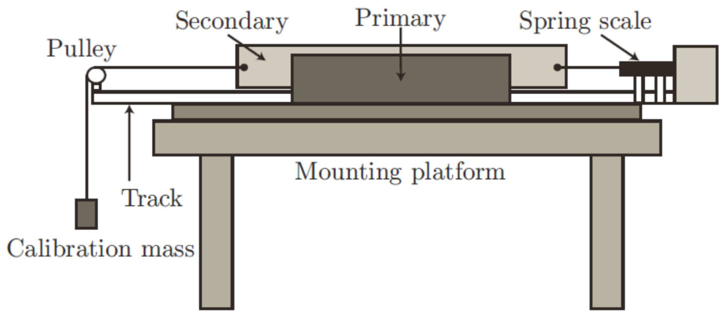

(d)

Figure 5.1(cont.) (b) subset of LIM geometry for 5 stator slots, (c) cross section of double stator and rotor showing 36 stator slots, and (d) experimental setup with calibration mass

The LIM is excited using symmetric three-phase excitation for a single-layered, series-wound stator. There are 35 turns per slot, and the pole pitch is 3 cm accordingly. The stator laminations are constructed with M19 steel. The solid aluminum rotor (alloy Al6061 with T611 temper) has conductivity $\sigma = 2.4662 \text{ x } 10^7 \text{ S/m}$. The rotor is free to move laterally parallel to the stator.

The experiment conducted from [49] attached a nylon string to the LIM rotor. On one end, the string was attached to a stabilizing spring scale, and on the other end, it was attached to a mass through a pulley. The mass was known and used to calibrate the spring scale. For specified operating frequencies, the drive excited the rotor so that force was created away from the spring scale. The total force measured was read by the spring scale. In addition, the stator excitation current was measured for the operating frequency.

From the measured results recorded in [49], the data point chosen for finite element simulation is shown in Table 5.1. The volts-per-Hertz drive ratio excitation used is 40/60 Vs.

Table 5.1 LIM Experiment Measurements

f_s *(Hz)*	$I_{s,RMS}$ *(A)*	*F (meas.) (N)*
14	8.64	7.20

5.2 FE Simulation of Experiment

Based on the LIM geometry shown in Figure 5.1, a mesh was created for a subset of the geometry for the partial differential equation simulation. Taking advantage of the periodicity of the machine, six stator slots were simulated. The fine mesh is shown in Figure 5.2. The a-, b-, and c-phase excitation polarity is such that the windings for the three left-most slots are out of the page, and the three right-most slots are into the page. This applies to both the upper and lower stators. Additional domains are created in the air gap to more readily compute the force in it. The elements or nodes along the specified *y* coordinate along the edge of the domain are used for force calculation using the Maxwell stress tensor method. Figure 5.3 shows the fine mesh closer to the rotor and air gap. The green-filled elements are the first-order elements used to calculate the force in the air gap. The force along the edge of the rotor is also calculated.

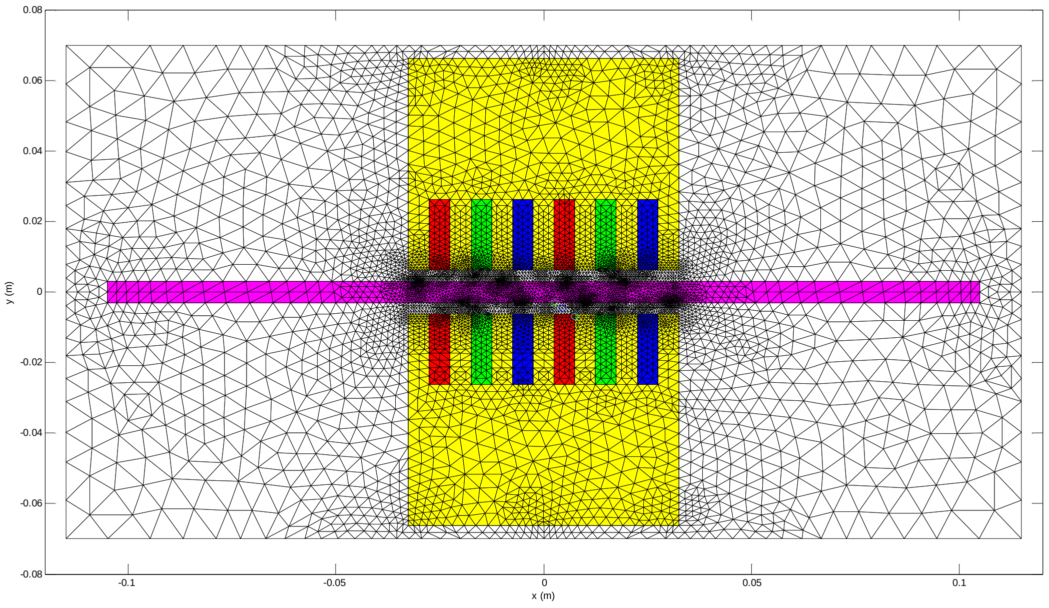

Figure 5.2 Linear induction machine fine mesh for six stator slots

Several assumptions are made for numerical simulation of the LIM experiment. The steel conductivity is assumed to be zero. The steel magnetic permeability is simulated as linear with an approximate relative permeability of $\mu_r = 8754$ [50]. The resulting solution is not as sensitive to the saturation of the magnetic steel as other machine problems because the air gap is relatively large. The winding slot fill is assumed to be 100%, resulting in the impressed current density calculated over the entire winding area. The impressed current density is also even over the winding area. As with the benchmark problem, the two-dimensional approximation of the LIM results in the impressed current density simulated as infinite in the *z*-direction.

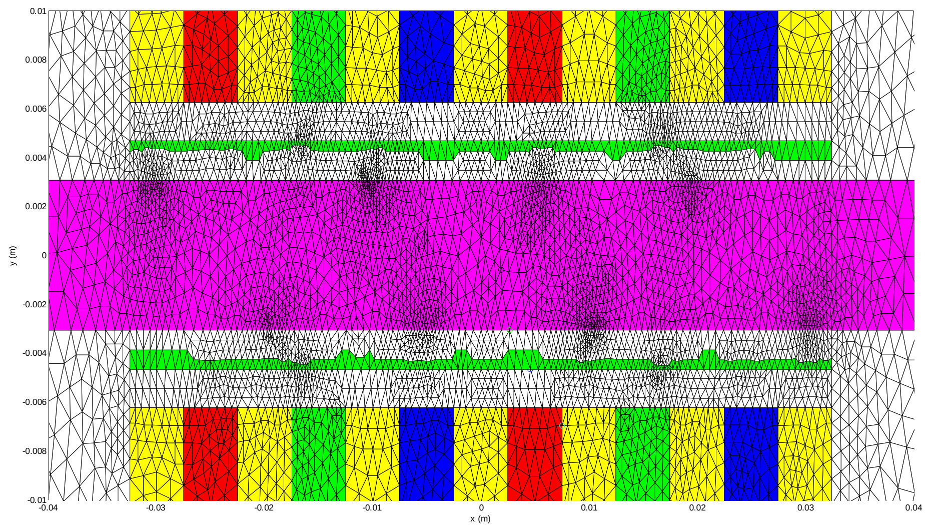

Figure 5.3 Linear induction machine fine mesh view near air gap. Green-filled elements are used for force calculation in the air gap for first-order elements.

For the above assumptions, the CPU and GPU simulations of the LIM are calculated for the first- and second-order elements. Magnetic vector potential, magnetic flux density, and eddy current solutions are tracked at four elements or nodes: the middle of the air gap, on the aluminum rotor surface, in the middle of the aluminum rotor, and on the stator steel near the air gap. The coordinates for these tracked solutions are given in Table 5.2.

Table 5.2 Tracked Solution Points for LIM Problem

Tracked Node Description	*Simulated Points*	
	x (m)	y (m)
Middle Air Gap	0.00455	-0.00466
On Rotor Surface	0.00266	-0.00308
Middle of Rotor	0.00187	-0.00059
Stator Steel	0.00750	-0.00696

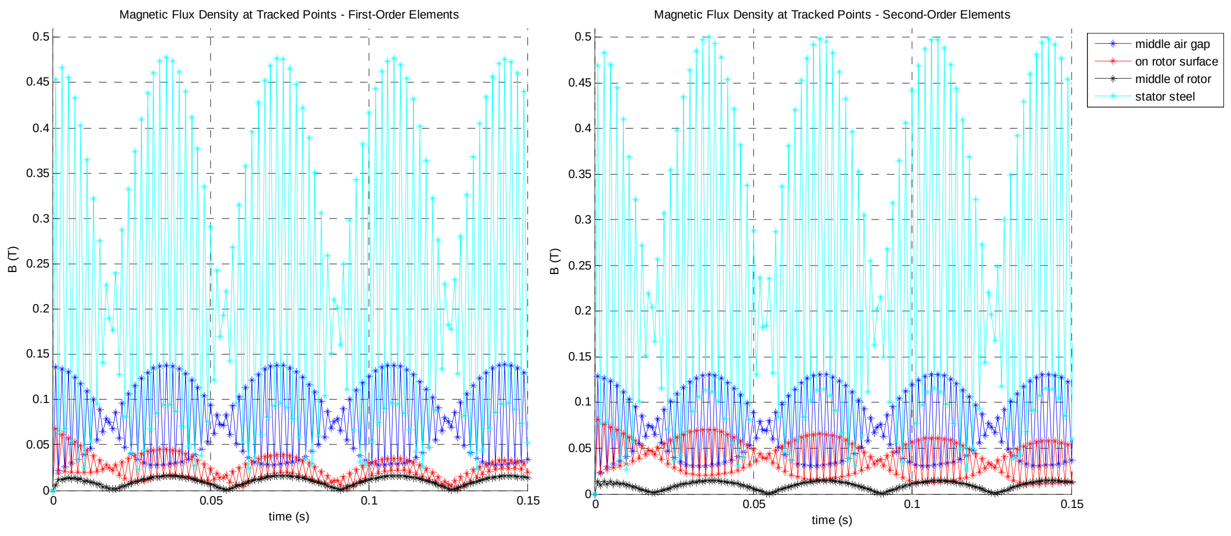

(a) (b)

Figure 5.4 Simulated magnetic flux density magnitude at tracked points for (a) first-order elements, and (b) second-order elements

The computed LIM magnetic flux density magnitude solutions for the first- and second-order elements are shown in Figure 5.4. For both simulations, the highest magnetic flux density is in the stator steel as expected for induction machine design. The periodicity of the solutions shown for a 14 Hz excitation is due to the periodic excitation. Since the magnetic flux density magnitude is shown, all values are positive. The oscillation within each period may be due to the numerical time discretization of the simulation. The results shown are for a time step of 1 ms. When the time step was reduced, the same oscillation within each period occurred, with one time step solution lower or higher than the next. Comparing the first- and second-order magnetic flux density solution magnitudes, the simulations match closely. The second-order elements simulated slightly higher magnetic flux density in the stator steel.

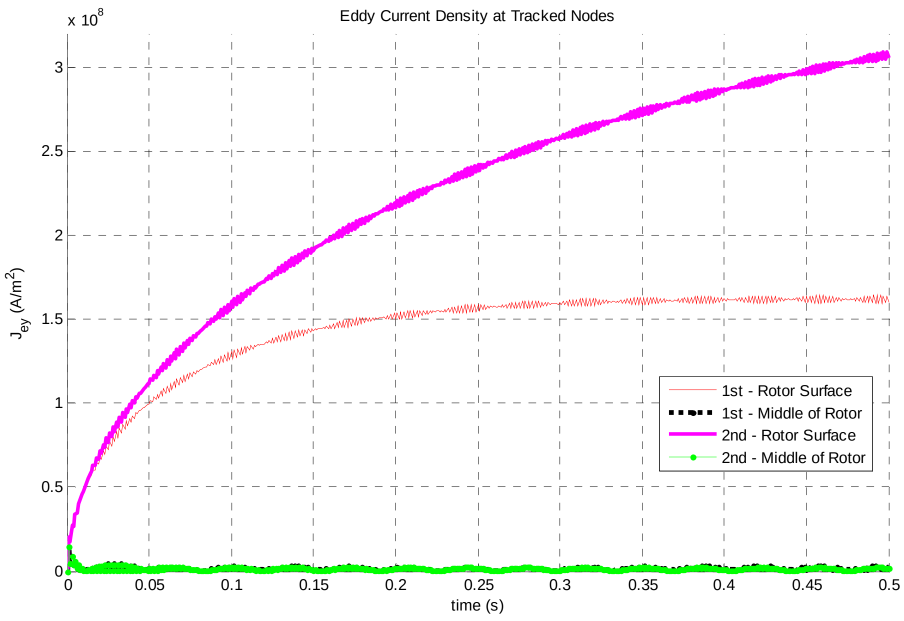

Figure 5.5 Simulated eddy current density magnitude at rotor tracked points for first- and second-order elements

The simulated eddy current density is shown in Figure 5.5 for the rotor surface and middle of the rotor. The eddy current density is zero for the tracked stator steel and air gap points and is not shown in Figure 5.5. As expected, the eddy current density is significant and greater on the rotor surface compared to the middle of the rotor. The second-order eddy current density on the rotor surface continues to increase over time while the first-order eddy current density on the rotor surface increases then remains constant on average after approximately 0.35 seconds. However, the first- and second-order simulated solutions are on the same order of magnitude.

The force per unit length is calculated according to the Maxwell Stress Tensor method in section 2.5.3 Force from Maxwell Stress Tensor. The force density (N/m^2) is calculated at each point around the desired path. To numerically integrate along the path, the trapezoidal rule is used. The numerical integration yields the force per unit length for the given time step solution. The results shown in Figure 5.6 are calculated in newtons based on multiplying the force per unit length times the stator height for the air gap force or the rotor height for the force on the rotor surface.

The upper and lower forces are summed to calculate the force on the rotor. The total force taken over the average of the last cycle simulated is shown in Table 5.3. Both the first- and second-order simulated forces on the aluminum rotor edge are lower than the measured force. The simulated force along the rotor edge is closer to the measured result than the simulated force along the air gap. Factors that could contribute to the differences between measured and simulated results are the two-dimensional approximation, and simulating a subset of the stator and stator windings.

Table 5.3 Measured and Simulated LIM Force Calculations

	Force (N)		
Region	**Measured**	**First-Order Elements Simulation**	**Second-Order Elements Simulation**
Al Rotor Edge	7.20	4.40	3.61
Along Air Gap	7.20	0.16	0.08

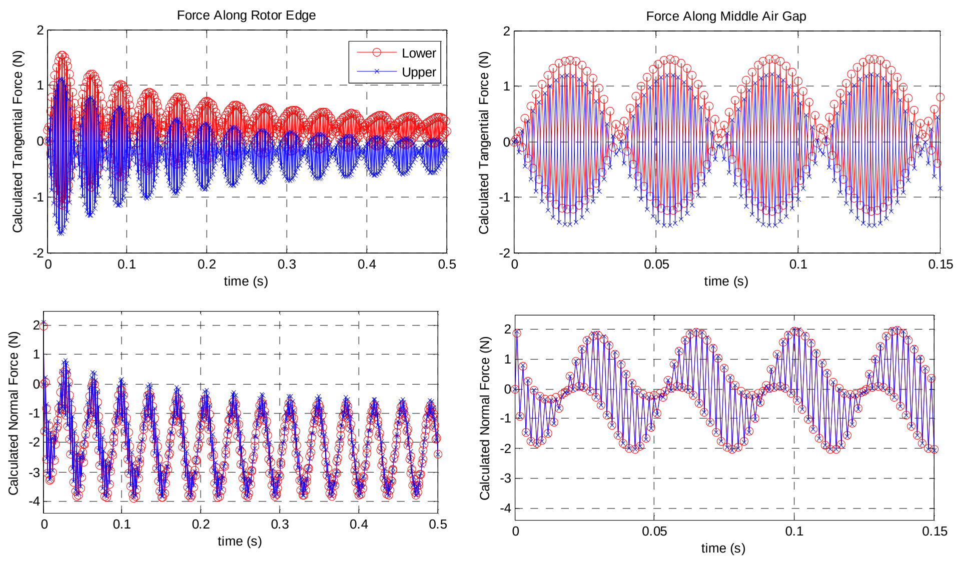

(a)

Figure 5.6 Calculated tangential and normal force along LIM rotor edge and middle of the air gap for (a) first-order elements

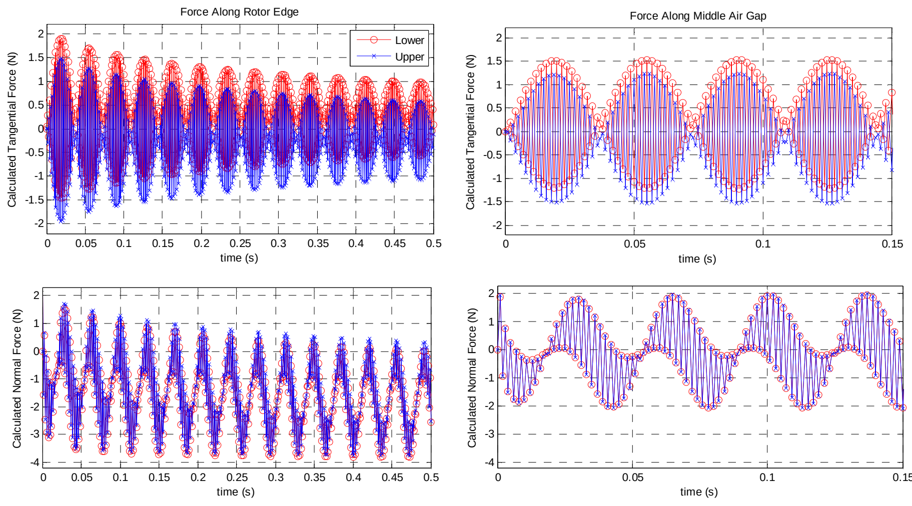

(b)

Figure 5.6 (cont.) Calculated tangential and normal force along LIM rotor edge and middle of the air gap for (b) second-order elements

The CPU and hybrid CPU/GPU simulations of the linear LIM problem were conducted to compare computation time. The hybrid CPU/GPU simulation follows the implementation for the benchmark problem for the first- and second-order elements with linear magnetic material. Due to the large air gap, the steel will not normally saturate for this LIM experiment. As a result, the magnetic permeability of the steel can be approximated linearly. The hybrid CPU/GPU simulation uses the GPU for matrix-vector multiplication to form the right-hand side vector and to compute the magnetic flux density. As discussed previously, the biconjugate gradient iterative solver is implemented on the CPU using the MATLAB built-in function bicgstab, and the preconditioner is formed on the CPU using the incomplete Cholesky factorization function ichol. Additionally, the force density calculation is done on the CPU since it is computed element-wise. This type of calculation is much faster on the CPU than the GPU.

Table 5.4 LIM Problem Mesh Description

Magnetic Material Model	Element Order	Mesh	*Total Domain* Number of Nonzero Elements in Matrix	Number of Elements	Number of Nodes
Linear	First	Fine	56517	16416	8281
	Second	Fine	297219	16416	32977

Table 5.5 CPU and hybrid CPU/GPU simulation times for LIM linear problem, first- and second-order elements over 500 ms simulation

			Total Time (s)		
		Preconditioner Time (s)	**Iterative Solver**	**Magnetic Flux Density**	**Total Time (s)**
First Order	CPU	0.006	23.984	73.330	111.322
	GPU	0.005	9.973	15.353	38.567
	Speed-up	**N/A**	**N/A**	**4.776**	**2.886**
Second Order	CPU	0.007	1550.500	676.252	2235.600
	GPU	0.006	496.544	110.618	638.870
	Speed-up	**N/A**	**N/A**	**6.113**	**3.499**

Table 5.4 shows the first- and second-order mesh descriptions. Table 5.5 shows the CPU and hybrid CPU/GPU simulation times. While the iterative solver was calculated on the CPU for both simulations, the hybrid CPU/GPU simulation calculated the iterative solution faster. For the larger problem size for the second-order elements, greater speed-up is achieved. A speed-up of approximately 4.7 and 6.1 was achieved for the first- and second-order magnetic flux density calculation, respectively. The overall speed-up resulted in 2.8 for the first-order elements, and 3.5 for the second-order elements. The problem size for the LIM mesh is slightly larger than for the benchmark problem. Using similar techniques, greater speed-up is achieved with the larger problem size.

CHAPTER 6
CONCLUSION AND FUTURE WORK

The use of GPUs for parallel processing of the two-dimensional transient finite element analysis problem was explored. Simulation results for the benchmark and linear induction machine problems show which simulation GPUs can be used to speed up the finite element analysis simulation computation time and where their functionality is limited. MATLAB implementations of first- and second-order elements for linear and nonlinear magnetic material were created, and the simulation results for these finite element analysis programs were presented. For the sparsity and problem sizes simulated, the GPUs provided speed-up for a range of approximately 4 to 11 times for sparse matrix-vector multiplication required for magnetic flux density calculation and Jacobian formulation. However, GPUs did not speed up the sparse iterative solver simulation time for each type of simulation. The CPU iterative solver used was the MATLAB sparse-format based preconditioned biconjugate gradient stabilized method. These CPU iterative solver times were compared to the CUDA biconjugate gradient functions explored and linked to MATLAB and the preconditioned and un-preconditioned biconjugate gradient stabilized method algorithm implementation using the sparse gpuArray format. Based on these simulation results and prior research for GPU iterative solver implementations [35], [36], the current algorithms available and implemented on the GPU do not result in faster computation times for the GPU implementations for problems of this size (1842-32977 nodes). From [35], for problem sizes ranging from 150,000 to 1.5 million rows and columns, speed-up achieved for the incomplete-LU and Cholesky preconditioned BiCGStab and CG methods ranged from 1 to 5.5. Different speed-up was achieved for different values of the preconditioner fill-in threshold. For problems of varying sparsity, the average speed-up was approximately 2.2. From [36], the level scheduling technique was used for the sparse triangular solve and several preconditioned iterative methods on the GPU were explored for problems from 5,000 to 1.4 million rows and columns. The greatest GPU speed-up achieved was 4.3 for the GPU-accelerated ILUT-GMRES method for the matrix with 1.27 million rows and columns. Through use of algorithms favorable to maximizing the parallel thread computations given the sparsity of the finite element matrix, such as level scheduling in [36], it may be possible to improve the GPU performance of the biconjugate gradient or GMRES solver over the CPU for two-dimensional finite element problem sizes. However, the author expects these algorithms will provide limited improvements if any for this problem size compared to the speed-up achieved for sparse matrix-vector multiplication.

To combine the simulation components with the fastest CPU and GPU computation times, hybrid CPU/GPU simulation experiments were conducted. Matrix assembly, vector addition and subtraction, preconditioner formation, and the sparse iterative solver were implemented on the CPU, while the sparse matrix-vector multiplication operations were implemented on the GPU. This required transferring matrices and vectors to and from the CPU and GPU. Such transfers should be minimized since they contribute to GPU processing overhead. For the two-dimensional problem sizes, this transfer time was minimal compared to the speed-up achieved for GPU sparse matrix-vector multiplication. As a result, it was still advantageous to use GPUs for these parts of the simulation.

These hybrid CPU/GPU simulation results were compared to the CPU-only simulation results. Depending on the problem size, overall simulation speed-ups achieved for the benchmark and LIM problems ranged from 2.3 to 3.5, with the largest problem size simulated consisting of 32977 nodes. The speed-up is limited by the component speed-up achieved and percentage of the faster component computation time relative to the remainder of the simulation computation time.

The use of GPUs for parallel processing for even larger finite element analysis problems, such as three-dimensional domains, will show the scalability and limitations of their processing capabilities for electromagnetic analysis of electric machines. For larger scale problems, the CUDA preconditioner and sparse iterative solver functions may provide speed-up, but this is highly dependent on the sparsity of the problem. From three-dimensional mechanics finite element problems with 147,900 rows and columns with 3.5 million nonzero elements analyzed in [35], speed-up was not achieved for the fastest overall method tested - the preconditioned CG and BiCGStab methods with 0 fill. For slower overall methods using higher fill in thresholds, moderate speed-up of 1.1-6.28 was achieved. Ideally, speed-up on the GPU should be achieved for the CPU fastest possible available method. For the triangular solve with level scheduling for the 3D Poisson problem in [36], the GPU implementation had a speed-up of approximately 2.3, and the triangular solve of multi-color ILU with zero fill in had a speed-up of approximately 5.34 on the GPU over the CPU.

Additionally, the scalability of the sparse matrix-vector multiplication can be explored for the larger problem. For the sparse-matrix vector results presented, the GPU speed-up over the CPU increased from 1.49 to 11 with increasing problem size in terms of the matrix number of nonzero elements and the number of nodes in the mesh. From the 3D Poisson problem analyzed in [36] with 85,000 rows and columns and 2.3 million nonzero elements, the greatest GPU sparse matrix-vector multiplication achieved was approximately 5.3 using double precision floating point arithmetic. As a result, the speed-up for sparse matrix-vector multiplication applied to three-dimensional finite element problems is expected to be in the range of 5-10.

Along with finite element analysis, GPU parallel computing can be used for magnetic equivalent circuits (MEC) [51], the boundary-element method [52], and finite element analysis coupled to circuit equivalent models [3]. Each of these types of models requires the solution of a system of equations. GPUs can be applied to the components of these types of models where they are suitable for parallel processing, such as sparse matrix-vector multiplication or sparse iterative solvers for large problem sizes.

Additionally, numerical and parallel processing techniques can be explored in conjunction to further accelerate the more detailed electromagnetic simulation of the electric machine. Such an approach could involve creating a hybrid three-dimensional MEC-FEA simulation by using MEC to simulate flux density and field intensity for a certain transient duration, providing an estimated initial condition for an FEA transient simulation. The MEC reluctance network could be mapped to a similar FEA mesh, and then the FEA simulation could be used for more detailed analysis to capture eddy current. GPUs could be applied to certain components of the MEC and FEA simulations to further speed-up the simulation. Compared to an FEA-only CPU-based transient analysis solution, such a hybrid approach along with the use of GPUs could result in faster computation times.

APPENDIX A
CUDA SOURCE CODE FOR MATLAB MEX FUNCTION: SPARSE MATRIX-VECTOR MULTIPLICATION USING CSR FORMAT

```
/*
 * Copyright (c) 2013, The Regents of the University of California,
 * through Lawrence Berkeley National Laboratory (subject to receipt of
 * any required approvals from U.S. Dept. of Energy) All rights reserved.
 *
 * Redistribution and use in source and binary forms, with or
 * without modification, are permitted provided that the
 * following conditions are met:
 *
 *     * Redistributions of source code must retain the above
 * copyright notice, this list of conditions and the following
 * disclaimer.
 *
 *     * Redistributions in binary form must reproduce the
 * above copyright notice, this list of conditions and the
 * following disclaimer in the documentation and/or other
 * materials provided with the distribution.
 *
 *     * Neither the name of the University of California,
 * Berkeley, nor the names of its contributors may be used to
 * endorse or promote products derived from this software
 * without specific prior written permission.
 *
 * THIS SOFTWARE IS PROVIDED BY THE COPYRIGHT HOLDERS AND
 * CONTRIBUTORS "AS IS" AND ANY EXVPRESS OR IMPLIED WARRANTIES,
 * INCLUDING, BUT NOT LIMITED TO, THE IMPLIED WARRANTIES OF
 * MERCHANTABILITY AND FITNESS FOR A PARTICULAR PURPOSE ARE
 * DISCLAIMED. IN NO EVENT SHALL THE COPYRIGHT OWNER OR
 * CONTRIBUTORS BE LIABLE FOR ANY DIRECT, INDIRECT, INCIDENTAL,
 * SPECIAL, EXVEMPLARY, OR CONSEQUENTIAL DAMAGES (INCLUDING,
 * BUT NOT LIMITED TO, PROCUREMENT OF SUBSTITUTE GOODS OR
 * SERVICES; LOSS OF USE, DATA, OR PROFITS; OR BUSINESS
 * INTERRUPTION) HOWEVER CAUSED AND ON ANY THEORY OF LIABILITY,
 * WHETHER IN CONTRACT, STRICT LIABILITY, OR TORT (INCLUDING
 * NEGLIGENCE OR OTHERWISE) ARISING IN ANY WAY OUT OF THE USE
 * OF THIS SOFTWARE, EVEN IF ADVISED OF THE POSSIBILITY OF
 * SUCH DAMAGE.
 *
 * Stefano Marchesini, Lawrence Berkeley National Laboratory, 2013
 */

#include <cuda.h>
#include <cusp/complex.h>
#include <cusp/blas.h>
#include<cusp/csr_matrix.h>
#include<cusp/multiply.h>
#include <cusp/array1d.h>
#include <cusp/copy.h>
#include <thrust/device_ptr.h>
```

```
#include "mex.h"
#include "gpu/mxGPUArray.h"

/* Input Arguments */
#define VAL prhs[0]
#define COL prhs[1]
#define ROWPTR prhs[2]
// #define NCOL    prhs[3]
// #define NROW    prhs[4]
// #define NNZ    prhs[5]
#define XV    prhs[3]


/* Output Arguments */
#define Yplhs[0]

void mexFunction(int nlhs, mxArray * plhs[], int nrhs,const mxArray * prhs[]){

    mxGPUArray const *Aval;
    mxGPUArray const *Acol;
    mxGPUArray const *Aptr;
    mxGPUArray const *x;
    mxGPUArray  *y;

//     int nnzs = lrint(mxGetScalar(NCOL));
//     int nrows = lrint(mxGetScalar(NROW));
//     int nptr=nrows+1;
//     int nnz  = lrint(mxGetScalar(NNZ));
//

    /* Initialize the MathWorks GPU API. */
    mxInitGPU();

    /*get matlab variables*/
    Aval = mxGPUCreateFromMxArray(VAL);
    Acol = mxGPUCreateFromMxArray(COL);
    Aptr = mxGPUCreateFromMxArray(ROWPTR);
    x    = mxGPUCreateFromMxArray(XV);

    int nnz=mxGPUGetNumberOfElements(Acol);
    int nrowp1=mxGPUGetNumberOfElements(Aptr);
    int ncol =mxGPUGetNumberOfElements(x);


    mxComplexity isXVreal = mxGPUGetComplexity(x);
    mxComplexity isAreal = mxGPUGetComplexity(Aval);
    const mwSize ndim= 1;
    const mwSize dims[]={(mwSize) (nrowp1-1)};

    if (isAreal!=isXVreal)
    {
        mexErrMsgTxt("Aval and X must have the same complexity");
        return;
    }

    if(mxGPUGetClassID(Aval) != mxSINGLE_CLASS||
   mxGPUGetClassID(x)!= mxSINGLE_CLASS||
   mxGPUGetClassID(Aptr)!= mxINT32_CLASS||
   mxGPUGetClassID(Acol)!= mxINT32_CLASS){
     mexErrMsgTxt("usage: gspmv(single, int32, int32, single)");
     return;
    }

    //create output vector
    y = mxGPUCreateGPUArray(ndim,dims,mxGPUGetClassID(x),isAreal,
MX_GPU_DO_NOT_INITIALIZE);


    /* wrap indices from matlab */
    typedef const int  TI;  /* the type for index */
    TI *d_col =(TI  *)(mxGPUGetDataReadOnly(Acol));
    TI *d_ptr =(TI  *)(mxGPUGetDataReadOnly(Aptr));
    // wrap with thrust::device_ptr
    thrust::device_ptr<TI>    wrap_d_col  (d_col);
    thrust::device_ptr<TI>    wrap_d_ptr  (d_ptr);
    // wrap with array1d_view
    typedef typename cusp::array1d_view< thrust::device_ptr<TI> >   idx2Av;
    // wrap index arrays
    idx2Av colIndex (wrap_d_col , wrap_d_col + nnz);
    idx2Av ptrIndex (wrap_d_ptr , wrap_d_ptr + nrowp1);

    if (isAreal!=mxREAL){

        typedef const cusp::complex<float> TA;  /* the type for A */
        typedef const cusp::complex<float> TXV; /* the type for X */
        typedef cusp::complex<float> TYV; /* the type for Y */

        // wrap with array1d_view
        typedef typename cusp::array1d_view< thrust::device_ptr<TA > >   val2Av;
        typedef typename cusp::array1d_view< thrust::device_ptr<TXV > >   x2Av;
        typedef typename cusp::array1d_view< thrust::device_ptr<TYV > >   y2Av;

        /* pointers from matlab */
        TA *d_val =(TA  *)(mxGPUGetDataReadOnly(Aval));
        TXV *d_x   =(TXV  *)(mxGPUGetDataReadOnly(x));
        TYV *d_y   =(TYV  *)(mxGPUGetData(y));

        // wrap with thrust::device_ptr
        thrust::device_ptr<TA >    wrap_d_val  (d_val);
        thrust::device_ptr<TXV >    wrap_d_x    (d_x);
        thrust::device_ptr<TYV >    wrap_d_y  (d_y);

        // wrap  arrays
        val2Av valIndex (wrap_d_val , wrap_d_val + nnz);
        x2Av xIndex   (wrap_d_x   , wrap_d_x   + ncol);
        y2Av yIndex(wrap_d_y, wrap_d_y+ nrowp1-1);
//         y2Av yIndex(wrap_d_y, wrap_d_y+ ncol);

        // combine info in CSR matrix
        typedef  cusp::csr_matrix_view<idx2Av,idx2Av,val2Av> DeviceView;

        DeviceView As(nrowp1-1, ncol, nnz, ptrIndex, colIndex, valIndex);

        // multiply matrix
```

```
        cusp::multiply(As, xIndex, yIndex);

    }
     else{

        typedef const float TA;  /* the type for A */
        typedef const float TXV; /* the type for X */
        typedef float TYV; /* the type for Y */

        /* pointers from matlab */
        TA *d_val =(TA  *)(mxGPUGetDataReadOnly(Aval));
        TXV *d_x   =(TXV  *)(mxGPUGetDataReadOnly(x));
        TYV *d_y   =(TYV  *)(mxGPUGetData(y));

        // wrap with thrust::device_ptr!
        thrust::device_ptr<TA >    wrap_d_val  (d_val);
        thrust::device_ptr<TXV >    wrap_d_x    (d_x);
        thrust::device_ptr<TYV >    wrap_d_y  (d_y);
        // wrap with array1d_view
        typedef typename cusp::array1d_view< thrust::device_ptr<TA > >   val2Av;
        typedef typename cusp::array1d_view< thrust::device_ptr<TXV > >   x2Av;
        typedef typename cusp::array1d_view< thrust::device_ptr<TYV > >   y2Av;

        // wrap  arrays
        val2Av valIndex (wrap_d_val , wrap_d_val + nnz);
        x2Av xIndex   (wrap_d_x   , wrap_d_x   + ncol);
        //y2Av yIndex(wrap_d_y, wrap_d_y+ ncol);
        y2Av yIndex(wrap_d_y, wrap_d_y+ nrowp1-1);

        // combine info in CSR matrix
        typedef  cusp::csr_matrix_view<idx2Av,idx2Av,val2Av> DeviceView;

        DeviceView As(nrowp1-1, ncol, nnz, ptrIndex, colIndex, valIndex);

        // multiply matrix
        cusp::multiply(As, xIndex, yIndex);

    }

    Y = mxGPUCreateMxArrayOnGPU(y);

    mxGPUDestroyGPUArray(Aval);
    mxGPUDestroyGPUArray(Aptr);
    mxGPUDestroyGPUArray(Acol);
    mxGPUDestroyGPUArray(x);
    mxGPUDestroyGPUArray(y);

    return;
}
```

APPENDIX B

CUDA SOURCE CODE FOR MATLAB MEX FUNCTION: BICONJUGATE GRADIENT SPARSE ITERATIVE SOLVER

```
#include "mex.h"
#include "cuda.h"
#include "gpu/mxGPUArray.h"
#include <string.h>
#include <iostream>
#include <time.h>
#include <windows.h>
#include <float.h>

#define DEBUG 1

#include <cusp/blas.h>
#include <cusp/copy.h>
#include <cusp/gallery/random.h>
#include <cusp/coo_matrix.h>

#include <cusp/krylov/bicg.h>
#include <cusp/krylov/bicgstab.h>
#include <cusp/krylov/cg.h>
#include <cusp/krylov/gmres.h>

#include <cusp/io/matrix_market.h>

void mexFunction (int nlhs, mxArray *plhs[], int nrhs, const mxArray *prhs[])
{
 /* define timer variables */
    /* unsigned int kernelTime;
    cutCreateTimer(&kernelTime);
    cutResetTimer(kernelTime);*/
 LARGE_INTEGER frequency, start, end;
    double seconds;

    /* Read in one sparse matrix */
    mwSize nnz_A = mxGetNzmax(prhs[0]);

    /* Create the three arrays needed to represent matrix in COO format */
    mxArray *matlab_coo_A[] = {
        mxCreateNumericArray(1, &nnz_A, mxDOUBLE_CLASS, mxREAL),
        mxCreateNumericArray(1, &nnz_A, mxDOUBLE_CLASS, mxREAL),
        mxCreateNumericArray(1, &nnz_A, mxDOUBLE_CLASS, mxREAL)
    };
    mexCallMATLAB(3, matlab_coo_A, 1, (mxArray**)(&prhs[0]), "find");

    /* Create a cusp matrix on the host */
    cusp::coo_matrix<int, double, cusp::host_memory> A(mxGetM(prhs[0]),
                                                       mxGetN(prhs[0]),
                                                       nnz_A);
    double *row = (double*)mxGetData(matlab_coo_A[0]);
    double *col = (double*)mxGetData(matlab_coo_A[1]);
    for (int i = 0; i < nnz_A; i++)
    {
        A.row_indices[i] = row[i] - 1;
        A.column_indices[i] = col[i] - 1;
    }
    memcpy(&A.values[0],         mxGetData(matlab_coo_A[2]), sizeof(double) * nnz_A);

    /* Copy to GPU */
    cusp::coo_matrix<int, double, cusp::device_memory> gpuA = A;
    /* A = gpuA; */

#if DEBUG
    cusp::io::write_matrix_market_file(A, "A.mtx");
#endif

    /* Read in a full vector */
    mwSize A_num_rows = mxGetM(prhs[0]);
    cusp::array1d<double, cusp::host_memory> B(A_num_rows);
    memcpy(&B[0], mxGetData(prhs[1]), sizeof(double) * A_num_rows);

    /* Copy to GPU */
    cusp::array1d<double, cusp::device_memory> gpuB = B;
    /* B = gpuB; */

#if DEBUG
    cusp::io::write_matrix_market_file(B, "B.mtx");
#endif

    /* Read in a full vector */
    cusp::array1d<double, cusp::host_memory> x(A_num_rows);
    memcpy(&x[0], mxGetData(prhs[2]), sizeof(double) * A_num_rows);

    /* Copy to GPU */
    cusp::array1d<double, cusp::device_memory> gpux = x;
    /* x = gpux; */

#if DEBUG
    cusp::io::write_matrix_market_file(x, "x.mtx");

#endif

  /* Read in one sparse matrix */
    mwSize nnz_M = mxGetNzmax(prhs[3]);

    /* Create the three arrays needed to represent matrix in COO format */
    mxArray *matlab_coo_M[] = {
        mxCreateNumericArray(1, &nnz_M, mxDOUBLE_CLASS, mxREAL),
        mxCreateNumericArray(1, &nnz_M, mxDOUBLE_CLASS, mxREAL),
        mxCreateNumericArray(1, &nnz_M, mxDOUBLE_CLASS, mxREAL)
    };
    mexCallMATLAB(3, matlab_coo_M, 1, (mxArray**)(&prhs[3]), "find");

    /* Create a cusp matrix on the host */
    cusp::coo_matrix<int, double, cusp::host_memory> M(mxGetM(prhs[3]),
                                                         mxGetN(prhs[3]),
                                                         nnz_M);
    double *rowM = (double*)mxGetData(matlab_coo_M[0]);
    double *colM = (double*)mxGetData(matlab_coo_M[1]);
    for (int i = 0; i < nnz_M; i++)
    {
        M.row_indices[i] = rowM[i] - 1;
        M.column_indices[i] = colM[i] - 1;
    }
    memcpy(&M.values[0],         mxGetData(matlab_coo_M[2]), sizeof(double) * nnz_M);

    /* Copy to GPU */
    cusp::coo_matrix<int, double, cusp::device_memory> gpuM = M;
    /* A = gpuA; */

#if DEBUG
    cusp::io::write_matrix_market_file(M, "M.mtx");
#endif

    /* Allocate space for solution */
    cusp::array1d<double, cusp::host_memory> x1(A_num_rows, 0);
    cusp::array1d<double, cusp::device_memory> gpux1 = x1;

    cusp::verbose_monitor<double> monitor(gpuB, 8000, 1e-5);

    //cutStartTimer(kernelTime);
    /* solve the linear systems */
 QueryPerformanceFrequency(&frequency);
    QueryPerformanceCounter(&start);
 cusp::krylov::bicgstab(gpuA, gpux, gpuB, monitor);
    //cusp::krylov::cg(gpuA, gpux, gpuB, monitor);
    //cusp::krylov::gmres(gpuA, gpux, gpuB, 20, monitor);

 cudaDeviceSynchronize();
    QueryPerformanceCounter(&end);

// if any error, such as launch timeout, return maximum run time,
    seconds = (cudaGetLastError() == cudaSuccess) ? ((double)(end.QuadPart -
start.QuadPart) / (double)frequency.QuadPart) : DBL_MAX;
    std::cout << seconds << std::endl;
    /*cudaThreadSynchronize();
    cutStopTimer(kernelTime);
    printf("Time for the kernel: %f ms\n", cutGetTimerValue(kernelTime));*/
    /* Copy result back */
    x1 = gpux;

    /* Store in output array */
    double *output = (double*)mxCalloc(A_num_rows, sizeof(double));
    memcpy(output, &x1[0], A_num_rows * sizeof(double));

#if DEBUG
    cusp::io::write_matrix_market_file(x1, "xsolve.mtx");
#endif

    plhs[0] = mxCreateNumericArray(1, &A_num_rows, mxDOUBLE_CLASS, mxREAL);
    mxSetData(plhs[0], output);
}
```

APPENDIX C

MATLAB SOURCE CODE FOR GCSPARSE CLASS DEFINITION

```
classdef gcsparse < handle
    % sparse array GPU class
    % Usage:
    % A=gcsparse(A,[format]);
    % A=gcsparse(col,row,val,[nrows,[ncols,[format]]]);
    % format: 0 for COO, 1 for CSR (0 is default);
    % A: can be  matlab full/sparse array or gcsparse itself
    %
    % overloaded operators:
    % transpose: B=A.';
    % transpose: B=A';
    % multiply: x=A*y; (spmv)
    % size: [row, columns]
    % type: class/real/complex
    %
    % format conversion:
    %         B=real(A);
    %         A=complex(B);
    %         B=gcsparse(A,format);
    %         rowptr= ptr2row(A);
    %         row   =grow2ptr(A);
    % row <-> offset pointer conversion may crash inside the function,
    % but manually does not:
    %       so, to convert from A COO, to B CSR one can use this instead:
    %         B=A; %copy
    %         B.row= gptr2row(A.row,int32(A.nrows+1),A.nnz);
    %         B.format=1;
    %
    % S. Marchesini, LBNL 2013


    %    properties (SetAccess='private')
    properties
        nrows=int32(0); % number of rows
        ncols=int32(0); % number of columns
        nnz=int32(0);   % non zero elements
        val=gpuArray([]); %values  (gpu real/complex, single)
        col=gpuArray(int32([])); % column index (gpu int32)
        row=gpuArray(int32([])); % row/ptr index (gpu int32)
        format=int32(0); %0 for COO 1 for CSR
    end
    methods (Access = private)
    end
    methods (Static)
    end
    methods
        function obj = gcsparse(col,row,val,nrows,ncols,format)

            if nargin<6         %default is COO
```

```
                format=int32(0); %COO
            else
                format=int32(format);
            end

            if (nargin<=2); %gcsparse(A,[format])
                % get the sparse structure of A
                if nargin==2    %gcsparse(A,format) (format=row, second
input)
                    format=int32(row); %row is actually the second input
                else
                    format=0;
                end

                if isa(col,'gcsparse') % we are just converting here
                      obj=col; %col is actually the fisrt input
                    if obj.format==format %nothing to do...
                        return
                    elseif (obj.format==0 && format==1)
                         obj.row=row2ptr(obj); %COO->CSR
                        obj.format=format;
                    elseif (obj.format==1 && format==0);
                         %nptr=obj.nrows+1;
                         %rowptr= gptr2row(obj.row,nptr,obj.nnz);
                                                rowptr=ptr2row(col);  %CSR->
COO
                         %
obj.row=gptr2row(obj.row,nptr,obj.nnz);
                         obj.row=rowptr;
                         obj.format=format;
                    else
                        fprintf('invalid');
                    end
                    return
                else
                    % get  val,col,row triplets from A (first input)
                    [obj.nrows,obj.ncols]=size(col); %col is actually the
fisrt input
                    obj.nrows=gather(obj.nrows);
                    obj.ncols=gather(obj.ncols);

                    [obj.row,obj.col,obj.val]=find(col);

                    obj.col=gpuArray(int32(obj.col(:)));
                    obj.row=gpuArray(int32(obj.row(:)));
                    obj.val=gpuArray((single(obj.val(:))));
                end
                if nargin==2
                    format=int32(row); %row is actually the second input
                end
            else
                obj.col=gpuArray(int32(col(:)));
                obj.row=gpuArray(int32(row(:)));
                obj.val=gpuArray(val(:));
                obj.nrows=gather(int32(max(obj.row(:))));
                obj.ncols=gather(int32(max(obj.col(:))));
                obj.nnz=int32(obj.nnz);
            end

            obj.nnz=gather(int32(numel(obj.val)));

            % matlab to c indexing...:
            obj.col=obj.col-1;
            obj.row=obj.row-1;
            % increase nrows if input [nrows] is given
            if nargin>3
                if(~isempty(nrows))
                    obj.nrows=gather(int32(max(obj.nrows,nrows)));
                end
                if nargin>4
                    if (~isempty(ncols))
                        obj.ncols=int32(max(obj.ncols,ncols));
                    end
                end
            end
            % sort by rows
            [obj.row,unsort2sort]=sort(obj.row);
            obj.col=obj.col(unsort2sort);
            obj.val=obj.val(unsort2sort);
            obj.format=0;

            if  format==1;
                %                 obj.row=coo2csr(obj);
                obj.row= row2ptr(obj);
                obj.format=1;
            end
            %                'hi'
        end
        function B=real(A)
            B=A;
            B.val=real(B.val);
        end
        function B=complex(A)
            B=A;
            if isreal(A.val);
                B.val=complex(B.val);
            end
        end
        function y = mtimes(A,x) %SpMV
            %SpMV with CUSP
            if A.format==0
                % y=0;
                wait(gpuDevice())
                y=gspmv_coo(A.val,A.col,A.row,A.nrows, x);
            elseif A.format==1
                %  y=gspmv_csr(A.col,A.row,A.val,A.nrows,A.ncols,x);
                wait(gpuDevice());
                y=gspmv_csr(A.val,A.col,A.row,x);
            end
        end
        function C= ctranspose(obj)
```

```
            % format->coo->transpose->format
            C=gcsparse(obj,0); %convert to COO
            tmprow=C.col; %swap row and columns
            C.col=C.row;
            C.row=tmprow;
            tmp=C.nrows;
            C.nrows=obj.ncols;
            C.ncols=tmp;
            C.val=conj(obj.val); %conjugate
            C=gcsparse(C,obj.format); %revert to original format
        end

        function C= transpose(obj)
            C=gcsparse(obj,0); %convert to COO
            tmprow=C.col;  %swap row and columns
            C.col=C.row;
            C.row=tmprow;
            tmp=C.nrows;
            C.nrows=obj.ncols;
            C.ncols=tmp;
            C=gcsparse(C,obj.format);
        end
        function [row,col,val]= find(obj)
           if obj.format==1;
                fprintf('it may not work, use COO\n')
                fprintf('[col,row,val]=find(gcsparse(A,0))');
%                 [~,row,~]=find(gcsparse(A,0));
                nptr=int32(obj.nrows+1);
                ptr=obj.row+0;
                nnz=obj.nnz+0;
                row=gptr2row(ptr,nptr,nnz);
%                row=ptr2row(obj);
                row=row+1;
                if numel(row)<obj.nnz
                    fprintf('did not work, use COO\n')
                end
%                 row=gptr2row(obj.row,int32(obj.nrows+1),obj.nnz);
           else
                row=obj.row+1;
           end
           col=obj.col+1;
           val=obj.val;

        end


        function m = size(obj)
            m=[obj.nrows obj.ncols];
        end
        function m = type(obj)
            f0= classUnderlying(obj.val);
            if (isreal(obj.val))
                fmt='Real';
            else fmt='Complex';
            end
            m=[f0 ' ' fmt];
        end
        function row= ptr2row(obj)
            %  offset pointer to row conversion
            row= gptr2row(obj.row,int32(obj.nrows+1),obj.nnz);
        end
        function rowptr= row2ptr(obj)
            %  row to offsets
            rowptr=grow2ptr(obj.row,(obj.nrows+1),(obj.nnz));
        end

    end

end
```

APPENDIX D
BUILT-IN MATLAB FUNCTIONS THAT SUPPORT GPUARRAY FOR MATLAB 2012A

Table D.1 shows the built-in functions that support gpuArray type that are available in the parallel computing toolbox for MATLAB version 2012a.

Table D.1 Available Built-In Functions for MATLAB 2012a Parallel Computing Toolbox that Support GPUArray

abs	conv2	floor	log
acos	cos	fprintf	log10
acosh	cosh	full	log1p
acot	cot	gamma	log2
acoth	coth	gammaln	logical
acsc	csc	gather	lt
acsch	csch	ge	lu
all	ctranspose	gt	mat2str
any	cumprod	horzcat	max
arrayfun	cumsum	hypot	meshgrid
asec	det	ifft	min
asech	diag	ifft2	minus
asin	diff	ifftn	mldivide
asinh	disp	imag	mod
atan	display	ind2sub	mrdivide
atan2	dot	int16	mtimes
atanh	double	int2str	ndgrid
beta	eig	int32	ndims
betaln	eps	int64	ne
bitand	eq	int8	norm
bitcmp	erf	inv	not
bitor	erfc	ipermute	num2str
bitshift	erfcinv	isempty	numel
bitxor	erfcx	isequal	permute
bsxfun	erfinv	isequaln	plot (and related)
cast	exp	isfinite	plus
cat	expm1	isinf	power
ceil	filter	islogical	prod
chol	filter2	isnan	qr
circshift	find	isreal	rdivide
classUnderlying	fft	issorted	real
colon	fft2	ldivide	reallog
complex	fftn	le	realpow
conj	fix	length	realsqrt
conv			

APPENDIX E
BUILT-IN MATLAB FUNCTIONS THAT SUPPORT GPUARRAY FOR MATLAB 2014A

Table E.1 shows the built-in functions that support gpuArray type that are available in the parallel computing toolbox for MATLAB version 2014a.

Table E.1 Available Built-In Functions for MATLAB 2014a Parallel Computing Toolbox that Support GPUArray

abs	blkdiag	display	gammaln	isinf	mod	real	times
acos	bsxfun	dot	gather	isinteger	mpower	reallog	trace
acosh	cast	double	ge	islogical	mrdivide	realpow	transpose
acot	cat	eig	gt	ismatrix	mtimes	realsqrt	tril
acoth	ceil	eps	horzcat	ismember	NaN	rem	triu
acsc	chol	eq	hypot	isnan	ndgrid	repmat	TRUE
acsch	circshift	erf	ifft	isnumeric	ndims	reshape	uint16
all	classUnderlying	erfc	ifft2	isreal	ne	rot90	uint32
and	colon	erfcinv	ifftn	isrow	nnz	round	uint64
angle	complex	erfcx	ifftshift	issorted	norm	sec	uint8
any	cond	erfinv	imag	issparse	normest	sech	uminus
arrayfun	conj	exp	ind2sub	isvector	not	shiftdim	uplus
asec	conv	expm1	Inf	kron	num2str	sign	var
asech	conv2	eye	int16	ldivide	numel	sin	vertcat
asin	convn	FALSE	int2str	le	ones	single	xor
asinh	cos	fft	int32	length	or	sinh	zeros
atan	cosh	fft2	int64	log	pagefun	size	
atan2	cot	fftn	int8	log10	perms	sort	
atanh	coth	fftshift	interp1	log1p	permute	sprintf	
besselj	cov	filter	interp2	log2	plot (and related)	sqrt	
bessely	cross	filter2	interp3	logical	plus	squeeze	
beta	csc	find	interpn	lt	pow2	std	
betaln	csch	fix	inv	lu	power	sub2ind	
bitand	ctranspose	flip	ipermute	mat2str	prod	subsasgn	
bitcmp	cumprod	fliplr	iscolumn	max	qr	subsindex	
bitget	cumsum	flipud	isempty	mean	rand	subsref	
bitor	det	floor	isequal	meshgrid	randi	sum	
bitset	diag	fprintf	isequaln	min	randn	svd	
bitshift	diff	full	isfinite	minus	rank	tan	
bitxor	disp	gamma	isfloat	mldivide	rdivide	tanh	

REFERENCES

[1] F. J. Bartos, "Efficient motors can ease energy crunch," *Control Engineering,* pp. 63-70, May 2001.

[2] P. C. Krause and O. Wasynczuk, *Electromechanical Motion Devices,* McGraw-Hill, 1989.

[3] S. J. Salon, *Finite Element Analysis of Electrical Machines,* Norwell: Kluwer Academic Publishers, 1995.

[4] R. Telichevesky, K. Kundert and J. White, "Efficient steady-state analysis based on matrix-free Krylov-subspace methods," in *32nd ACM/IEEE Design Automation Conference,* pp. 480-484, 1995.

[5] W. Yao, "Accurate, efficient, and stable domain decomposition methods for analysis of electromechanical problems," Ph.D. dissertation, University of Illinois at Urbana-Champaign, Urbana, IL, 2013.

[6] J. Jin, *The Finite Element Method in Electromagnetics*, New York: John Wiley & Sons, 2002.

[7] P. P. Silvester and R. L. Ferrari, *Finite Elements for Electrical Engineers*, Melbourne: Press Syndicate of the University of Cambridge, 1996.

[8] J. Crank and P. Nicolson, "A practical method for numerical evaluation of solutions of partial differential equations of the heat-conduction type," *Proc. Camb. Phil. Soc.*, vol. 43, no. 1, pp. 50-67, 1947.

[9] W. F. Tinney, V. Brandwajn and S. M. Chan, "Sparse vector methods," *Power Apparatus and Systems, IEEE Transactions on,* vols. PAS-104, no. 2, pp. 295-301, 1985.

[10] S. M. Chan and V. Brandwajn, "Partial matrix refactorization," *IEEE Transactions on Power Systems,* vol. 1, no. 1, pp. 193-199, 1986.

[11] Y. Saad, *Iterative Methods for Sparse Linear Systems,* Cambridge University Press, 2003.

[12] W. E. Arnoldi, "The principle of minimized iterations in the solution of the matrix," *Quarterly of Applied Mathematics,* vol. 9, pp. 17-29, 1951.

[13] C. Lanczos, "An iteration method for the solution of the eigenvalue problem of linear differential and integral operators," *Res. Nat'l Bur. Std,* vol. 45, no. 4, pp. 255-282, 1950.

[14] R. Barrett et al., *Templates for the Solution of Linear Systems: Building Blocks for Iterative Methods*, Philadelphia, PA: SIAM, 1994.

[15] Y. Saad and M. H. Schultz, "GMRES: A generalized minimal residual algorithm for solving nonsymmetric linear systems," *SIAM J. Sci. Stat. Comput,* vol. 7, no. 3, pp. 856-869, 1986.

[16] P. Sonneveld, "CGS: A fast Lanczos-type solver for nonsymmetric linear systems," *SIAM J. Sci. Stat. Comput.,* vol. 10, no. 1, pp. 36-52, 1989.

[17] H. A. van der Vorst, "BI-CGSTAB: A fast and smoothly converging variant of BI-CG for the solution of nonsymmetric linear systems," *SIAM J. Sci. Stat. Comput.,* vol. 13, no. 2, pp. 631-644, 1992.

[18] M. T. Heath, *Scientific Computing: An Introductory Survey*, New York, NY: McGraw-Hill, 2002.

[19] T. A. Manteuffel, "An incomplete factorization technique for positive definite linear systems," *Math. Comput*, vol. 34, no. 150, pp. 473-497, 1980.

[20] S. C. Brenner and L. R. Scott, *The Mathematical Theory of Finite Element Methods*, New York: Springer Science + Business Media, 2010.

[21] T. Nakata, N. Takahashi, K. Fujiwara, N. Okamoto and K. Muramatsu, "Improvements of convergence characteristics of Newton-Raphson method for nonlinear magnetic field analysis," in *IEEE Transactions on Magnetics*, vol. 28, no. 2, pp. 1048-1051, 1992.

[22] K. Fujiwara, T. Nakata, N. Okamoto and K. Muramatsu, "Method for determining relaxation factor for modified Newton-Raphson method," in *IEEE Transactions on Magnetics*, vol. 29, no. 2, pp. 1962-1965, 1993.

[23] A. Burtscher, E. Fonn and P. Meury, "Swiss federal institute of technology Zurich department of mathematics handouts and lecture notes," [Online]. Available: https://www.math.ethz.ch/education/bachelor/lectures/fs2013/other/n_dgl/serien/edit/LehrFEM.zip. [Accessed April 2011].

[24] Mathworks Technical Staff, *Parallel Computing Toolbox Documentation*, The Mathworks, Inc., 2014.

[25] Mathworks Technical Staff, *Parallel for-Loops (parfor) Documentation*, The Mathworks, Inc., 2014.

[26] J. Doke, "MATLAB central file exchange - demo files for parallel computing with MATLAB on multicore desktops and GPUs webinar," 11 May 2011. [Online]. Available: http://www.mathworks.com/matlabcentral/fileexchange/31336-demo-files-for--parallel-computing-with-matlab-on-multicore-desktops-and-gpus--webinar/content/. [Accessed June 2011].

[27] M. J. Quinn, *Parallel Programming in C with MPI and OpenMP*, New York: McGraw-Hill, 2003.

[28] S.-I. Sugimoto, H. Kanayama, M. Ogino and S. Yoshimura, "Introduction of a direct method at subdomains in non-linear magnetostatic analysis with HDDM," in *2010 International Conference on Broadband, Wireless Computing, Communication and Applications*, 2010, pp. 304-309.

[29] Y. Zhan and A. M. Knight, "Parallel time-stepped analysis of induction machines with Newton-Raphson iteration and domain decomposition," in *IEEE Transactions on Magnetics*, vol. 44, no. 6, pp. 1546-1549, 2008.

[30] Y. Takahashi et al., "Parallel time-periodic finite-element method for steady-state analysis of rotating machines," in *IEEE Transactions on Magnetics*, vol. 28, no. 2, pp. 1019-1022, 2012.

[31] C. Fu, "A parallel algorithm for nonlinear dynamic finite element analysis," *Information Science and Engineering (ICISE), 2009 1st International Conference on*, 2009, pp. 59-62.

[32] D. B. Kirk and W.-M. W. Hwu, *Programming Massively Parallel Processors: A Hands-on Approach*, Burlington: Morgan Kaufmann Publishers, 2010.

[33] NVIDIA Corporation, "NVIDIA CUDA toolkit documentation: CUDA C programming guide," March 2015. [Online]. Available: http://docs.nvidia.com/cuda/cuda-c-programming-guide/index.html. [Accessed March 2015].

[34] NVIDIA Corporation Technical Staff, "Technical brief: NVIDIA GeForce 8800 GPU architecture overview," NVIDIA Corporation, Santa Clara, CA, Tech. Rep. TB-02787-001_v01, 2006.

[35] M. Naumov, "Incomplete-LU and Cholesky preconditioned iterative methods using CUSPARSE and CUBLAS," NVIDIA Corporation, Santa Clara, CA, White Paper Tech. Rep., Jun. 2011.

[36] R. Li and Y. Saad, "GPU-Accelerated preconditioned iterative linear solvers," *The Journal of Supercomputing,* vol. 63, no. 2, pp. 443-466, 2013.

[37] A. Dziekonski, A. Lamecki and M. Mrozowski, "Jacobi and Gauss-Seidel preconditioned complex conjugate gradient method with GPU acceleration for finite element method," in *Proceedings of the 40th European Microwave Conference*, 2010, pp. 1305-1308.

[38] A. Dziekonski, A. Lamecki and M. Mrozowski, "Tuning a hybrid GPU-CPU V-cycle multilevel preconditioner for solving large real and complex systems of FEM equations," *Antennas and Wireless Propagation Letters, IEEE,* vol. 10, pp. 619-622, June 2011.

[39] N. Bell and M. Garland, "Efficient sparse matrix-vector multiplication on CUDA," NVIDIA Corporation, Santa Clara, CA, Tech. Rep. NVR-2008-004, 2008.

[40] A. Ashari, N. Sedaghati, J. Eisenlohr, S. Parthasarath and P. Sadayappan, "Fast sparse matrix-vector multiplication on GPUs for graph applications," in *High Performance Computing, Networking, Storage and Analysis, SC14: International Conference for,* 2014, pp. 781-792.

[41] Z. A. Taylor, M. Cheng and S. Ourselin, "High-speed nonlinear finite element analysis for surgical simulation using graphics processing units," *IEEE Transactions on Medical Imaging,* vol. 27, no. 5, pp. 650-663, 2008.

[42] R. Couturier and S. Domas, "Sparse systems solving on GPUs with GMRES," *The Journal of Supercomputing,* vol. 59, no. 3, pp. 1504-1516, 2012.

[43] NVIDIA Corporation, "Sparse linear algebra library based on thrust," [Online]. Available: http://cusplibrary.github.io/. [Accessed 2014].

[44] NVIDIA Corporation, "NVIDIA CUDA toolkit v7.0 documentation: cuSPARSE," 5 March 2015. [Online]. Available: http://docs.nvidia.com/cuda/cusparse/. [Accessed 2015].

[45] A. George and W. H. Liu, "The evolution of the minimum degree ordering algorithm," *SIAM,* vol. 31, no. 1, pp. 1-19, 1989.

[46] S. Marchesini, "MATLAB central file exchange: GPU sparse, accumarray, non-uniform grid," Lawrence Berkeley National Laboratory, December 2013. [Online]. Available: http://www.mathworks.com/matlabcentral/fileexchange/44423-gpu-sparse--accumarray--non-uniform-grid. [Accessed 2013].

[47] T. Nakata, N. Takahashi and K. Fujiwara, "Summary of results for benchmark problem 10 (steel plates around a coil)," in *COMPEL - The International Journal for Computation and Mathematics in Electrical and Electronics Engineering,* vol. 15, no. 2, pp. 103-112, 1995.

[48] J. Wells, P. Chapman and P. Krein, "Development and application of a linear induction machine for instructional laboratory use," in *Proc. IEEE Power Electronics Specialists Conference,* 2002, pp. 479-482.

[49] M. Magill, "A composite material approach towards induction machine design using planar layer models," M.S. thesis, University of Illinois at Urbana-Champaign, Urbana, IL, 2011.

[50] P. Pillay, "Improved design of motors for increased efficiency in residential and commerical buildings," U.S. Department of Energy, Washington, DC, Building Technologies Program Topical Report, 2008.

[51] M. Amrhein and P. T. Krein, "3-D magnetic equivalent circuit framework for modeling electromechanical devices," *Energy Conversion, IEEE Transactions on,* vol. 24, no. 2, pp. 397-405, 2009.

[52] A. J. Adzima, P. T. Krein and T. C. O'Connell, "Investigation of accelerating numerical-field analysis methods for electric machines with the incorporation of graphic-processor based parallel processing techniques," in *Electric Ship Technologies Symposium, 2009. ESTS 2009. IEEE*, 2009, pp. 59-64.